A Technique for Rapid Prediction of Aftbody Nozzle Performance for Hypersonic Launch Vehicle Design

A Thesis

Presented to

The Academic Faculty

by

John Edward Bradford

In Partial Fulfillment
of the Requirements for the Degree of
Doctor of Philosophy in Aerospace Engineering

Georgia Institute of Technology

June 2001

A Technique for Rapid Prediction of Aftbody Nozzle Performance for Hypersonic Launch Vehicle Design

Approved:

_____
John R. Olds, Chairman

_____
Dimitri N. Mavris, Thesis Commitee

_____
Stephen M. Ruffin, Thesis Commitee

_____
David R. Komar, Reading Commitee

_____
Amy Pritchett, Reading Commitee

Date Approved by Chairman _____

Music for the Masses…

ACKNOWLEDGEMENTS

First, I would like to express my sincere appreciation to everyone who has aided in my education and research over the years. Primarily, I would like to thank my advisor and mentor, Dr. John Olds, for giving me the opportunity to come to Georgia Tech. It has been one of the best decisions of my life. I would like to thank my GSRP sponsor, D.R. Komar at NASA Marshall, for all of his help and support over the years. The countless hours spent on the phone discussing performance analysis have been invaluable. I would also like to thank the members of my committee, Dr. Stephen Ruffin, Dr. Dimitri Mavris, and Dr. Amy Pritchett, for their advice and support. All of your suggestions have helped to make this work a success.

I would like to thank my parents, John and Sandra. You taught me the value of hard work and that has led to my current success in life. Thank you Dad for all the wisdom and advice over the years. I know you have more to give and I am sure I will need it. My gratitude must also be extended to my in-laws, Wendell, Peggy, Karl, June, Karla, and Jose. Their constant encouragement and support was always appreciated.

I would also like to thank the members of the Space Systems Design Lab. Namely all of the other 'founding members', Irene Budianto, Laura Ledsinger, David McCormick, and David Way. Thanks for all of the stimulating conversations (aerospace related and other) that always made coming into the office enjoyable.

Finally, I would like to thank my loving wife, Heather. Thank you for your patience and understanding for all those endless nights in the lab. I know it has been a rough road, but it made it all the better to share it with you.

TABLE OF CONTENTS

LIST OF TABLES

LIST OF FIGURES

NOMENCLATURE

ABBREVIATIONS

A_c	normalizing area for thrust coefficient
A_i	engine cross-sectional area at station *i*
Ar	argon
BTU	british thermal units, 778.17 lbf-ft
$C_{f,forebody}$	forebody skin friction coefficient
$C_{f,combustor}$	combustor skin friction coefficient
Cf	rocket engine thrust coefficient
C_p	constant pressure specific heat, BTU/lbm-R
C_t	thrust coefficient
C-D	converging-diverging
$F_{z,x}$	axial body force due to *z*, lbs
$F_{z,y}$	normal body force due to *z*, lbs
H_2O_2	hydrogen peroxide
H	monatomic hydrogen
H_2	hydrogen
H_t	total enthalpy per unit mass, BTU/lbm
I_{sp}	specific impulse, s
L	aftbody nozzle length, ft
MixR	propellant mixture ratio, (oxidizer weight/fuel weight)
$\mathcal{MW}_i$	mixture molecular weight at station *i*
N_2	diatomic nitrogen
$N_{species}$	number of unique molecules
N-R	Newton-Rhapson root finder
N	monatomic nitrogen
NO	nitrogen oxide

O	monatomic oxygen
OO	object-oriented
O_2	oxygen
OH	hydroxyl radical
P_c	rocket chamber pressure, psi
P_t	total pressure, psi
P-B	Plackett-Burman
P-C	Predictor-Corrector integration routine
PdAx	non-dimensional integrated nozzle normal force
PdAy	non-dimensional integrated nozzle axial force
R	rankine
R^2	residual
$R_{universal}$	universal gas constant, 49712.52 BTU/lbm-R
R-K	Runge-Kutta integration routine
T/W	vehicle thrust-to-weight ratio
T/W_e	engine thrust-to-weight ratio
V_{fuel}	fuel injection velocity, ft/s
V_r	cone flow radial velocity component, ft/s
V_θ	cone flow normal velocity component, ft/s
deg	degree
ft	feet
fps	feet per second
g	gravitational acceleration, 32.174 ft/s^2
h_{cowl}	height of engine at cowl leading edge, ft
h_s	static enthalpy per unit mass, BTU/lbm
k	number of variables in response surface equation
lbm	pounds mass
lbs	pounds force
log	logarithm
$\dot{m}_i$	mass flow rate at station i, lbm/s
$\dot{m}_{rocket}$	mass flow rate of rocket thruster system, lbm/s
n	number of experiments
nmi	nautical mile

phi	combustor equivalence ratio, stoichiometric-to-actual fuel-to-air ratio
psf	pounds per square foot
psi	pounds per square inch
q	freestream dynamic pressure, psf
s	seconds
w_{nozzle}	width of aftbody nozzle, ft
1-D	one dimensional
2-D	two dimensional
3-D	three dimensional

ACRONYMS

A/B	Airbeathing
ABLV	Airbreathing Launch Vehicle
AFRSI	Advanced Flexible Reusable Surface Insulation
AIAA	American Institute of Aeronautics and Astronautics
APAS	Aerodynamic Preliminary Analysis Software
CA	Contributing Analysis
CAD	Computer Aided Design
CCD	Central Composite Design
CFD	Computational Fluid Dynamics
CGI	Common Gateway Interface
CIM	Common Industry Method
CPG	Calorically Perfect Gas
CPU	Central Processing Unit
DOF	Degrees Of Freedom
DOE	Design of Experiments
ERJ	Ejector Ramjet
ESJ	Ejector Scramjet
GH2	Gaseous Hydrogen
GOX	Gaseous Oxygen
GUI	Graphical User Interface

HTML	HyperText Markup Language
JANNAF	Joint Army Navy NASA Air-Force
KSC	Kennedy Space Center
LaRC	Langley Research Center
LH2	Liquid Hydrogen
LOX	Liquid Oxygen
MDO	Multidisciplinary Design Optimization
MECO	Main Engine Cut-Off
MER	Mass Estimating Relationship
MOC	Method Of Characteristics
NASA	National Aeronautics and Space Administration
NASP	National Aerospace Plane
OMS	Orbital Maneuvering System
PERL	Practical Extraction and Report Language
POST	Program to Optimize Simulated Trajectories
RBCC	Rocket Based Combined-Cycle
RCS	Reaction Control System
RJ	Ramjet
RLV	Reusable Launch Vehicle
RSE	Response Surface Equation
RSM	Response Surface Methodology
RTLS	Return to Launch Site
SCCREAM	Simulated Combined-Cycle Rocket Engine Analysis Module
SERJ	Supercharged Ejector Ramjet
SJ	Scramjet
SLS	sea-level static
SSTO	Single-Stage-to-Orbit
TPG	Thermally Perfect Gas
TPS	Thermal Protection System
UHTC	Ultra-High Temperature Ceramic
W&S	Weights and Sizing

SYMBOLS

f	fuel-to-air ratio
γ	ratio of specific heats
θ_i	expansion or compression surface angle, deg
ϕ	equivalence ratio, phi
β	shock wave angle, deg
ψ	fuel injection angle, deg

SUBSCRIPTS

1	location of cowl leading edge
2	location of diffuser exit
3	location of mixer or isolator exit
4	location of combustor exit
5	location of converging-diverging nozzle throat
e	location of cowl trailing edge
e'	location of aftbody nozzle tip
i	engine station identifier
N	normal component
t	total property
s	static property
δ	turn angle of flow through shockwave, deg
α	vehicle angle of attack, deg
θ	angle of ray from conical forebody centerline

SUMMARY

Air breathing propulsion engines for space applications are very complex systems and must be specifically tailored to a particular vehicle concept. These types of engines are in many instances 'airframe integrated', meaning the engine flowpath is partially defined by the vehicle mold lines. This implies that when designing an engine concept, the vehicle mold lines are directly coupled with the engine performance. Any optimization of the propulsion system must then include the entire vehicle system.

Due to available computing resources, it is impractical to attempt to optimize the complete engine flowpath. It is possible to optimize the forebody section by ignoring the aftbody section. Accurate estimates of forebody pressures can be obtained through closed-form equations for the flowfield and shock waves. This allows for selection of optimal compression ramp angles. But, closed form equations that accurately model the flow do not exist for the aftbody region of the vehicle. Studies have shown that the aftbody geometry has a significant effect on the overall propulsion system performance, with nozzle thrust variations of up to 30% depending on the nozzle expansion angles and flow model assumed. Therefore, ignoring the aftbody section cannot produce a truly optimized design.

While the aftbody flowfield can be analyzed with computer-intensive computational fluid dynamic codes, this approach is not suitable for use in conceptual vehicle studies. In order

to accomplish any complete vehicle optimization at the conceptual design level, changes in performance due to the nozzle design must be available quickly. To make this task even more challenging, performance changes need to be assessed over a broad range of flight conditions, instead of just at a single point.

A new approach has been developed to enable accurate performance prediction and the optimization of the aftbody geometry. This approach involves generating response surface equations of the aftbody pressure distributions. The response surface equations are generated from the results of a new two-dimensional, inviscid flow solver. Parameters that affect the pressure distribution and serve as input variables to the response surface equations include the nozzle geometry, combustor-exit flow conditions, and the freestream flow properties. The results of this new approach have been incorporated into SCCREAM, a conceptual-level engine performance prediction tool.

As a demonstration of the usefulness and effectiveness of this technique, a sample design case was considered that involved an advanced, hypersonic launch vehicle concept. The vehicle performance, in terms of gross and dry weight, was assessed and compared for the three cases of a nozzle analysis using current industry practice, incorporating the new aftbody nozzle thrust predictions, and finally with the new aftbody thrust and lift predictions. Results show a decrease in vehicle gross weight of 35% when incorporating the thrust and lift predictions from the higher level nozzle analysis, indicating the vehicle sensitivity to this component. The vehicle dry weight was also shown to decrease by 33% for this case.

CHAPTER I

INTRODUCTION

1.1 Motivation

Engineers in the conceptual launch vehicle design environment need to be able to assess engine performance at every point in a vehicle's trajectory. Unlike rocket engines, where the propulsion system is dependent only on the vehicle altitude, air-breathing propulsion system performance is strongly dependent on the vehicle's attitude (angle of attack) and flight path (velocity, dynamic pressure).

At the conceptual design level, exploring the design space for transportation systems typically emphasize breadth over depth, in terms of analysis fidelity and configuration options considered. Analysts need to quickly identify promising vehicle configurations, determine feasibility, and assess the economic viability of the system. While achieving a feasible configuration can be extremely difficult, achieving economic viability for a configuration is even more challenging, if not impossible in many cases. Thus, optimization of the configuration is a critical part of the design process. Depending on the number of

variables being considered, the optimization of a vehicle configuration can require tens to hundreds of closed vehicle designs, or 'point designs'. Obtaining a single point design can require 10-15 system level iterations, requiring multiple analyses from many disciplines. Based on the total number of disciplinary evaluations required, conceptual design tools need execution times on the order of minutes, not hours or days. Analysis tools that require model setup and execution times of days or hours (i.e. CFD, FEA with currently available computing resources) are considered 'slow' and although they typically offer higher fidelity, are not suitable for conceptual design. With future advances in computing resources, it will become possible to utilize higher fidelity tools at this stage in the design process. Tools suitable for use in the conceptual design phase must have setup and execution times on the order of minutes.

When designing a launch vehicle, strong coupling exists between various vehicle disciplines: configuration, aerodynamics, propulsion, trajectory, aerodynamic heating, mass properties, operations, and cost. Figure 1.1 shows the coupling for these eight disciplines in the Design Structure Matrix (DSM) [1]. A DSM enables quick visualization of system component interactions and couplings. Each discipline is represented by a block, known as a Contributing Analysis (CA). Surrounding each CA block are connecting paths to other disciplines. To the left and right sides of each box are connecting paths with data originating from the CA and flowing to other CA's (i.e. output parameters). Above and below each CA box are input parameters being provided to the CA from other disciplines.

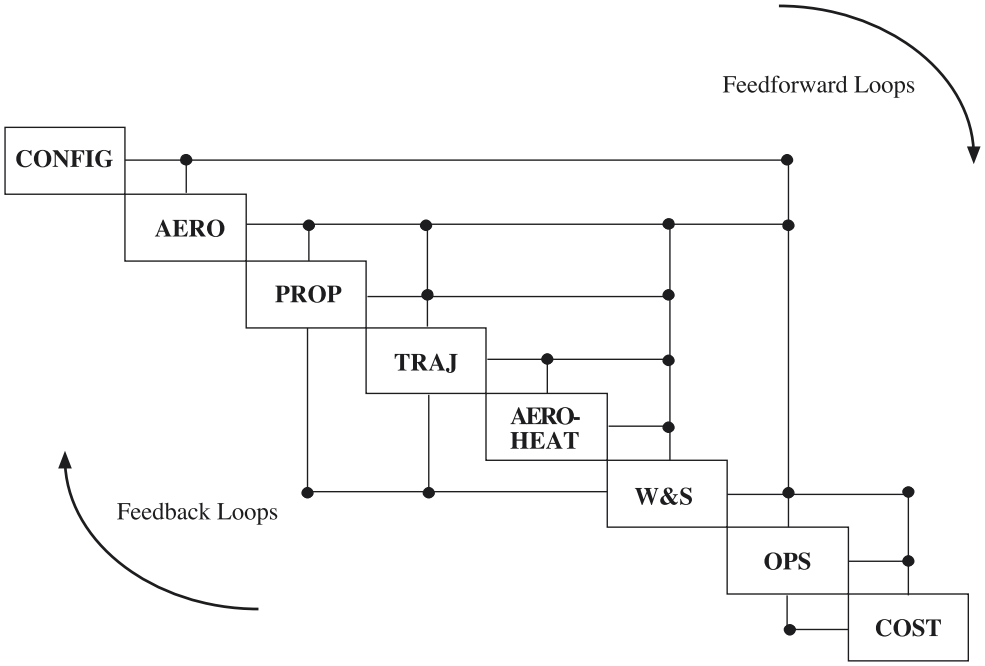

Figure 1.1 Typical Design Structure Matrix for Hypersonic Launch Vehicles

Disciplinary variable coupling can be resolved and a solution obtained through a variety of techniques involving numerous iterations by each discipline. A vehicle that has resolved internal data inconsistencies between disciplines is referred to as a 'closed' design. Thus, for the propulsion system, in addition to the requirement that the performance be assessed at every flight condition along the trajectory, a reassessment over the entire trajectory, for a range of vehicle sizes, is required numerous times to resolve the coupling issues between disciplines. This necessitates the need for design-oriented analysis tools that execute quickly and minimize the level of user interaction required.

For propulsion system design, in addition to a need for a design-oriented analysis tool, the overall performance estimation must also be improved. The engine component that has the

most significant impact on vehicle performance is the 'aftbody' or nozzle. Unfortunately, this component typically receives the lowest level of modeling detail in conceptual design studies. One option to correct this problem is to simply incorporate a higher fidelity analysis. But, higher fidelity techniques come at the expense of execution time. Therefore, simply incorporating this type of analysis is not a viable answer as the entire design process, as shown in the DSM, would suffer. Improvements made in modeling accuracy cannot be made at the expense of speed.

Aftbody nozzle flowfields have been studied fairly extensively in both computational and experimental analysis [2,3,4]. As a result of this work, the nozzle problem on its own is understood well, but this understanding has yet to be incorporated quantitatively into the conceptual design process. There is not a detailed understanding of how the nozzle's design and performance impacts the entire vehicle system.

Common industry practice for assessing nozzle performance is to expand either the frozen or equilibrium flow from the combustor exit to an assumed, projected nozzle exit area. An efficiency factor is then applied to the nozzle thrust. This technique, referred to as the 'Common Industry Method' (CIM), is a drastic oversimplification of the problem and the associated complex flowfield generated by the interaction between combustion exhaust products, high velocity air stream, and nozzle surface. The benefit of this approach lies in its simplicity and speed of execution, with nearly instantaneous generation of results. With the nozzle's primary function being to expand the engine exhaust products onto the aftbody of the vehicle and generate thrust, it is easy to see that assumptions made about the nozzle characteristics can have a dramatic impact on the vehicle system. Not only does the nozzle affect the overall engine thrust, it also generates a normal force on the vehicle which is an additional source of lift. Additionally, the pressure distribution along the nozzle surface

greatly affects the pitching moment of the vehicle. These moments influence the static and dynamic stability of the entire vehicle. In fact, some studies have suggested that when moments are integrated into the vehicle analysis, the system changes from being feasible to infeasible, with the vehicle gross weight increasing by as much as a factor of two [5,6].

Table 1.1 Relative Error in CIM vs. CFD Nozzle Thrust

	20° Ramp	25° Ramp	30° Ramp
$Mach_\infty$ 6	+28.3%	+0.7%	-15.4%
$Mach_\infty$ 10	+1.1%	-18.56%	-31.64%

A preliminary study was performed to compare the nozzle thrust using the CIM with a more accurate two-dimensional (2-D) numerical fluid analysis model. Table 1.1 shows the relative error between the axial forces for results using the CIM (current conceptual technique) with the higher fidelity results for a generic scramjet engine at two different freestream Mach number flight conditions. The nozzle was a single expansion ramp design (SERN) analyzed for three different cases with ramp angles of 20, 25, and 30 degrees. For the CIM cases, a divergence loss equal to the cosine of the ramp angle is included. It should be noted that the performance is highly dependent on the ramp angle assumed, with lower ramp angles yielding lower axial forces but higher normal forces. Figure 1.2 also shows the pressure distribution from CFD results for a 10° SERN design at a freestream Mach number of ten. Note the large discrepancy in the tail end of the distribution, leading to the CIM case overpredicting the axial and normal forces by 24%.

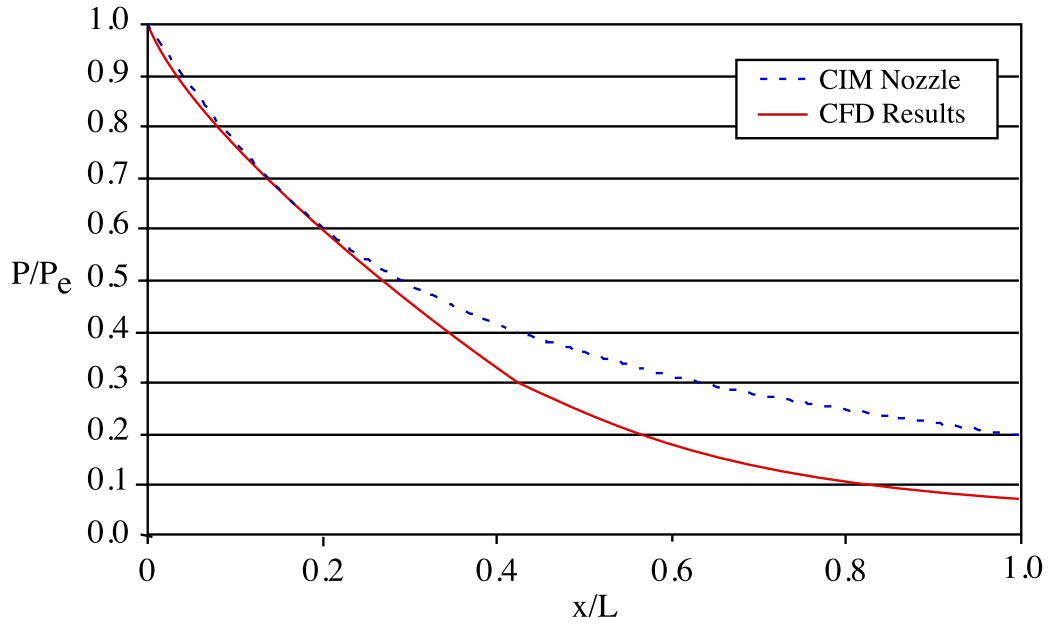

Figure 1.2 10° SERN Pressure Distribution Comparison

With performance prediction variations of up to 30%, the results from this table and figure clearly demonstrate the nozzle geometry significance and the need for improvements in the nozzle performance predictions.

1.2 Objective

The overall thesis objective is the establishment and verification of a new propulsion system design strategy, suitable for use in conceptual launch vehicle design. This process should allow the rapid, accurate assessment of airbreathing (A/B) and Rocket-Based Combined-Cycle (RBCC) propulsion system performance over a wide range of flight conditions and altitudes.

Numerous new capabilities to the conceptual launch vehicle designer will be enabled. These capabilities include accounting for propulsive lift, optimizing the vehicle aftbody nozzle shape and the entire engine flowpath, as well vehicle pitch-plane moment trajectory simulations. These capabilities will be enabled through a significant improvement in the aftbody nozzle analysis method and results currently used, thus providing the propulsion engineer with technical data previously not available at this early stage in the design process.

1.3 Goals

The goals of this thesis can be divided into two categories, qualitative and quantitative:

- On a qualitative level, the goal is to enable improved determination of nozzle performance in conceptual design studies. With these improved estimates, accurate studies of nozzle contours and geometry will be enabled, offering a host of new parameters for optimization at both the propulsion system and vehicle level.

- On a quantitative level, the goal will be to significantly reduce the error relative to the CIM in the nozzle axial and normal force predictions for all supersonic and hypersonic flight conditions. Predictions from the regressed CFD data with a relative error within +/-10% will be desirable and represent a significant improvement over the CIM analysis.

The final goal will be the implementation of the RSE's into SCCREAM, a design tool for advanced propulsion system analysis [7]. SCCREAM will be capable of taking full advantage of the powerful RSE's and the information they can provide. This will provide the

user with the capability and option of optimizing the aftbody geometry and vehicle pitch-plane moment analysis.

1.4 Approach

The rapid prediction method involves performing a Response Surface Methodology (RSM) [8]. The RSM will yield a series of Response Surface Equations (RSE's) that will predict the nozzle performance. RSE's are able to model complex systems as simple, multi-variable polynomial equations. These equations, shown in their general form as Equation 1.1, often yield very accurate results and save valuable computation time.

$$RSE = b_o + \sum_{i=1}^{n} b_i x_i + \sum_{i=1}^{n} b_{ii} x_i^2 + \sum_{\substack{i,j=1 \\ i \neq j}}^{n} b_{ij} x_i x_j \qquad (1.1)$$

The procedure involves first conducting a 'screening test' on potentially important design parameters that impact the nozzle performance. Results of this screening test are used to reduce the set of design parameters to a subset of the original that include only the variables with the most significant impact on the responses. The subset resulting from the screening test is used in generation of the RSE's for the pressure distribution on the nozzle section. The vehicle flight conditions, combustor exit conditions, and nozzle geometry are input variables to these RSE's.

The results of an analysis from a new 2-D Euler flow solver that is capable of modeling two jet streams will provide the desired nozzle pressure distribution information and experiment

results for the screening and RSE cases. The Euler code will be executed over a wide range of vehicle flight conditions, for various combustor exit conditions and nozzle designs. The primary output from each Euler solution will be the static pressures along the aftbody nozzle surface at five different axial locations. Each of these selected pressures will be the response for a particular experiment. These can be used to reconstruct the pressure distribution for a given case through a polynomial fitting algorithm and then integrated to obtain the net axial and normal forces on the nozzle. These forces and their location on the nozzle surface can then be used to compute the moment on the nozzle or vehicle. This procedure will establish a set of RSE's that will be applicable to many different engine designs, aftbody designs, and flight conditions. Figure 1.3 shows a flowchart representing this multi-step process. Note that Steps 1-4 are the most time consuming but only have to be performed only once for a given set of variable ranges. Steps 5 and 6 are then used repeatedly during future vehicle design processes and can be executed nearly instantaneously.

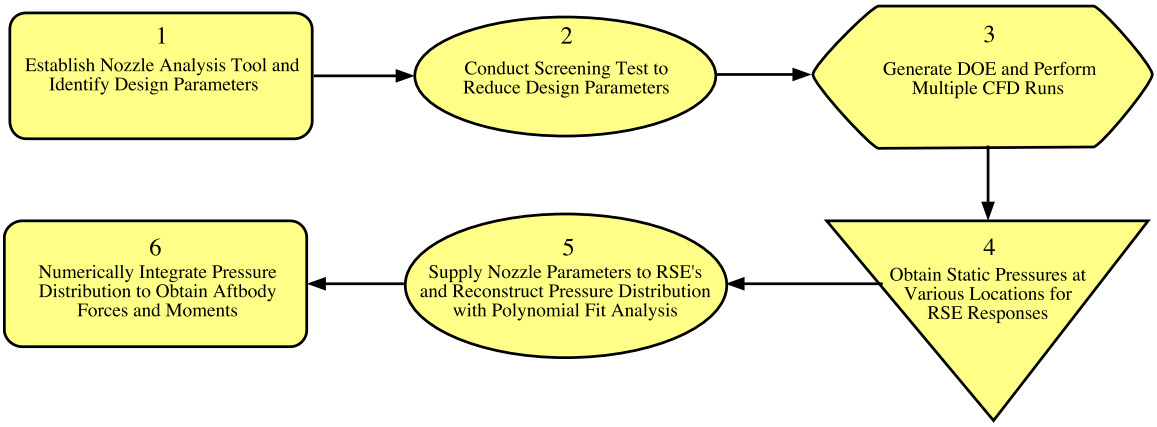

Figure 1.3 Rapid Aftbody Performance Prediction Process

A propulsion analysis tool suitable for analyzing A/B and RBCC propulsion systems will be created and referred to as SCCREAM. The aftbody RSE's will be incorporated into SCCREAM, allowing for more accurate force calculations, generation of propulsive moments, and optimization of the nozzle geometry. In addition to specifying other non-aftbody propulsion system variables, the geometry of the aftbody section (eg. expansion angles, area and height at the cowl trailing edge) will be required. SCCREAM will generate the flow properties (e.g. velocity, temperature, pressure) at the engine exit and provide the flight conditions (freestream velocity, pressure, density) as inputs to the RSE's. The pressure distribution generated by the RSE's and polynomial fit can then be integrated to obtain the forces on the vehicle aftbody. Depending upon the vehicle force accounting system selected, the nozzle forces can be combined with the forebody aerodynamic forces to obtain the net propulsive lift and thrust/drag on the vehicle. Finally, SCCREAM will create a formatted engine deck for use in the trajectory analysis. This engine deck will include overall engine performance metrics (thrust, fuel consumption) as well as the additional information gained from the nozzle analysis (normal force, moment coefficient).

1.5 Organization of the Thesis

First, a historical overview of A/B propulsion will be presented to familiarize the reader with current progress in the field. Then, the types of flow equations and assumptions used for engine performance predictions during the conceptual design phase will be presented. Next, the new aftbody analysis solver and prediction method will be explained in detail, along with the results from implementing this method. This effort will culminate into the development of SCCREAM, a tool for engine performance and aftbody nozzle analysis suitable for use in the conceptual design phase of launch vehicles. Finally, the results from a sample case

study performed for a representative advanced RLV utilizing RBCC propulsion will be shown.

CHAPTER II

OVERVIEW OF AIR-BREATHING PROPULSION

While many engine types are technically airbreathers, the ramjet and scramjet engines are typically assumed in the context of space access. Ramjet and scramjet propulsion systems are desirable over turbine-powered systems due to their mechanical simplicity and preferred over rockets because they utilize the oxidizer readily available in the atmosphere instead of from an onboard source (i.e. tanks). The difference between a ramjet and a scramjet engine lies mainly in their combustion process. While a ramjet operates with a subsonic airflow in its combustor, the scramjet engine combusts the flow supersonically. While the ramjet performance is superior, the scramjet engine provides wider operating ranges in terms of flight Mach number and altitude. They are both unique in that they offer high thrust, low weight, and low fuel consumption, a combination typically not encountered in propulsive devices.

2.1 Historical Perspective

In 1935, a Frenchman by the name of Rene LeDuc developed the idea for a manned, ramjet-powered aircraft and was awarded a patent for his design[9]. Due to delays caused by World War II, it would not be until 1949 before his concept could be tested in actual flight. Figure 2.1 shows a schematic of this subsonic ramjet aircraft during the historic day on which Mach 0.9 flight was obtained. Although operationally successful, the real potential of this propulsion system could not be realized in subsonic flight.

Around the same time as the LeDuc manned flight test, a team of engineers at the Navy's Applied Physics Laboratory in Maryland was conducting its own unmanned test of a supersonic-flight ramjet. This simple device was constructed using the exhaust pipe of a P-47 fighter. With small, solid rockets providing the initial boost phase, this projectile reached 2,050 ft/s in 1945, more than twice as fast as any manned aircraft at the time [10].

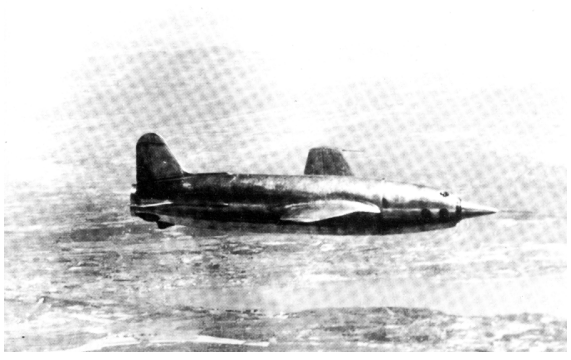

Figure 2.1 Rene LeDuc Subsonic Ramjet Flight

Ramjets have been used in missiles by the United States military for over 40 years now. Figure 2.2 shows two early uses of the ramjet engine. The 'Talos' was a sea-launched, Mach 3 surface-to-air missile used by the U.S. Navy between 1959 and 1979 [11]. This weapon had a range of fifty nautical miles due to its efficient ramjet propulsion system. The engines for this system were developed by the McDonell Aircraft Corporation, a large producer of ramjet engines at the time.

The 'D-21' was a top-secret unmanned reconnaissance vehicle that was launched off the top of the SR-71 Blackbird at supersonic speeds [12]. This drone, intended for aerial spy missions deep in enemy territory, was capable of Mach 3.5 flight and used a hydrocarbon fuel. The engines for this vehicle were developed by the Marquardt Corporation.

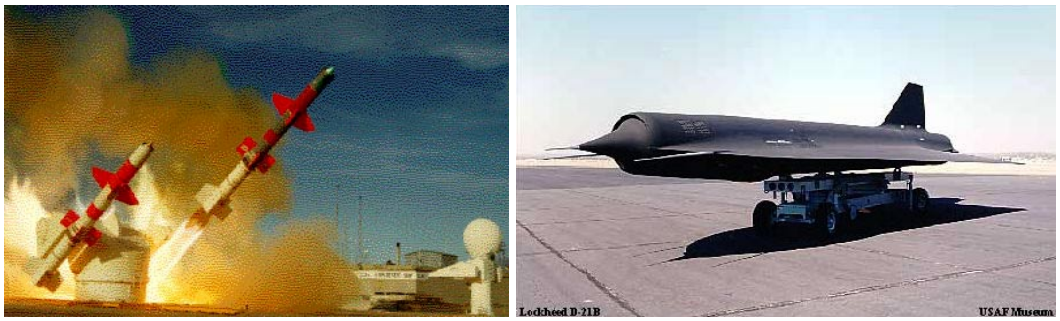

Figure 2.2 Talos Missiles and D-21 Drone

To date, there has yet to be an unclassified scramjet engine flight test. It remains uncertain whether a recent attempt made during a joint NASA-Russia test program actually achieved supersonic combustion, although the engine was a scramjet design[13]. Curran has

compiled an excellent review and detailed history of the scramjet engines development over the years [14].

The disadvantage of ramjet (RJ) and scramjet (SJ) engines is that they do not work outside of the atmosphere and they do not generate thrust during static and subsonic flight conditions (exception is the subsonic-ramjet design). These engines must be flying at supersonic speeds in order to achieve the ram-effect of compressing the incoming air stream and forcing it through the engine. This ram-effect replaces the need for heavy compressor turbomachinery. After this compression process, fuel is injected into either the subsonic or supersonic air stream. This fuel mixes and burns with the air inside the combustor. In the ramjet case, the flow is accelerated towards Mach one at the throat of a converging-diverging nozzle. The exhaust is then expanded supersonically, generating thrust. For scramjet engines, the supersonic combustor exit flow is simply exhausted into the nozzle and expanded.

One additional type of A/B propulsion system is the Rocket-Based Combined-Cycle (RBCC) engine. This engine concept, although slightly less known, has also been under investigation since the 1960's [15,16,17]. This propulsion system actually combines elements of rocketry and A/B propulsion, in an attempt to combine the best of both systems and obtain a single, integrated engine. This integration has led to these propulsive devices being referred to as 'Synerjet' engines for their synergistic operating characteristics [18]. Figure 2.3 shows an early, subscale RBCC engine from the Marquardt Corporation.

The RBCC engine is capable of generating static thrust and operating at subsonic, supersonic, hypersonic, and exo-atmospheric flight conditions. This is achieved by incorporating rocket thrusters into the A/B engine flowpath. At sea-level static (SLS)

conditions, the rockets are ignited, entraining air through the front of the engine. The rocket exhaust and entrained air mix together producing a subsonic flow. Additional thrust is generated by injecting fuel into this mixture further downstream in the engine. The net effect is generally a 10-20% increase in static engine performance over the thrust and Isp that would ordinarily be achieved by the rockets alone. The rockets are kept on until approximately Mach three when the ramjet can take over (i.e. inlet is started). At this point, the rockets are throttled down and the engine functions as a typical A/B system, with a RJ to SJ transition around Mach six. In the range of Mach 10-15, the rockets must be re-ignited due to the quickly diminishing thrust margin provided by the A/B engines. The optimal Mach number for this rocket re-ignition, called the transition Mach number (M_{tr}), is vehicle configuration and mission dependent. The rockets are then used to exit the sensible atmosphere and insert the vehicle into an elliptical transfer orbit (i.e. MECO point).

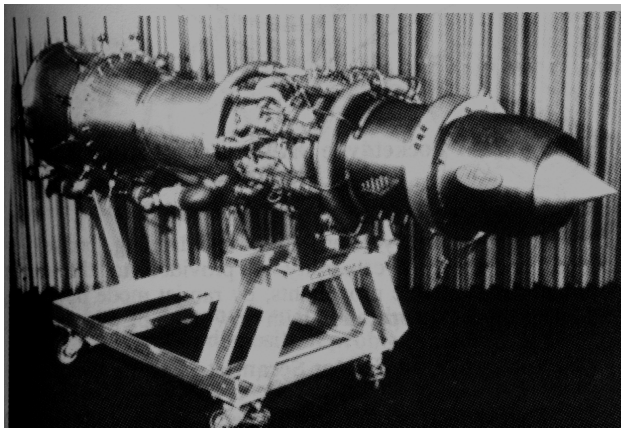

Figure 2.3 Early RBCC Engine Test Article, Marquardt Corporation

2.2 Current Status and Programs

Systems Studies

Recently, there has been a significant increase in the number and fidelity of advanced space transportation system architecture studies. This is partly attributable to significant gains in computing power over the past decade. A wide variety of airbreathing vehicle designs are currently being examined by a number of conceptual design organizations [19,20,21,22]. Some of the most common configuration options are: horizontal versus vertical takeoff, single-stage versus two-stage to orbit, magnetic launch assist, and combination versus combined-cycle propulsion options. With the continued increase in computing power, the fidelity of these vehicle systems will continue to increase, allowing for improved selection of optimal designs and reduction in program risk.

Hardware Testing

Two of the most significant and current activities involving A/B propulsion are the Hyper-X program and the Advanced Reusable Technologies (ART) program [23,24,25,26]. Both of these programs are being funded and managed by the National Aeronautics and Space Administration (NASA).

The Hyper-X program plans flight testing of three airframe-integrated scramjet engines, called the X-43a, in the Mach seven to ten flight regime. These flights are scheduled to occur over the Pacific Ocean beginning in June 2001. The vehicles, which measure eight feet in length and span five feet, will be air-dropped from a B-52 aircraft and boosted to hypersonic Mach numbers on the nose of Orbital Sciences Corporation's Pegasus-XL solid rocket motor. The vehicle will separate from the booster and obtain approximately ten

seconds of engine-on scramjet operation time. At the end of the flight, each vehicle will drop into the ocean and will not be recovered for economic reasons. If successful, the X-43a will set new flight Mach number records for A/B powered vehicles.

Figure 2.4 X-43a Scramjet Engine Flight Demonstrator

NASA's ART program has significantly advanced RBCC engine development and technology. From 1995 to 2000, the engine contractors of Pratt & Whitney, Aerojet, and Rocketdyne have built and tunnel tested three different sub-scale, copper heat-sink engine designs through all cycle modes and operating ranges representative of an RBCC-powered vehicle. These engines were all hydrogen-fueled and varied from utilizing completely fixed geometry (high T/W_e) to fully variable geometry, including the combustor (low T/W_e).

Additionally, NASA's Integrated Space Transportation Program (ISTP) office is funding 3rd Generation vehicle technology development[27]. A majority of these technologies are propulsion related, specifically for hypersonic A/B engine systems like RBCC.

Under ISTP funding, the construction of a flight-like RBCC engine, called *ISTAR*, has been awarded. This hydrocarbon-fueled engine will undergo ground testing at the NASA Stennis Space Center facility in Mississippi. The engine concept is based on GenCorp Aerojet's 'Strutjet' engine design [28]. Current design studies are examining ways to allow integration of this flight-like engine onto a vehicle airframe, currently being referred to as the 'X-43b'. The X-43b is envisioned as being air-dropped at subsonic flight conditions from a B-52 bomber. The vehicle will then accelerate under its own power to a Mach number of about seven. The vehicle length will be on the order of 35 feet.

2.3 Existing Analysis Tools

A survey of non-proprietary and commonly used engine design tools has been conducted. The four engineering tools identified are: HAP, RJPA, RAMSCRAM, and SRGULL. Each of the tools were categorized by their execution speed, accuracy, and useability. Useability is defined as whether the tool does the required task for the intended job for the intended user. Those tasks being airbreathing propulsion system analysis for use in conceptual vehicle design environment by either a user or automation script. Additionally, the engine modes each tool is capable of analyzing has also been identified in the table. The results of this classification are presented in Table 2.1. Although some of the categories are subjective, an accurate representation of these tools for real-world applications has been attempted.

Table 2.1 Summary of Available Engine Analysis Tools

+ fast/high O moderate - slow/low	Speed	Accuracy	Useability	AAR Mode	Ramjet Mode	Scramjet Mode	All-Rocket Mode
HAP	+	-	+		X	X	
RJPA	O	O	+			X	X
RAMSCRAM	O	O	O	X	X		
SRGULL	-	+	-		X	X	

As shown in Table 2.1, a variety of analysis tools exist and are in use for determining the performance of these types of A/B and RBCC engines. These tools offer a wide range of analysis fidelities and modeling options. Unfortunately, most are not well suited for use in the conceptual design environment Generally, tools with faster execution speeds have lower fidelity analysis levels. These lower fidelity tools tend to limit the types of system trade studies that can be performed by lacking the sensitivity to pick up higher order engine-vehicle interactions. Tools that do offer higher levels of fidelity are primarily intended for the generation of engine performance at a single flight condition and require inputs from other more detailed analysis or test data. This can require a significant amount of manual setup time in order to generate performance maps over the entire vehicle trajectory. A brief overview of each of these four tools will be presented next.

2.3.1 HAP

HAP is available with the AIAA Education Series books on A/B propulsion and is supported through the University of Washington [9]. The code is written in the BASIC programming language and can run on the Windows/DOS operating system. The performance analysis routine in this program assumes a calorically perfect gas (CPG), so its results are questionable for flows exceeding Mach three. The CPG assumption does allow the use of many closed-form equations, which contributes to HAP's speed and ease of use.

HAP is sufficient for 'back of the envelope' calculations, but is not suitable for use in any vehicle design and closure process. The tool lacks the ability to predict engine operating phenomena like inlet unstart and combustor choking. The force accounting system is a 'net-jet' approach, so off-line calculations are necessary to supplement the performance estimates and accurately measure the total propulsive force from the engine. Additionally, the code lacks a detailed equilibrium chemistry model and assumes ideal combustion which may overpredict engine performance in the higher flight Mach number regime. All HAP's input files are text based and no graphical user interface (GUI) is available.

2.3.2 RJPA

Developed by Johns Hopkins University in 1986, RJPA stands for RamJet Performance Analysis[29]. This tool is written in Fortran 77 and executes on both Windows and UNIX platforms. Contrary to the name, the tool is more commonly used for scramjet engine performance prediction. RJPA uses thermally perfect gas (TPG) models with reacting flows and some empirical models. The chemistry model is based on the NOTS equilibrium routine and can support a wide variety of fuel and oxidizer combinations [30].

The user must provide inlet pressure recovery and capture efficiencies based on a vehicle forebody design determined and analyzed beforehand. Mass flow choking in the diffuser or combustor sections will result in the lack of a solution being obtained. For thermal choking in the combustor, the user must manually decrease the fuel flowrate. The nozzle analysis performs an isentropic flow expansion from the combustor exit with either frozen or equilibrium flow options.

The text based user interface is easy to manipulate and the code executes on the order of few seconds for a single flight condition. RJPA could be used in a design environment with additional scripting software and analysis tools for the capture efficiency and pressure recovery values. An efficiency factor is then be applied to the nozzle flow's exiting momentum.

One additional note is that all of the component analysis performed in RJPA are performed by utilizing the conservation laws to balance the entering fluid properties with the exiting fluid properties. Details of what exactly is occurring between the entering and exit planes of the engine components are not known. This type of solution technique is commonly referred to as a 'jump' code, meaning the analysis jumps from the beginning of a component to the end as opposed to marching through the component in discrete steps or analyzing in n-dimensions. This technique can arrive at a solution faster, but requires more information to be specified in order to obtain accurate results (eg. the wall pressure integral, flow Mach number regime) and can be prone to not converging to a solution.

2.3.3 RAMSCRAM

RAMSCRAM, which stands for RAMjet SCRAMjet, is available from NASA Glenn Research Center [31]. This code is very similar to RJPA, but is more commonly used for subsonic-combustion ramjet analysis and less for scramjet analysis. The code executes on both UNIX and Windows based machines and is written in Fortran 77.

RAMSCRAM features a similar chemistry model to RJPA and is a jump code (i.e. no marching solutions). Its text-based input files are somewhat unwieldy due to poor variable name declarations. Unlike RJPA and HAP, RAMSCRAM is capable of performing 2-D

vehicle forebody analyses with multiple compression surfaces. Another advantage is that RAMSCRAM is more flexible in terms of its engine geometry and component setup, thus it supports a wider range of propulsion system configurations. As an example, the user can specify multiple combustor sections/breaks and fuel injector locations. Execution speeds are on the order of a few seconds for a single flight condition on a 350 MHz R12000 Unix Workstation.

2.3.4 SRGULL

Without going to the extreme case of generating an entire CFD model of an engine, the highest fidelity tool currently available for performance analysis is SRGULL [32,33]. SRGULL was developed during the National Aerospace Plane (NASP) program to design and analyze ramjet and scramjet propulsion concepts. SRGULL is written in Fortran 77 and can be operated on either a Windows or UNIX platform.

SRGULL uses a 2-D Euler solver, called SEAGULL [34], for the external flows (i.e. forebody, nozzle) and a 1-D equilibrium flow model internally. A boundary-layer routine based on the Spalding-Chi method is also incorporated to provide skin friction losses. SRGULL can currently only support studies using hydrogen and octane fuels, but an expanded chemistry model with additional fuel options is currently being incorporated and verified. An optional liquid oxygen injector can be selected for augmenting scramjet performance at high flight Mach numbers, but it does not support a true rocket (i.e. reacted fuel and oxidizer injection) type of augmentor. Unfortunately, SRGULL can only analyze ramjet and scramjet engines for started inlets in supersonic flight. It also requires significant setup time and is not considered to be a very robust code. The number of input parameters that must be specified for an engine configuration is on the order of 300. Execution time is

approximately 2-3 minutes for a single flight condition on a 667 Mhz Intel Pentium III© PC or 350 Mhz R12000 UNIX workstation. This tool is not suited for use in conceptual design or in a highly iterative design environment.

CHAPTER III

PROPULSION SYSTEM PERFORMANCE MODELING

In order to accurately predict engine performance, the fluid flow properties (eg. velocity, temperature, pressure, enthalpy, specific heat) internal to and surrounding the engine must be determined. These parameters will vary depending upon the engine's specific operating conditions (eg. freestream Mach number, vehicle altitude) and design. The conservation equations for mass, momentum, and energy are needed to determine these property values. The solution process is often iterative at a given engine station or between a given downstream and upstream station.

The flow modeling equations and assumptions to be presented next are mainly applicable to the types of engine configurations discussed in previous chapters. While the conservation equations are applicable to almost all flows, their specific form presented will be based on certain assumptions regarding the engine geometry, propellant addition locations, and expected or assumed flow responses.

3.1 Engine Components

Figures 3.1 and 3.2 show generic representations of a pure A/B engine (non-RBCC) and a RBCC engine with various locations or stations in the engine denoted by a number or symbol. Starting at the freestream flow (∞), the engine is classified or broken up into different components. Depending on the engine classification, the exact components comprising the engine system will vary. The common components present in any airbreathing system are: external compression system (∞-1), inlet/diffuser (1-2), combustor (3-4), and nozzle (4-e).

For RBCC systems, there is an additional rocket subsystem in the flowpath. The rocket exhaust interfaces with the core flow in the 'mixer' section. Additionally, some RBCC variants incorporate a limited amount of turbomachinery. These variants are known as 'supercharged' and use a single stage, gas-generator powered tip-driven compressor simply referred to as the 'fan' system.

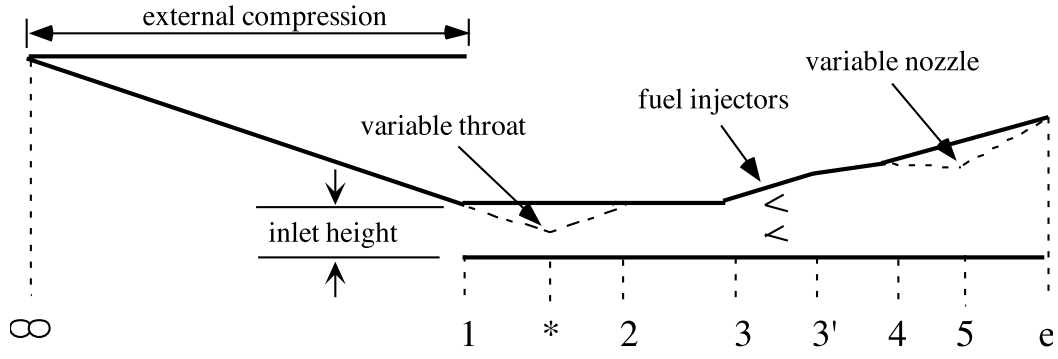

Figure 3.1 Airbreathing Engine Components

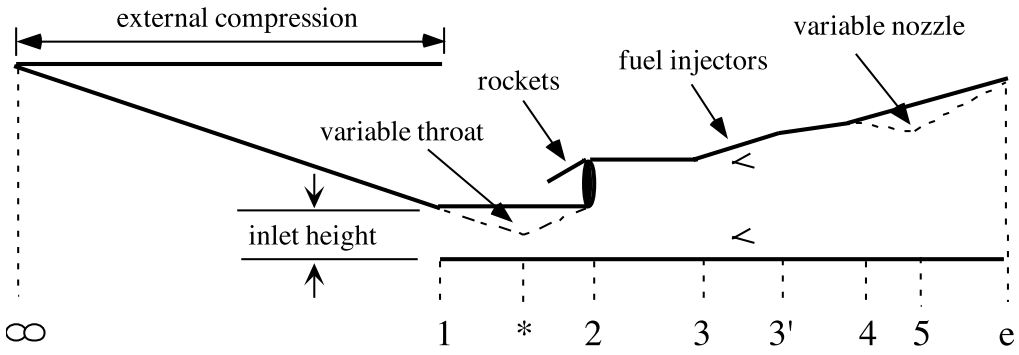

Figure 3.2 RBCC Engine Components

Next, analysis methods suitable for use in conceptual design will be presented. These methods will determine the flow properties across each of the aforementioned engine components and correspond to the station locations identified in Figures 3.1 and 3.2.

3.2 Basic Flow Equations and Assumptions

At the conceptual and preliminary stages of advanced propulsion system design, a number of flow assumptions can be made. Typically, the engine flow is assumed to be 1-D or quasi 1-D, meaning axial variations in the flowfield are functions of area only. The primary equations used are the conservation equations for mass(continuity), momentum, and energy. The form of these are provided in Equations 3.1, 3.2, and 3.3 respectively[35].

$$\dot{m}_i = \rho_i V_i A_i \tag{3.1}$$

$$\dot{m}_{i+1} V_{i+1} + P_{i+1}A_{i+1} = \dot{m}_i V_i + P_i A_i + \int_i^{i+1} PdA \tag{3.2}$$

$$h_{s,i+1} + \frac{1}{2}V_{i+1}^2 = H_t = h_{s,i} + \frac{1}{2}V_i^2 \tag{3.3}$$

The '*i*' subscript identifies and corresponds to a specific location in the engine. For a particular design, the area at any location (A_i) will be known. The mass flow rate, $\dot{m}_i$, initially involves a calculation to determine its value at station '1', but it is then known for *i*=2,...,e. Any added propellant ($\dot{m}_{rocket}$ or $\dot{m}_{fuel}$) will be either a specified value or a function of $\dot{m}_i$. The density in Equation 3.1 can be found by assuming an ideal gas, as shown in Equation 3.4.

$$P_i = \rho_i \frac{R_{universal}}{\mathcal{MW}_i} T_i \tag{3.4}$$

Note that the mass flow rate, $\dot{m}_i$, is composed of numerous species (eg. nitrogen, oxygen, argon). The general form for its calculation is shown in Equation 3.5, along with the mixture's molecular weight ($\mathcal{MW}_i$) in Equation 3.6, where $Y_{i,j}$ is the mass fraction of the species '*j*' at station '*i*'.

$$\dot{m}_i = \sum_{j=1}^{N_{species}} \dot{m}_{i,j} \tag{3.5}$$

$$\mathcal{MW}_i = \frac{1}{\sum_{j=1}^{N_{species}} \frac{Y_{i,j}}{\mathcal{MW}_j}} \tag{3.6}$$

Referring back to the conservation laws, Equation 3.2 states the momentum conservation between any two locations. The final term on the right hand side of this equation is referred to as the wall-pressure integral. There are various techniques for finding this contribution to the momentum term (eg. Crocco's P-A relationship[36], direct integration). For constant area regions, this term will be zero (dA=0).

In Equation 3.3, the total enthalpy (H_i) is composed of the static sensible enthalpy (h_s) and the kinetic energy ($\frac{1}{2}V^2$) of the flow. For frozen flow assumptions, the enthalpy is a function of the flow temperature and composition. For equilibrium flows, the composition is dependent on the flow pressure and temperature, thus the enthalpy also becomes implicitly pressure dependent. This dependency also extends to the flows specific heat, Cp, which is the partial derivative of the enthalpy with respect to temperature at a constant pressure.

$$\text{Frozen:} \quad h_s = f(T, \dot{m}_j) \quad j=1\ldots N_{species} \tag{3.7}$$

$$\text{Equilibrium:} \quad h_s = f(T, P, \dot{m}_j) \quad j=1\ldots N_{species} \tag{3.8}$$

$$Cp = \left.\frac{\partial h}{\partial T}\right)_P \tag{3.9}$$

3.2.1 External Compression

The freestream flowfield typically experiences a significant amount of compression due to the presence of the vehicle forebody or an inlet 'spike'. The analysis method used to model this compression depends on the exact flight conditions and geometry of the compression surface. Figures 3.3 and 3.4 show samples of two common compression system designs and the resultant flowfield gradients associated with each.

The most common compression surfaces are either the 2-D 'wedge' shapes, or 3-D 'cone' shapes. At subsonic speeds, there is only a small 'compression' effect and this influence on the flowfield can be ignored (i.e. no loss in total pressure). Recall that these methods are for conceptual-level analysis. The time involved and increase in computing resources necessary to resolve the subsonic flowfield is inconsistent with the available resources for this phase of the design. If necessary, empirical data is available for computing 3-D cone static surface pressures from Mach 0.3 to 0.8 [37]. At supersonic speeds, these surfaces will generate oblique shockwaves and the flowfield can be quickly analyzed to a reasonable degree of certainty. For these cases, static pressure rises from the freestream value can be on the order of 5 to 10, depending on the level of flow contraction.

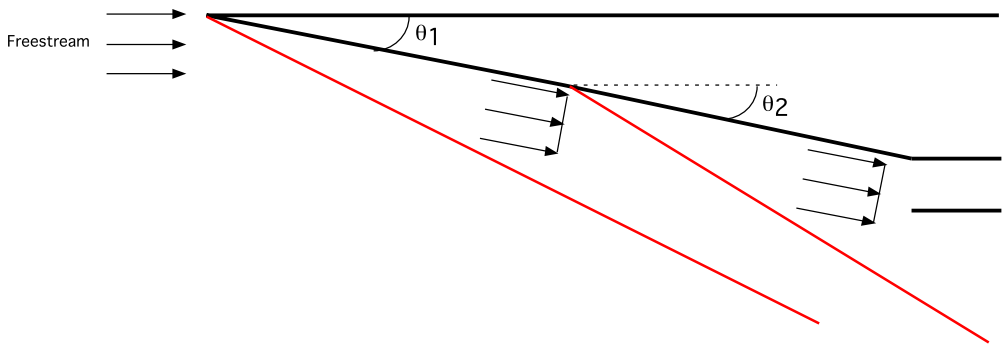

Figure 3.3 2-D Forebody Compression System

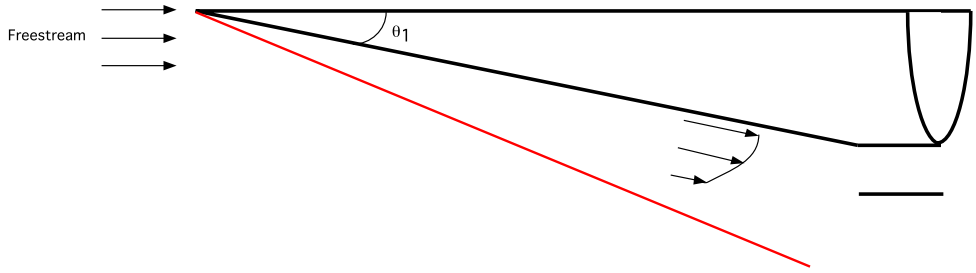

Figure 3.4 Conical 3-D Forebody Compression System

2-D Compression

For 'wedge' geometries (Figure 3.3), the flowfield behind the shockwave(s) will remain 2-D, although there can be multiple regions of different 2-D flows. These compression surfaces can be analyzed using oblique shock relations. Note that more than one of these ramps can be present to minimize the flow losses obtained for the same amount of compression as a single ramp at a higher angle. In order to have the highest degree of generality and applicability, the thermally perfect form of these equations should be implemented. The equations needed to resolve this flowfield are presented in Equation's 3.10-3.12.

$$P_{s,y} - P_{s,x} = \rho_x V_{N,x}^2 \left(1 - \frac{\rho_x}{\rho_y}\right) \tag{3.10}$$

$$h_{s,y} - h_{s,x} = \frac{V_{N,x}^2}{2}\left(1 - \left(\frac{\rho_x}{\rho_y}\right)^2\right) \tag{3.11}$$

$$\frac{\rho_x}{\rho_y} = \frac{(\gamma+1)M_x^2 \sin^2\beta}{\left(2 + (\gamma-1)M^2 \sin^2\beta\right)} \tag{3.12}$$

The subscript 'x' denotes known properties upstream of the shockwave and subscript'y' denotes the unknown values to be solved for downstream of the shockwave. The 'N' subscript denotes the velocity component normal to the shockwave. The enthalpy ($h_{s,y}$) is a function of the static temperature ($T_{s,y}$). The solution process is iterative and involves assuming a shockwave angle, β' [38]. As a good initial starting value, the CPG closed-form approximation for β' can be used, as shown in Equation 3.13 [39].

$$\beta = \sin^{-1}\left(\sin(\delta)\left(\left(\frac{\gamma+1}{4}\right) + \sqrt{\left(\frac{\gamma+1}{4}\right)^2 + \frac{1}{M_\infty^2 \sin^2(\delta)}}\right)\right) \tag{3.13}$$

where δ is the turning angle of the flow. With the value of β' specified, the Equations 3.10-3.12 can be solved iteratively. After their solution is obtained, the actual shockwave angle, β, can be computed numerically, as shown in Equation 3.14. If this angle does not match the assumed shockwave angle (β'), a new value is assumed and the procedure executed again.

$$\beta = \delta + \sin^{-1}\left(\frac{V_{Ny}}{V_y}\right) \tag{3.14}$$

Note that this process is for analyzing the flow across a single compression surface or

ramp. For vehicle geometries with multiple ramps, this procedure is executed for every ramp, with the turn angle (δ) being the difference between two adjacent ramp angles (θ_i and θ_{i+1}). Also note that vehicle angle-of-attack (α) effects can easily be incorporated into the analysis by increasing the first ramp's angle by α.

3-D Compression

For determining the properties behind the bow shock of a conical 3-D surface, a system of ordinary differential equations (ODE's) must be solved. The reverse procedure of guessing a shock angle, as recommended by Anderson, is implemented to solve these equations along with a Predictor-Corrector (P-C) integration routine [39,40]. The P-C routine provides good overall convergence rates and only requires a two step process for each integration step. Small integration stepsizes will be necessary to sufficiently resolve the flowfield between the cowl leading edge and vehicle body. The ODE's are shown here in their more familiar spherical coordinate form as:

$$V_\theta = \frac{dV_r}{d\theta} \tag{3.15}$$

$$\frac{dV_\theta}{d\theta} = \left(\frac{a^2}{V_\theta^2 - a^2}\right)\left(2V_r + V_\theta \cot\theta - \frac{V_r V_\theta^2}{a^2}\right) \tag{3.16}$$

$$\frac{dp}{d\theta} = \left(\frac{-\rho V_\theta a^2}{V_\theta^2 - a^2}\right)\left(V_r + V_\theta \cot\theta\right) \tag{3.17}$$

where a is the speed of sound, θ is the ray angle from the tip of the cone, V_r is the radial velocity component, V_θ is the normal velocity component perpendicular to the radial

component, p is the static pressure, and ρ is the density of the flow. Note that this equation set is based on the assumption of flow symmetry around the entire cone surface, thus it is only sufficient for analysis at zero-alpha conditions. For cones at non-zero alpha, the flow equations become much more complex (PDE's) and cannot be solved in a manner consistent with the design phase. A 3-D Method of Characteristics (MOC) solution is possible although difficult to implement and still fairly CPU intensive [41].

Skin Friction

Along the vehicle forebody, skin friction effects will be significant. The magnitude of the shear stress on the vehicle forebody is largely dependent on whether the boundary layer is laminar or turbulent and a variety of empirical models can be used to predict the location of this transition. The simplest model to account for friction effects uses an average skin friction ($C_{f,forebody}$) coefficient across the length of the forebody. This average C_f can be a function of flight conditions (eg. Mach number) for additional fidelity. An appropriate value for C_f can be obtained from higher level analysis tools (eg. boundary layer equations). For a specified average $C_{f,forebody}$, the axial frictional force ($F_{friction,x}$) can be computed as shown in Equation 3.18, where S_x is the wetted surface area of the vehicle forebody in the axial direction of the 2-D or 3-D compression surface. The effect of friction in the normal direction ($F_{friction,y}$) could be included, but will be ignored.

$$F_{friction,x} = \frac{1}{2}\rho_\infty V_\infty^2 C_{f,forebody} S_x \tag{3.18}$$

Other more sophisticated, non-constant values for $C_{f,forebody}$ can also be obtained by incorporating the Reynolds number and a boundary layer thickness estimate.

3.2.2 Internal Compression

The purpose of the'inlet' is to trap the airflow from the forebody and attempt to align the flow for the combustor. This process should be done with the minimal amount of losses (i.e. entropy rise). In general, most engines will require variable geometry inlets and therefore this type of system is typically assumed to be available in any analysis. Variable geometry inlets allow for efficient operation over the wide flight corridor experienced by hypersonic launch vehicles as well as offer improved engine operability. As an additional performance and operability option, a portion of the boundary layer flowfield can be 'bled' from the inlet. The amount of flow bleed is typically specified as a percentage of the incoming mass flowrate and an appropriate reduction on $\dot{m}_1$ can be taken to reflect this. Bleeding flow can help to prevent flow separation, allowing for higher flow contraction ratios.

Total Pressure

The primary measure of inlet performance is the 'total pressure ratio', defined as the ratio of the total pressure at the diffuser exit ($P_{t,2}$) to the total pressure at the cowl leading edge ($P_{t,1}$) [42]. The total pressure value is a measure of the entropy in the system, therefore the ratio of the total pressures provides a measure of the shock strength and other non-isentropic effects in the inlet.

At subsonic flight conditions ($M_\infty<1$), inlet performance losses due to friction and wall heat transfer will be negligible. It is therefore common to assume no losses in total pressure ($\Delta P_{t,1\text{-}2}=1$).

For supersonic flight Mach numbers below Mach 6, it is acceptable to compute the total pressure at station '1' using in Equation 3.19. Between station '1' and station '2', the total pressure decrease through the inlet can be determined by specifying a total pressure ratio performance map. This pressure ratio map is typically a function of the Mach number at the cowl leading edge and can be obtained from an off-line inlet analysis, by assuming ideal inlet operation, or from actual test data. If a supercharging fan is present and operating, the total pressure at station '2' is subsequently adjusted by the fan pressure ratio ($P_{t,fan}/P_{t,1}$). Typical single-stage fan pressure ratios range from 1.1 to 1.5. The total enthalpy from station '1' to station '2' is constant if the inlet walls are assumed to be adiabatic. Ignoring the enthalpy contribution from the fan is acceptable since the fuel required to drive the fan is generally not accounted for and these two factors are assumed to cancel each other out.

$$P_t = P_s\left(1 + \frac{\gamma - 1}{2} M^2\right)^{\frac{\gamma}{\gamma - 1}} \tag{3.19}$$

For flight Mach numbers above Mach 6, the usefulness of the total pressure parameter decreases and its calculation becomes much more complex. Eliminating the CPG assumption and assuming that the total temperature, static temperature, and static pressure are known, the total pressure can be computed by assuming an isentropic process, as in Equation 3.20 [43].

$$P_t = P_s \exp\left(\frac{MW}{R_{universal}} \int_{T_s}^{T_t} Cp \frac{dT}{T}\right) \tag{3.20}$$

Subsonic Flight

For subsonic flight conditions, the mass flowrate at the cowl face is not known because the flowfield cannot be resolved. The subsonic flow is aware of the cowl and forebody downstream and can react to it, destroying any flow streamline uniformity. Thus, for flight Mach number less than ~1.2, the mass flow at the inlet is computed based on the maximum flowrate that can pass through the inlet/diffuser system. This value is based on the freestream total pressure, total temperature, and geometry. Assuming a sonic flow at the minimum area in the inlet/diffuser system, Fleigner's Formula provides the amount of captured air flow in the engine (see Equation 3.21)[38].

$$\dot{m}_1 = \left(\frac{2}{\gamma+1}\right)^{(\gamma+1)/2/(\gamma-1)} \frac{A_{\min} P_{t,1}}{\sqrt{T_{t,1}}} \sqrt{\frac{\gamma \cdot MW}{R_{universal}}} \tag{3.21}$$

Supersonic Flight

When equation set 3.10-3.12 or 3.15-3.17 are solved, the flowfield behind the shock system is completely defined and the properties upstream of the cowl are known. The static property gradients can be integrated from the vehicle's surface to the cowl leading edge, to obtain the total mass flowrate of air ($\dot{m}_1$) into the engine and the total momentum at the cowl leading edge (M_{cowl}), as shown in Equations 3.22 and 3.23. These will be critical parameters in computing engine forces later. Additionally, average static and total properties at the cowl leading edge can be defined using area-weighted values.

$$\dot{m} = \int_0^{h_{cowl}} (\rho V) dA \tag{3.22}$$

$$\mathrm{M}_{cowl} = \int_{o}^{h_{cowl}} \left(\rho V^2 + P\right) dA \tag{3.23}$$

If the vehicle operating condition is such that all the shocks from the compression surface are 'swallowed' by the inlet, the engine is said to be operating at "100% capture efficiency" and the inlet is oversped (i.e. operating above its design point). The mass capture can be computed by projecting the frontal area of the engine and forebody out to the undisturbed freestream flow. This area is then used in the continuity equation, along with the freestream properties to get the total mass flow into the engine. The momentum at the cowl leading edge can be determined in a similar manner. A freestream momentum flux can be calculated and the forces on the forebody subtracted off of this value to obtain M_{cowl}, as shown in Equation 3.24.

$$\mathrm{M}_{cowl} = \mathrm{M}_{freestream} - \sum_{i=1}^{N_{ramps}} \left(P_{s,i} - P_{\infty}\right) S_{i,x} \tag{3.24}$$

Subsonic Combustion

For subsonic combustion cases, a normal shock will exist in the diffuser section (see Figure 3.5). It is desirable to have the flow just upstream of this shock at the lowest possible Mach number to minimize any losses. Note that the position of this shock system is dependent on the downstream throat area (at station 5) and will vary continuously during flight. Engine performance and operation dictate that the shock location must be downstream of the inlet throat (station *).

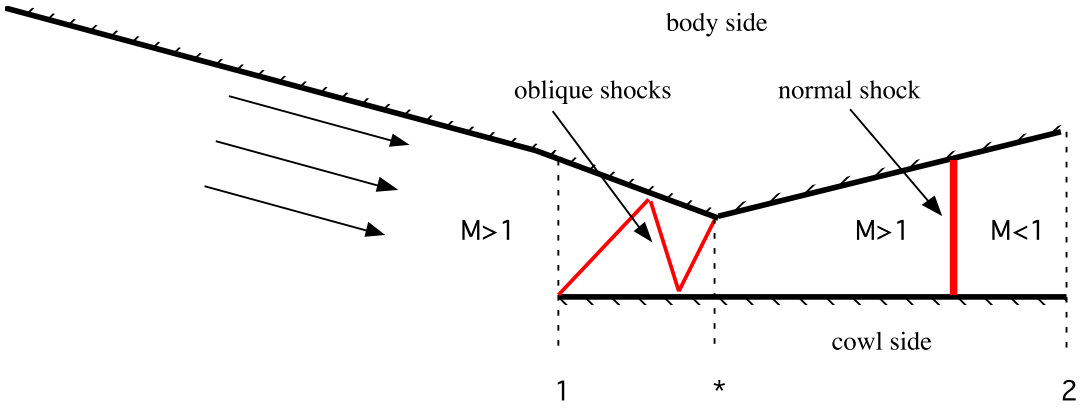

Figure 3.5 Subsonic Combustion Inlet Operation

With a known air mass flowrate ($\dot{m}_1$), diffuser exit area (A_2), total pressures ($P_{t,1}$ and $P_{t,2}$) and total temperature at the cowl leading edge ($T_{t,1}$), the solution for the Mach number at station '2' is iterative. For a guessed, subsonic Mach number, the flow static temperature and static pressure at '2' are found from the adiabatic, CPG equation for total temperature and the total pressure from Equation 3.19. The velocity at station '2' can then be determined using the definition of Mach number. With all the fluid properties now calculated, the mass flowrate can be calculated using Equation 3.22. This value needs to match the actual known value computed as entering the engine from the freestream flow. A bisection routine that finds the Mach number that drives the difference between these two calculated mass flowrates to zero is suggested.

Supersonic Combustion

For higher flight Mach number cases, an alternate inlet analysis method is required and involves performing an oblique shock analysis on the flow entering the inlet. A supersonic flow entering the engine will be aligned with the final forebody ramp angle. When this flow

intersects the cowl side of the engine, it will be forced to turn and align with the cowl (see Figure 3.6). This turning is accomplished through the generation of an oblique shock. Depending upon the inlet geometry, there can be multiple shocks reflecting the flow off both the cowl and body side. The inlet performance can be assessed by assuming a uniform flowfield at station '1' and analyzing the flow as it passes through these oblique shocks (see Equations 3.10-3.12). For flows with gradients, area averaged flow properties can be defined. The change in static temperature, pressure, and velocity through the inlet can then be obtained. For supersonic flows, there will not be a normal shock present in the diffuser and the flow is expanded to the area specified at the diffuser exit (station 2). Note that a pressure recovery schedule is not required for this analysis.

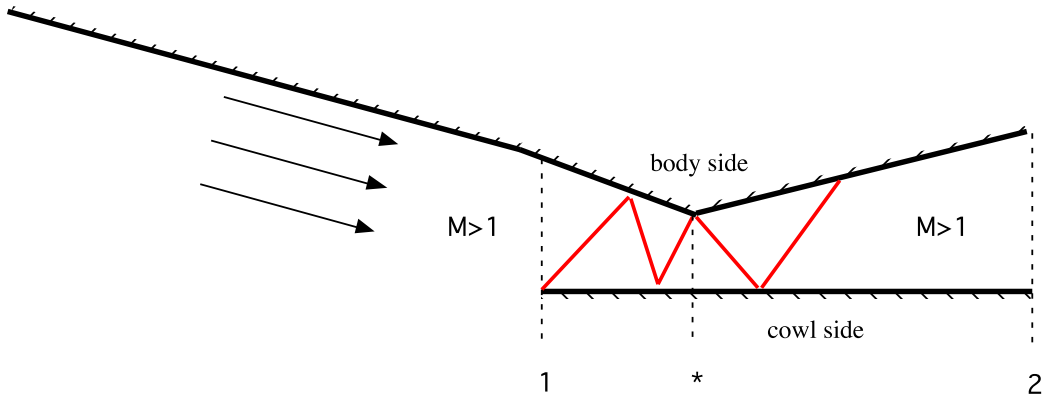

Figure 3.6 Supersonic Combustion Inlet Operation

Although this alternate method is also applicable for the subsonic combustion case during supersonic flight, this technique is more computationally intensive than the first. The increased fidelity due to this method will not be realized at the lower flight Mach numbers typical of subsonic-combustion cases because the CPG assumption is valid. Thus, in the interest of computational efficiency, this method is reserved for higher flight Mach number operation (i.e. supersonic combustion cases).

Unstart

If the flight conditions and forebody compression system provide a mass flowrate that exceeds the maximum mass flow that can be passed through the inlet throat, then a normal shock will develop upstream of the cowl leading edge (i.e. between '∞' and '1') and the inlet is referred to as 'unstarted'. Due to the strength of the normal shock, this unstart can result in a dramatic decrease in the engines total pressure and thrust. Some unstarts can be severe enough that the engine does not produce any thrust. This phenomenon typically occurs below flight Mach numbers of three, but may occur at higher Mach numbers for engines with high internal flow contraction ratios.

To check if an inlet is 'started' or 'unstarted', Fleigners formula can be used to compute the maximum amount of flow the inlet can accommodate. If this value is less than the mass flowrate value obtained using Equation 3.22, the inlet is unstarted. In this case, a normal shock can be positioned at station '1' and the flowfield analyzed as it passes through it. The total pressure drop and static flow properties can be calculated using equation set 3.10-3.12 with $\beta=90^{o}$. Fleigner's formula can be reapplied using the new static and total properties downstream of the shockwave to determine the new mass flow into the inlet.

The unstart phenomenon is not solely a function of engine geometry. Even in scramjet mode, with supersonic flow throughout the engine, downstream disturbances in the engine (eg. fuel injection) can propagate forward through the subsonic boundary layer and cause the inlet to unstart. Unfortunately, this type of calculation is beyond the level of conceptual propulsion system analysis and design.

3.2.3 Rocket Thruster Subsystem

The rocket system is critical to vehicle operation. It provides the initial thrust to get the vehicle moving, off the ground, and up to ramjet takeover speeds. The thrusters are also the primary propulsive device above Mach 10-15 and provide the final boost to orbital insertion. Figure 3.7 shows two notional sketches of what these imbedded rocket thrusters typically look like.

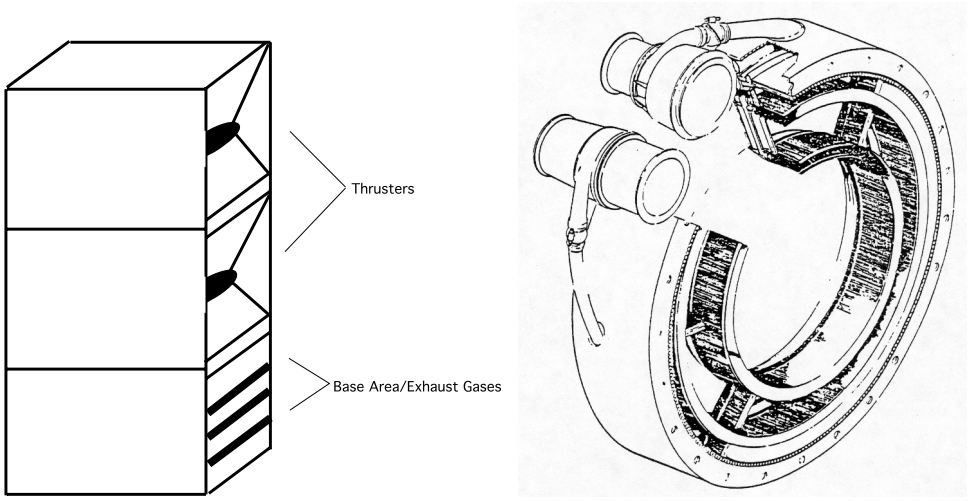

(A) (B)

Figure 3.7 Sample Rocket Thruster Hardware

Chemical Equilibrium Analysis

In order to assess the rocket system performance and flow properties, the exhaust products due to the combustion process in the rocket chamber must be determined. The most suitable and efficient method for accomplishing this is through the minimization of the Gibbs energy[44,45,46]. The Gibbs minimization requires the solution of a system of simultaneous, non-linear equations. The number of equations that must be solved is

dependent upon the number of different atoms present in the rocket propellants. The general form of the equations to be solved is shown in Equation 3.25 and 3.26. Appendix A provides the variable descriptions and appropriate matrices with atomic coefficients for a five atom (l=5; C, H, N, O, Ar) system with twelve potential products ($N_{species}$=12; H_2, O_2, H, O, OH, H_2O, N_2, N, NO, Ar, CO, CO_2). The subscript 'k' also represents the five atoms, thus Equation 3.25 represents five equations when expanded, for a total of six to be solved.

$$\sum_{i=1}^{l}\sum_{j=1}^{N_{species}} a_{kj}a_{ij}n_j\pi_i + \left(\sum_{j=1}^{N_{species}} a_{kj}n_j\right)\Delta\ln n = b_k^o - b_k + \sum_{j=1}^{N_{species}} \frac{a_{kj}n_j\mu_j}{RT} \qquad (3.25)$$

$$\sum_{i=1}^{l}\sum_{j=1}^{N_{species}} a_{ij}n_j\pi_i + \left(\sum_{j=1}^{N_{species}} n_j - n\right)\Delta\ln n = n - \sum_{j=1}^{N_{species}} n_J + \sum_{j=1}^{N_{species}} \frac{n_j\mu_j}{RT} \qquad (3.26)$$

For a known temperature, reaction pressure, and initial atom ratios, these equations can be solved using a Newton-Rhapson (N-R) root finder [40]. The N-R routine is fairly simple to program but requires initial guesses to be made. This routine has also been demonstrated as one of the most efficient methods for solving simultaneous non-linear equations sets. At each iteration, a matrix form of Equations 3.25 and 3.26 is solved using a Lower-Upper Matrix (LU) Decomposition algorithm with complete pivoting [47]. The LU algorithm requires about the same number of mathematical operations as a traditional Gaussian Elimination method. But, the addition of the 'complete pivoting' step reduces truncation and round-off errors by reducing the chance of division operations with small numbers. Each solution for the matrix system results in correction terms for the number of moles for each species in the system ($\Delta\ln n_i$), as well as a correction for the total number of moles present

($\Delta \ln n$). An initial guess for each of the product moles (n_i) equal to $1/N_{species}$ is made, as suggested by Gordon and McBride[44].

For a rocket analysis, it is necessary to balance the final enthalpy of the system with the initial enthalpy. Since the equilibrium analysis is designed to analyze a reaction with a specified temperature, an iterative procedure of guessing a temperature to match the required enthalpy is used. By specifying the initial fuel and oxidizer temperatures, the total enthalpy of the propellants can be determined, as shown in Equation 3.27. A bisection routine is used to determine the flame temperature of the system that matches the required enthalpy, assuming an adiabatic, constant-pressure process. Note the small enthalpy contribution due to the injection velocity of fuel and oxidizer is ignored.

$$H_{t,required} = \frac{\left(\dot{m}_{fuel}\left(h_{f,fuel} + h_{s,fuel}\right) + \dot{m}_{oxidizer}\left(h_{f,oxidizer} + h_{s,oxidizer}\right)\right)}{\left(\dot{m}_{fuel} + \dot{m}_{oxidizer}\right)} \tag{3.27}$$

Once all the combustion products have been determined, the performance of the rocket system can be assessed using isentropic flow equations. By specifying an expansion ratio (ε), the exit Mach number ($M_{rocket,e}$) can be found through iteration[48]. For this iteration, the bisection method was used. Lower and upper bounds of one and ten on the Mach number force the supersonic solution to occur. The iteration procedure involves solving Equation 3.28 until the computed expansion ratio matches the specified expansion ratio.

$$\varepsilon = \frac{1}{M_{rocket,e}} \sqrt{\left\{\frac{2}{\gamma + 1}\left(1 + \frac{(\gamma - 1)}{2} M_{rocket,e}^{\ 2}\right)\right\}^{\frac{\gamma+1}{\gamma-1}}} \tag{3.28}$$

Once this method converges upon the Mach number, the exit static pressure to chamber pressure ratio (P_e/P_c) can be found from the isentropic relationship:

$$\left.\frac{P_e}{P_c}\right)_{rocket} = \frac{1}{(1+\frac{(\gamma-1)}{2}M_{rocket,e}{}^2)^{\gamma/(\gamma-1)}} \tag{3.29}$$

The specific impulse of the rocket can then be found from Equation 3.30.

$$Isp = \frac{c^* Cf}{g_o} \tag{3.30}$$

where g_o is the acceleration due to gravity on the Earth's surface and the thrust coefficient (Cf) for the rocket is:

$$Cf = \left\{\frac{2\gamma^2}{\gamma-1}\left(\frac{2}{\gamma+1}\right)^{\frac{\gamma+1}{\gamma-1}}\left[1-\left(\frac{P_e}{P_c}\right)^{\frac{(\gamma-1)}{\gamma}}\right]\right\}^{0.5} + \varepsilon\left[\frac{P_e}{P_c}-\frac{P_\infty}{P_c}\right] \tag{3.31}$$

and the characteristic velocity (c*) is:

$$c^* = \frac{\sqrt{\gamma R T_c}}{\gamma\sqrt{\left(\frac{2}{\gamma+1}\right)^{\frac{\gamma+1}{\gamma-1}}}} \tag{3.32}$$

The actual thrust produced from the rocket subsystem can then be found using the total mass flowrate as:

$$T_{rocket} = Isp \cdot \dot{m}_{rocket} \tag{3.33}$$

Additionally, the combustor exit temperature ($T_{s,rocket,e}$) and exit velocity ($V_{rocket,e}$) can be found from:

$$T_{s,rocket,e} = \frac{T_{t,rocket}}{\left(1 + \frac{(\gamma - 1)}{2} M_{rocket,e}^2\right)} \tag{3.34}$$

$$V_{rocket,e} = M_{rocket,e} \sqrt{\frac{\gamma \cdot R_{universal} T_{s,rocket,e}}{MW_{rocket}}} \tag{3.35}$$

3.2.4 Mixer

For ramjet and scramjet engines, the 'mixer' region simply becomes an extension of the diffuser section. For RBCC systems, the 'mixer' section mixes the incoming air stream with the rocket exhaust stream into an ideally uniform and full-mixed flow (see Figure 3.8). This flow can be reacting or non-reacting, depending upon the mixture ratio of the rocket system, static flow conditions, and degree of mixing. Generally, a small amount of chemical reaction will occur due to the high rocket exhaust temperatures and oxygen from the airstream.

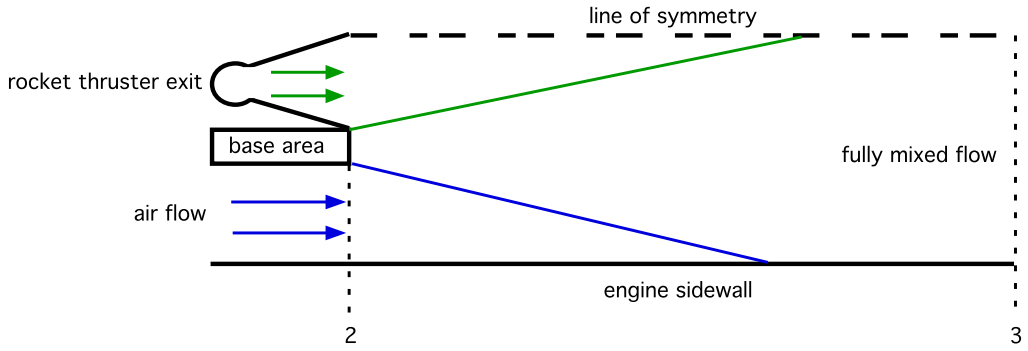

Figure 3.8 RBCC Engine Mixer Section Diagram

The mixer is typically of constant cross sectional area, where the flow area at station '3' is the sum of the rocket thruster's exit area(s), base area(s), and the diffuser exit area, as shown in Equation 3.36.

$$A_3 = A_2 + \sum_{i=1}^{No.Thrusters} A_{rocket,i} + A_{base} \tag{3.36}$$

where A_{rocket} is a function of the rocket expansion ratio and the base area, A_{base}, can be set independently. A_2 can be a 'pinch point' in the engine (non-adjustable throat area) and will influence where the inlet will start. The base area region is typically filled with hot exhaust gases from the rocket and/or fan's gas generator engine. The pressures acting on this region are assumed to be at half the diffuser exit pressure, or as the average between the rocket exhaust and diffuser exit pressure. Similarly, if the rocket is not ignited (no exhaust present), the rocket thruster exit area is assumed to be pressurized too.

The total mass flowrate at the mixer exit ($\dot{m}_3$) is the combined flowrates of the rocket exhaust and air stream. Similarly, the total enthalpy for the flow at the mixer exit ($H_{t,3}$) is the combined enthalpies of the rocket and air stream. These computations are shown in Equations 3.37 and 3.38. Note that the enthalpy equation assumes an adiabatic flow, as there are no sources of heat loss in the equation.

$$\dot{m}_3 = \dot{m}_2 + \dot{m}_{rocket} \tag{3.37}$$

$$H_{t,3} = \frac{\dot{m}_{rocket} H_{t,rocket} + \dot{m}_2 H_{t,2}}{\dot{m}_3} \tag{3.38}$$

The solution for the flow properties exiting the mixer requires a multi-step process. The first step involves solving for the ideal flow conditions (i.e. no losses). The next step involves accounting for the losses in the flow by applying an efficiency factor. Finally, the flow properties at station '3' are again solved for with the losses now accounted for. Note that the air flow conditions at station '2' and the rocket mass flowrate ($\dot{m}_{rocket}$), exit area (A_{rocket}), exhaust velocity (V_{rocket}), enthalpy ($h_{s,rocket}$), and exit pressure ($P_{s,rocket}$), are all known quantities in solving for the mixer section flow properties.

For the first step, the solution process begins by assuming a static temperature ($T_{s,3}$) for the flowfield. With this temperature, the specific heat (C_p), ratio of specific heats (γ), molecular weight ($\mathcal{MW}_3$) and static enthalpy ($h_{s,3}$) based on the combined rocket exhaust and air flow are calculated at station '3'. Mass averaging techniques are used for C_p and the $\mathcal{MW}_3$. Note individual species' C_p's as functions of temperature are required. Using the energy

equation, the mixer exit velocity (V_3) can be determined. At this point, the Mach number can be computed and the guess for the static temperature adjusted to ensure either the subsonic or supersonic flow is obtained, as desired. For subsonic flows, if the Mach number check yields a supersonic value, the static temperature guess should be increased to reduce the velocity and hence the Mach number. Likewise, for supersonic flows, the static temperature guess should be decreased to increase the velocity if a subsonic Mach number is obtained. Next, the mixer exit pressure can be obtained from the momentum balance as shown in Equation 3.2, with dA=0 since the mixer has a constant area. To check that the assumed static temperature is correct, the continuity equation is used. The mass flowrate based on the static properties, velocity, and mixer exit area is compared with the known value equal to the sum of the air stream ($\dot{m}_2$) and the rocket exhaust flowrate ($\dot{m}_{rocket}$). If the two values due not agree, the assumed temperature is adjusted and the entire process is repeated to a recommended tolerance of 0.5%. Once the solution for the ideal flow in the mixer has been obtained, the total pressure at the mixer exit can be computed using Equation 3.20.

The second step is to compute the ideal total pressure ($P_{t,3,ideal}$) and then apply a mixer efficiency (η_{mixer}). This efficiency accounts for non-reversible effects in the flow (eg. friction and shocks). This adjusted total pressure is now the actual total pressure in the mixer. Typical values for η_{mixer} are between 85-95%.

$$P_{t,3} = \eta_{mixer} P_{t,3,ideal} \tag{3.39}$$

For the third step, the corrected total pressure is used in place of the momentum balance equation. An identical procedure to that used in step one is conducted accept instead of determining the static pressure using the momentum balance equation the static pressure

based on the corrected total pressure is used. Additionally, if reacting flow effects are to be accounted for, a chemistry routine can be integrated into this iteration process. The flow composition will become dependent on the static temperature and pressure. The new composition also effects the molecular weight, specific heat, specific heat ratio, and static enthalpy calculations.

3.2.5 Combustor

A computationally efficient, one-dimensional (1-D) combustor model that accounts for the effects of mass addition, heat addition, friction, and non-constant areas can be easily implemented. By utilizing a 'marching' solution technique, more detail and accuracy can be obtained in the combustor flow modeling. This marching solution eliminates the need to predict the wall pressure integral, as this quantity is already included in the discretized flow equations. The general setup for the combustor section is shown in Figure 3.9.

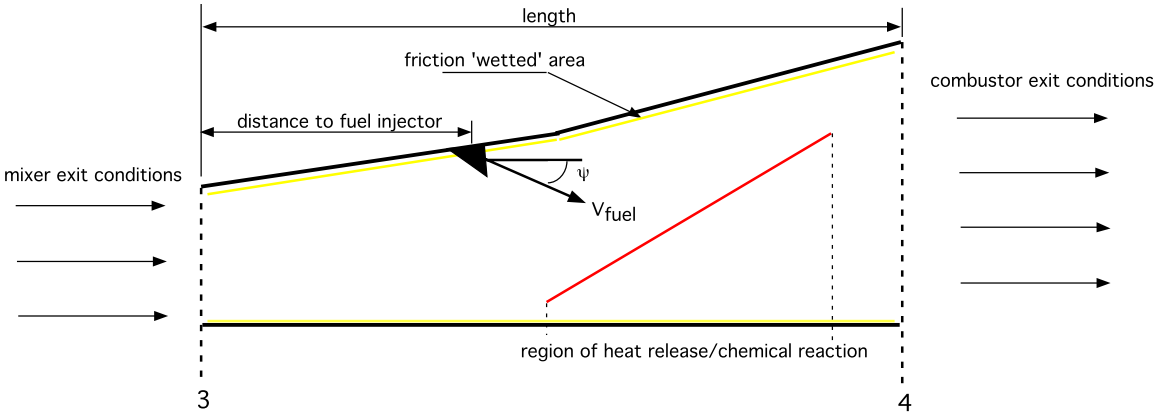

Figure 3.9 Combustor Section Diagram

Equation Set

The combustor model uses a common analysis method known as 'Influence Coefficients' [38]. This technique allows for all the flow properties to be determined by simply solving for the change in the Mach number throughout the combustor. The solution for the Mach number variation involves solving an ordinary differential equation of the form shown in Equations 3.40.

$$\frac{dM}{M} = C_1\left\{-\frac{dA}{A} + C_f\frac{\gamma M^2}{2}\left(\frac{S}{A}\right) + \frac{C_2}{2}\frac{dT}{T} + \left[C_2 - y\gamma M^2\right]\frac{d\dot{m}}{\dot{m}}\right\} \tag{3.40}$$

where,

$$C_1 = \frac{(1+\frac{\gamma-1}{2}M^2)}{1-M^2} \tag{3.40a}$$

$$C_2 = 1+\gamma M^2 \tag{3.40b}$$

The first term on the right hand side in Equation 3.40 is the impact on the Mach number due to area changes in the combustor. With specified combustor areas and length values, this term can easily be computed.

The second term in Equation 3.40 accounts for the effect of the wall shear stress on the flow. An average skin friction coefficient (C_f), can be defined as:

$$C_f = \frac{\tau}{q_{local}S} \tag{3.41}$$

where τ is a shear stress and q_{local} is the dynamic pressure computed using the local flow conditions. The variable 'S' is the flows local wetted surface area and is the mean area the flow experiences at a combustor step. This wetted area can be calculated for a variety of combustor geometries, either 2-D or 3-D in shape. Common average values for C_f in the combustor range from 0.001 to 0.002.

The third term is for the heat release due to chemical reactions. The 'influence coefficient' method requires that the heat release be specified in terms of a total temperature gradient. The procedure used for determining this will be discussed later.

The last term in Equation 3.40 is the contribution from the injected fuel's mass and velocity. This term is only nonzero at the location of the fuel injection. The '*y*' variable has the simple form shown in Equation 3.42.

$$y = \frac{V_{fuel}\cos(\psi)}{V_{stream}} \tag{3.42}$$

where V_{fuel} is the velocity of the fuel, ψ is the injection angle of the fuel, and V_{stream} is the velocity of the flow just upstream of the fuel injection position. If the fuel is injected normal to the flow, the injection angle is 90° and the value for '*y*' will be zero. If the injection angle is parallel to the flow (ψ=0°), '*y*' will have its maximum value and contribution to the flow momentum. If the fuel injection occurs at any other angle, the '*y*' term accounts for the axial momentum contribution of the fuel injection. Typical fuel injection velocities are from 2,000 to 4,000 fps, such that fuel injection Mach number is supersonic.

The main limitation of the influence coefficient method is due to an assumption made in its derivation. The influence coefficients assume a calorically perfect gas (CPG). The relatively

simple form presented above could not be achieved without this CPG assumption. Instead of Equation 3.40, it would be necessary to solve a set of partial differential equations. The CPG assumption typically does not hold above 2,000 R. But, by updating the specific heat and specific heat ratio at each spatial step, the usefulness of the technique has been expanded. This will be demonstrated and become evident in the subsequent verification process.

Solution Procedure

The conditions at the entrance to the combustor are known based on the outflow conditions from the mixer section (station 3) of the engine. To begin the analysis, the required flow properties are: the initial total enthalpy, static pressure, static temperature, Mach number, mass flow rates, and the rate of change in mass flowrate composition through the combustor $(\frac{d\dot{m}_i}{dx})$.

Returning now to the calculation of the heat release profile. With the initial total enthalpy and composition known, the total temperature can be evaluated. Until the point of fuel injection and chemical reation, the total temperature is assumed to remain unchanged and at this value in the combustor. Thus, the 3rd term in Equation 3.40 will be zero up to the point of fuel injection.

At the location of the fuel injection, a new total temperature must be evaluated. The mass flowrate of the fuel is added to the flow composition and any enthalpy contribution from the fuel is added to the flow. A new total temperature that includes the unreacted fuel and associated enthalpy contribution can then be determined.

The final total temperature can be determined since the final mass flow rates at the end of the heat release/chemical reaction have been specified apriori. The same procedure is then executed, using the final mass flowrates and total enthalpy, to determine the final total temperature value. This knowledge is actually the result of initial prior passes through the combustor to converge on the equilibrium static pressure and temperature at the end of the heat release process. After each pass, the mass flow composition derivatives are updated using the most recent temperature and pressure values. The chemical equilibrium analysis outlined in the section on 'Rocket Thruster Subsytem' can be utilized again for obtaining the reacted flow composition.

With a specified fuel injection location, starting point and ending points of heat release, a distribution based on the change in total temperature can be established. Note that the heat release in a real engine is most likely non-linear, but a linear profile can be assumed for simplicity. Heiser and Pratt provide a variety of empirical mixing and rection profile models for hydrogen fuels[9].

A fourth order Runge-Kutta (R-K) method is used to solve Equation 3.40 for the variation in Mach number[40]. This R-K routine can accommodate large stepsizes while still maintaining high levels of accuracy. All conditions at the upstream step are known beforehand. The differentials of total temperature, area, and mass flowrate are determined for the current position in the combustor. Using the Runge-Kutta solver, the local change in the Mach number is evaluated. The Mach number at the downstream point is then determined from Equation 3.43. Unless the area relief is sufficient, both the heat addition process and friction losses will drive the flow towards Mach one.

$$M_{i+1} = M_i + \frac{dM}{dx}dx \tag{3.43}$$

Note that it is not generally possible to transition the flow through the sonic point. Thus, a check on the value of the new Mach number is performed next. A comparison against a critical Mach number is done to enforce the 2nd Law of Thermodynamics. For numerical stability and as a performance margin, the critical Mach number should be either 0.95 or 1.05 depending on if subsonic or supersonic combustion is occurring. If the combustion is subsonic and the new Mach number exceeds the critical Mach number, or in the supersonic case, the Mach number is less than the critical Mach number, then the combustor analysis stops and a reduction in the fuel flowrate or equivalence ratio (ϕ) is required to prevent thermal choking. If a reduction in ϕ is not required, then the axial position, area, and total temperature are updated to the downstream position and become the upstream conditions for the next starting point.

After each successful axial step, the flow composition and molecular weights are updated at the new position. A static temperature based on the new Mach number and total temperature is then computed. With this static temperature, a new specific heat and gamma can be determined. The static pressure is then determined based on the conservation of mass equation, using the new mass flowrate.

This entire procedure is repeated until the end of the combustor is reached or the flow violates the critical Mach number condition. After the flow conditions at the exit of the combustor have been obtained, they can be used as entrance conditions to a nozzle analysis.

3.2.6 Nozzle

For subsonic combustion modes, the nozzle is a converging-diverging passage, with a throat at station '5', that expands the flow to supersonic speeds (i.e. variable geometry). For supersonic combustion, the nozzle is a divergent passage. At lower altitudes, the internal nozzle (station 4 to e) can expand the flow to atmospheric pressure (ideal expansion, $P_e=P_\infty$). At higher altitudes, the nozzle expansion is limited by the physical exit area (A_e) and the flow is often underexpanded ($P_e<P_\infty$). One option to include the effect of any external vehicle aftbody expansion is to assume a 'theoretical expansion area' ($A_{e'}$) that increases with altitude (i.e. the CIM method). Alternately, a more rigorous analysis can be performed involving a detailed fluid dynamic model and the static properties on the aftbody surface can then be obtained.

3.3 Force Accounting

Proper force accounting is critical for accurately sizing the vehicle and estimating performance. Two of the most common methods used are known as 'cowl-to-tail' accounting and 'tip-to-tail' accounting. Either method is acceptable, but care must be taken that the accounting on the remainder of the vehicle (aerodynamic forces) is consistent with that used for the propulsion system.

Computing the actual forces can involve to approaches. The first is to use a control volume (CV) approach around the entire engine. The other option is to integrate the static pressures on all exposed vehicle/engine surfaces. The control volume approach is generally used in the early stages of design since the engineer typically does not know the pressure distributions throughout the engine and vehicle. These two approaches can also be used in

conjunction on various portions of the vehicle. These methods and the necessary equations will be presented next.

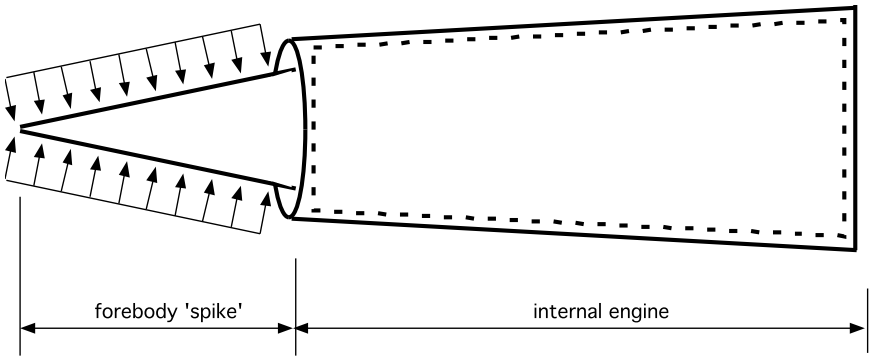

Figure 3.10 Podded Engine Static Pressure Distribution

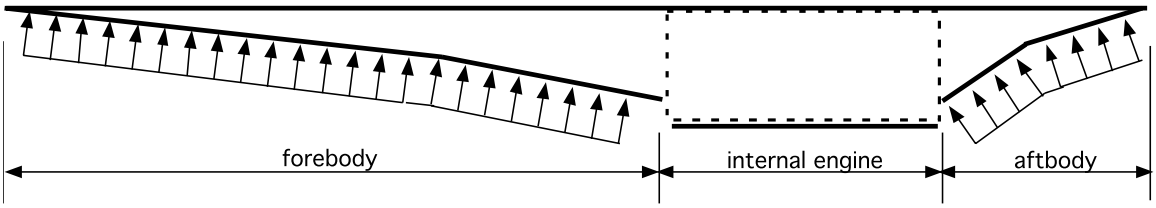

Figure 3.11 Airframe-Integrated Engine Static Pressure Distribution

3.3.1 Cowl-to-Tail Method

When using a 'cowl-to-tail' thrust accounting method, computation of the forces created by the engine begin at the cowl leading edge (station 1), and extend to the tail end of the vehicle. From the cowl leading edge to trailing edge, a control volume (CV) approach is used. This control volume accounts for the momentum change imparted on the flow internal

to the engine. The computation of the internal axial forces ($F_{x,internal}$) is shown in Equations 3.44 and 3.45.

$$F_{x,\text{int}ernal} = \dot{m}_e V_e + \left(P_e - P_\infty\right)A_e - \mathrm{M}_{cowl} \tag{3.44}$$

$$F_{y,\text{int}ernal} \cong 0 \tag{3.45}$$

Note that the internal normal force contribution from the engine is either nonexistent or will be a very small contributor to the total normal force on the vehicle. Also, it is common to always subtract out the ambient pressure (P_∞) from the local static pressure. This allows the propulsive forces to be easily added with the aerodynamic forces, which always use this convention.

The specific type of vehicle aftbody analysis being performed will dictate exactly how the resultant aftbody forces are computed. If the nozzle analysis consists of a simple isentropic expansion to a projected area (eg. $A_{e'}$), then the previous control volume around the engine can be extended to include this area, as shown in Equations 3.46 and 3.47, and the net cowl-to-tail axial force (F_x) is obtained.

$$F_{x,cowl-to-tail} = \dot{m}_{e©}V_{e©} + \left(P_{e©} - P_\infty\right)A_{e©} - \mathrm{M}_{cowl} \tag{3.46}$$

$$F_{y,cowl-to-tail} \cong 0 \tag{3.47}$$

If a more detailed nozzle analysis is performed that results in a known pressure distribution on the nozzle surface, then these pressures can be integrated to obtain the axial force ($F_{x,aftbody}$) and normal force ($F_{y,aftbody}$) contributions from the aftbody, as shown in Equation

3.40 and 3.41. Note that, as before, the freestream static pressure has been subtracted from the local static pressure.

$$F_{x,aftbody} = \sum \left(P - P_{\infty}\right) w_{nozzle} dy \tag{3.48}$$

$$F_{y,aftbody} = \sum \left(P - P_{\infty}\right) w_{nozzle} dx \tag{3.49}$$

For this scenario, the net cowl-to-tail axial and normal forces for the propulsion system can be defined as:

$$F_{x,cowl-to-tail} = F_{x,\text{int}ernal} + F_{x,aftbody} \tag{3.50}$$

$$F_{y,cowl-to-tail} = F_{y,aftbody} \tag{3.51}$$

3.3.2 Tip-to-Tail Method

If a tip-to-tail force accounting system is desired, the static pressures on the forebody must be integrated and the resultant force added to the cowl-to-tail engine thrust values. The form for this integral is provided by Equations 3.52 and 3.53.

$$F_{x,forebody} = \sum_{i=1}^{N_{ramps}} \left(P - P_{\infty}\right) w_{forebody} dy_i + F_{friction,x} \tag{3.52}$$

$$F_{y,forebody} = \sum_{i=1}^{N_{ramps}} \left(P - P_{\infty}\right) w_{forebody} dx_i \tag{3.53}$$

For this scenario, the net tip-to-tail axial and normal forces for the propulsion system can be defined as:

$$F_{x,tip-to-tail} = -F_{x,forebody} + F_{x,cowl-to-tail} \tag{3.54}$$

$$F_{y,tip-to-tail} = F_{y,foretbody} + F_{y,cowl-to-tail} \tag{3.55}$$

Thrust Coefficient

The thrust coefficient, C_t, is a common way to non-dimensionalize engine thrust to enable parametric scaling by inlet size and flight conditions. In the non-AAR airbreathing modes, C_t is defined as shown in Equation 3.56, where A_{ref} is a reference area. The most convenient A_{ref} to use is the inlet area at station '1', but some analysts use other areas for this non-dimensionalization (e.g. stream tube area at shock-on-lip conditions). Any area is acceptable, just as long as the form used is stated.

$$C_t = \frac{F_x}{q_\infty A_{ref}} \tag{3.56}$$

CHAPTER IV

AFTBODY NOZZLE ANALYSIS

4.1 Physical Description of Flowfield Attributes

The current aftbody conditions being considered are for cases when both the engine exhaust stream and freestream flows are supersonic. Figure 4.1 shows the flowfield features commonly encountered for these conditions. The three features of interest, as shown in the figure, are the outer shock, inner shock, and shear layer.

In most cases, the core engine flow will be at a higher pressure than the freestream, thus it will be underexpanded ($P_e > P_\infty$). This will cause the core flow to expand along the body very rapidly, as shown in Figure 1.2, and approach the ambient static pressure value. The freestream flow will need to be diverted around this expanding flowfield. Thus, the outer shockwave is generated as the freestream flow is diverted by the exhaust plume.

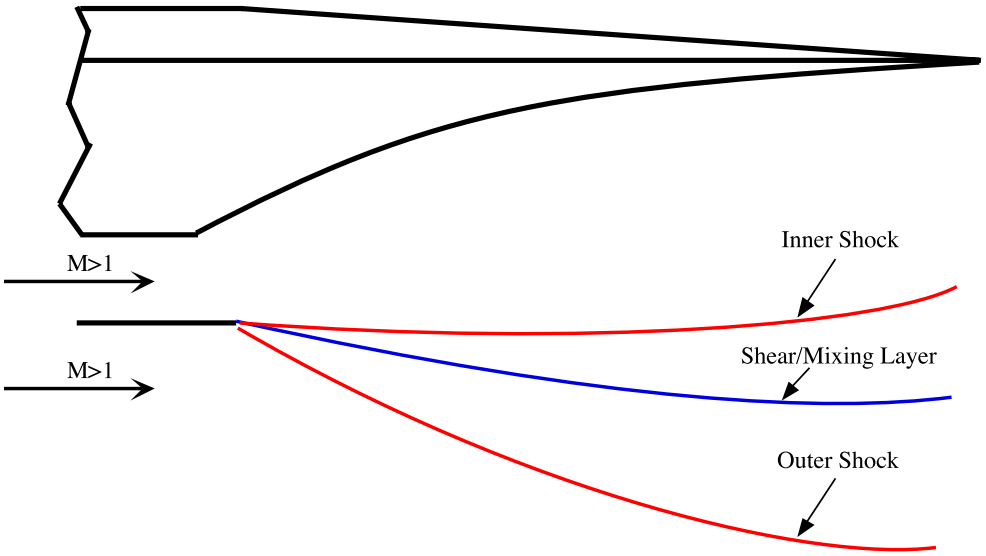

Figure 4.1 Aftbody Nozzle Flowfield Features

A shear layer will exist at the interface between the two streams. The freestream air and engine exhaust products will have a small mixing region. This mixing will be due to diffusion by mass, momentum, and energy. The mass diffusion will be a result of the species concentration gradients. While the airflow will consist almost entirely of nitrogen, oxygen, and argon species, the engine exhaust products will contain numerous different molecules (eg. H_2O, CO_2, OH). The velocity gradients due to the difference in the freestream and core flows will also promote mixing. Finally, the high temperature exhaust products of the core flow and low, ambient temperature of the freestream flow will cause thermal transport processes.

Typically, the nozzle will have its highest expansion angle immediately upon leaving the engine. The nozzle surface will then turn inward, thus decreasing the expansion angle. The

optimal expansion angle(s) can easily be determined for operation at a single flight condition. For operation over a wide range of flight conditions, determination of the optimal angles becomes more difficult. If the nozzle is designed with an expansion angle that is too high, the flow will tend to be overexpanded at low Mach number flight conditions. This overexpansion can require 'base burning', a process where fuel is injected and burned near the nozzle surface in an attempt to increase static pressures and reduce the overall vehicle drag. High expansion angles can also reduce the normal force and moment generated by the nozzle. This moment is the critical for countering the moment generated by the vehicle forebody pressures and maintaining vehicle stability. If the nozzle expansion angle is to low, the flow can be greatly underexpanded at high Mach number and altitude flight conditions, reducing the thrust from the engine.

4.2 Analytic Model

A schematic of a typical aftbody nozzle design, with notations for the two flow streams and parameters that are necessary to accurately model the flow is shown in Figure 4.2. After non-dimensionalizing a few of the variables, a total of nine are required to specify a unique operating condition. This will allow for the broadest applicability of the results. These design variables name and nomenclature are presented in Table 4.1.

By specifying a freestream altitude, the freestream density (ρ_∞) and pressure (P_∞) can be obtained. A freestream specific heat ratio (γ_∞) and molecular weight ($\mathcal{MW}_\infty$) values of 1.4016 and 28.965 respectively, corresponding to air, are always used.

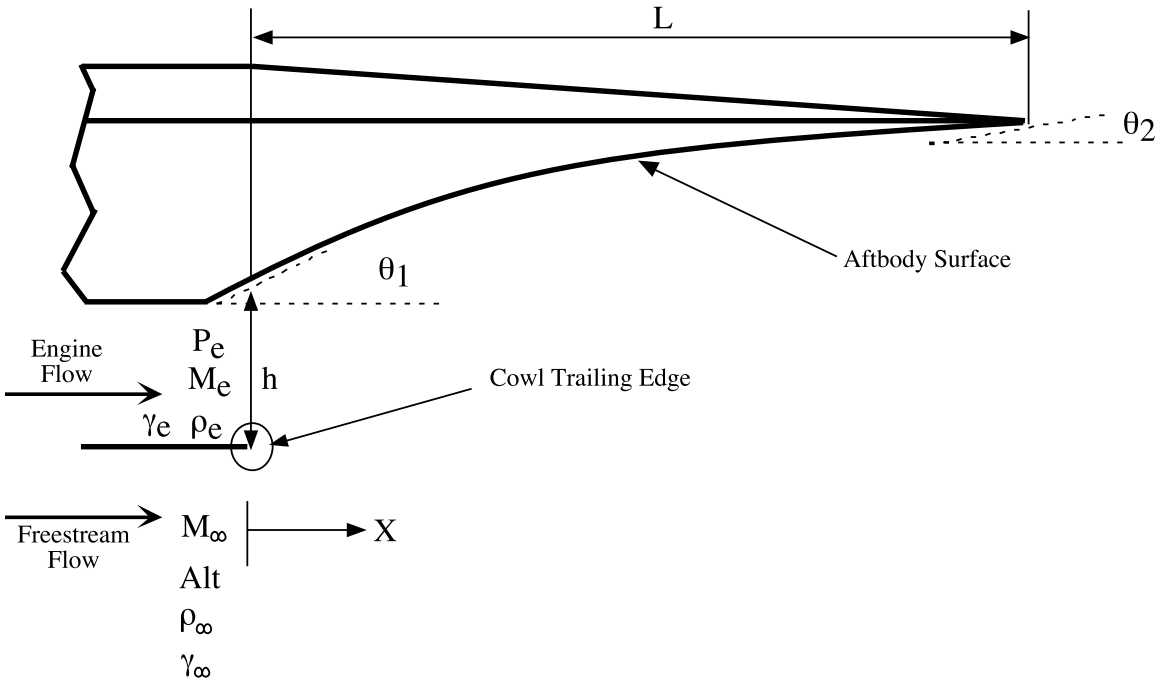

Figure 4.2 Aftbody Nozzle Model

Table 4.1. Aftbody Nozzle Design Variables

Name	Symbol
Engine Exit Mach Number	M_e
Engine Exit Specific Heat Ratio	γ_e
Engine Exit-to-Freestream Static Pressure Ratio	P_e/P_∞
Freestream-to-Engine Exit Density Ratio	ρ_∞/ρ_e
Freestream Mach Number	M_∞
Flight Altitude (Kft)	Alt
Engine Exit Height to Nozzle Length Ratio	h/L
Initial Nozzle Ramp Expansion Angle	θ_1
Final Nozzle Ramp Expansion Angle	θ_2

4.3 Flowfield Solver

4.3.1 Grid Generation

The first step in the analysis of a single point is establishing the nozzle shape and discretizing the flowfield. The shape for the nozzle surface is dictated by the initial and final expansion angles. Linear changes in surface angle at 20 discrete points allows for a smooth flow expansion. The equation for the nozzle expansion angle at a given axial position is provided in Equation 4.1.

$$\theta = \theta_{initial} + \left(\frac{x}{L}\right)\left(\theta_{final} - \theta_{initial}\right) \tag{4.1}$$

For the jet-boundary side of the grid, an initial guess with a y/L value of 1.0 is allowed for the expanding flowfield. Typical runs utilize 150 grid points in the axial direction and 150 in the normal direction. With this information, the grid generation program is executed. This program is a simple algebraic grid generator that incorporates stretching functions in both the normal and axial directions. Equations 4.2 and 4.3 show the stretching functions used, where C_x is for the axial clustering and C_y is for the normal direction clustering. Note ξ_{max} is the total number of points in the axial direction and η_{max} is the total number of points in the normal direction.

This clustering allows the grid points to be focused near the cowl trailing edge and nozzle surface. Note that in the axial direction, the stretching function was applied at the upper and lower bounds only, then a linear interpolation routine was applied between the boundaries for determining the x-coordinate locations.

$$x_{i,j} = x_{i,1} - \frac{\left(x_{\xi_{\max},1} - x_{1,j}\right)}{C_x}\left(\log\left(1 + \left(\frac{\left(e^{-C_x} - 1\right)(i-1)}{\xi_{\max} - 1}\right)\right)\right) \tag{4.2}$$

$$y_{i,j} = y_{i,1} - \frac{\left(y_{i,\eta_{\max}} - y_{i,1}\right)}{C_y}\left(\log\left(1 + \left(\frac{\left(e^{-Cy} - 1\right)(i-1)}{\eta_{\max} - 1}\right)\right)\right) \tag{4.3}$$

Execution of the grid generator is on the order of a few seconds, depending upon the desired grid resolution. Figure 4.3 shows the results for a nozzle design case with a 25° initial ramp angle and final divergence angle of 2°. For this case, the stretching factors were 1.5 axially (C_x) and 1.5 normally (C_y).

Care must be taken in the grid generation process to ensure that the expanding nozzle exhaust does not reach the lower boundary of the grid. If this occurs, the flowfield cannot be resolved accurately and the grid dimensions in the normal direction are manually increased to provide sufficient area for the flow to develop. For flows with large plume expansion area, additional grid points are added to maintain sufficient resolution. Similarly, for cases where the plume has very little expansion, the grid dimensions could be decreased, but the number of grid points are left at their initial value for these cases.

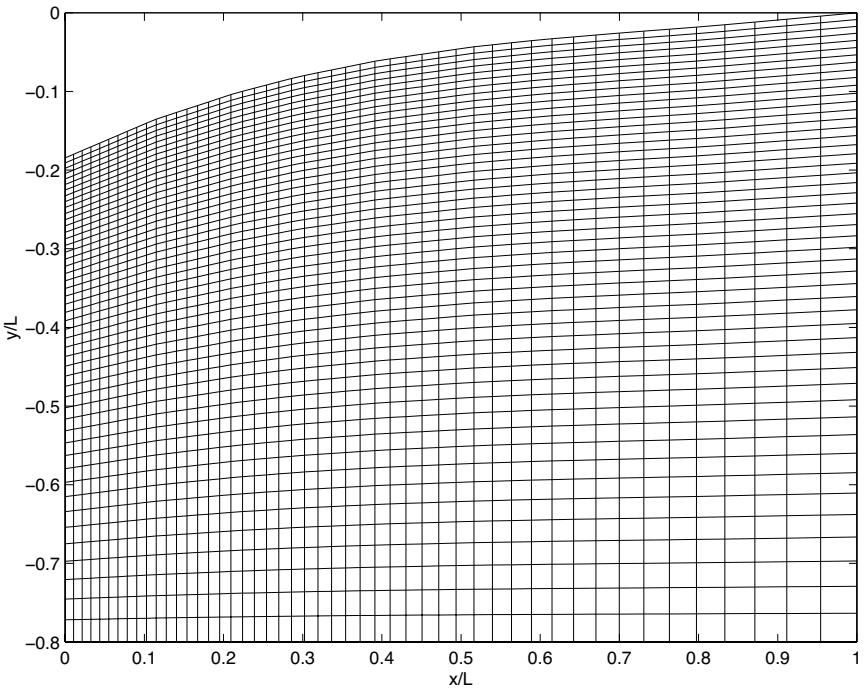

Figure 4.3 Sample Aftbody Nozzle Grid

4.3.2 Flowfield Solver

The nozzle flowfield solver uses a perfect gas model for the Euler equations in a two-dimensional flow field. This code uses a shock-capturing, implicit routine with Roe Averaging [49]. After some experimentation, it was found that a first-order accurate, fully upwind scheme provided the most robustness and fastest convergence rates. The overall robustness is critical for minimizing the amount of user interaction, especially when performing multiple runs.

Instead of using an 'effective gamma' method, the different γ's for the two flows (engine exhaust and freestream) are handled as discrete values. To determine which grid node uses

which specific heat ratio value, the continuity equation is used. The core's mass flowrate is determined at the upstream, inflow boundary plane. This value is then used at each vertical plane to determine the location of the interface between the two flowfields. Starting at the nozzle surface, the mass flux is integrated along a constant vertical grid line. When the integrated value exceeds the mass flowrate at the upstream boundary, the location is stored as the interface location. Between the body and this point, the engine exhaust specific heat (γ_e) is used. Below this point and to the lower grid boundary, the freestream specific heat value (γ_∞) is used. These values are updated after each iteration of the solution scheme. Figure 4.4 provides a sample contour plot resulting from implementing this method.

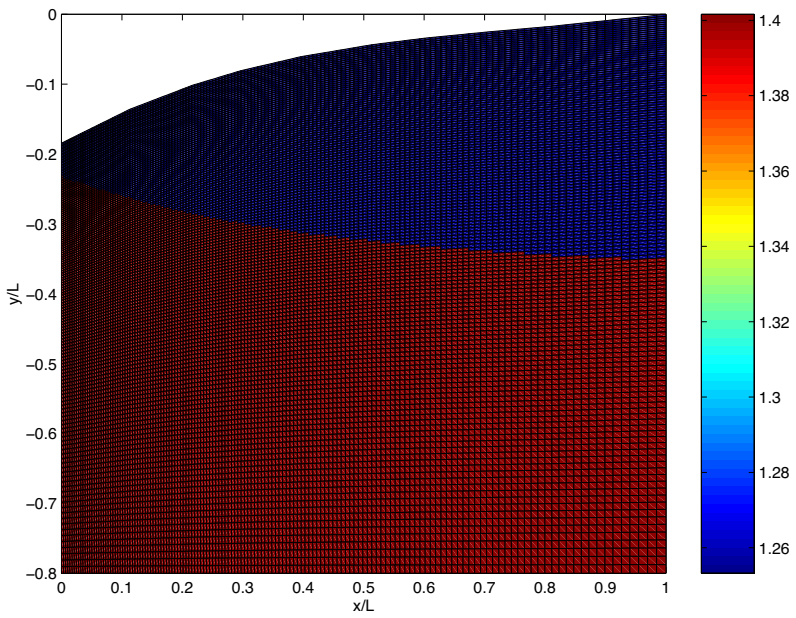

Figure 4.4 Sample Specific Heat Ratio Contour Plot

The engine exit flow velocity (at the upstream boundary) is varied linearly between $\theta=\theta_1$ on the vehicle body side and $\theta=0^o$ on the cowl side. This is a common assumption made for transforming the 1-D combustor exit results into a 2-D flowfield for the nozzle [50].

4.4 Pressure Distribution Fitting Models

Using only a few select points from the actual distribution, it is possible to recreate an approximation of the complete aftbody surface pressure-ratio distribution. This recreation needs to be as close as possible to the actual distribution since it will be integrated to obtain the net forces. Any errors in the fit result in errors in the force predictions.

The pressure data from the nozzle can be 'curve-fit' using a variety of regression methods. After carefully considering a variety of models, it has been concluded that a 5^{th} order polynomial provided the best fit for the widest range of nozzle designs. Lower order fits were unable to provide needed inflection points and steep initial gradients found in many distributions.

Critical for obtaining an accurate representation of the flow is ensuring that the model intercept is unity. This corresponds to the pressure ratio (P/P_e) at the engine exit plane, which will always be unity. A simple least squares analysis on the actual pressure ratios will result in the fit missing this intercept, sometimes significantly. This can be corrected by using a weighted least-squares analysis, or Chi-Square fit [51]. This method assigns weighting factors (σ_i) on the data to be fit. By assigning higher weighting factors to points that are closer to the engine exit plane, the intercept requirement can be meet. The general form for the equation being solved by the Chi-Square routine is provided by Equation 4.4,

where the values for a_i's are the 5th order polynomial coefficients. It should be noted that better results were obtained by fitting the inverse of the specified data points. Therefore, the 5th order polynomial provides the inverse pressures and must be inverted, as shown in Equation 4.5. The χ-minimization can be accomplished using a singular-value decomposition (SVD) matrix routine[47].

$$\min \chi^2 \equiv \sum_{i=1}^{N} \left(\frac{\left(\frac{P_e}{P}\right)_i - \left(\frac{P_e}{P}\right)(x_i, a_0 \ldots a_5)}{\sigma_i} \right)^2 \tag{4.4}$$

$$\frac{\mathrm{P}}{\mathrm{P_e}} = \frac{1}{a_0 + a_1\left(\frac{x}{L}\right) + a_2\left(\frac{x}{L}\right)^2 + a_3\left(\frac{x}{L}\right)^3 + a_4\left(\frac{x}{L}\right)^4 + a_5\left(\frac{x}{L}\right)^5} \tag{4.5}$$

A χ-Square fitting routine for regeneration of the pressure distributions was implemented using a published algorithm[51]. The code is written in the 'C' programming language and execution time is nearly instantaneous. The necessary input parameters are the number of data points to be fit (*N*), the desired polynomial order (eg. 5), and the weighting factors assigned to each data point (σ_i's). The following weighting factor distribution performs well in achieving the desired fit attributes:

$$\sigma_i = \left(1 + \frac{(i-1)(1000-1)}{N-1}\right) \tag{4.6}$$

Figure 4.6 provides an actual aftbody pressure distribution and the results for two sample fitting models. One fit used the standard least-squares approach and the other using the χ-Square fit method. Notice the superior results from the χ-Square method. This fitting technique has been tested for a range of distributions, with similar results always being obtained.

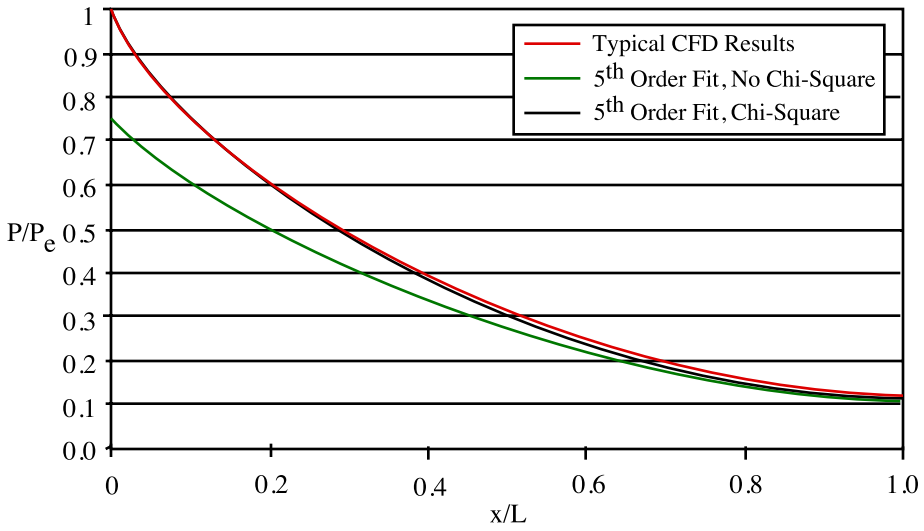

Figure 4.5 Pressure Distribution Fitting Results

4.5 Spatial Convergence Test

The required grid resolution necessary to accurately resolve the flowfield was determined through a spatial convergence test. While the number of grid nodes could be set at randomly selected high levels, this would be a valuable waste of computing resources. Thus, an attempt was made to determine the minimum resolution necessary for accurate result generation.

The tests were conducted for a generic, M_∞=9 SERN design with a y/L value of 1.0. The flow conditions used are specified in Table 4.2.

Table 4.2 Spatial Convergence Test Variable Settings

Parameter	Setting
M_e	1.85
γ_e	1.3
P_e/P_∞	20.0
ρ_∞/ρ_e	1.0
M_∞	9.0
Alt (Kft)	85
h/L	0.1
θ_1 (°)	17.5
θ_2 (°)	17.5

By systematically increasing the grid resolution and analyzing the change in the steady-state solution, the convergence rate can be examined. The integrated forces were used as the convergence metrics.

A total of six different resolutions were examined for the test. Table 4.3 provides the grid sizes and execution times for each case. Execution times were based on results from a 350 Mhz R12000 Unix workstation. Figure 4.6 shows the integrated axial force values for each case examined. Using the 200-by-200 node grid results as the 'real' solution, the 150-by-150 node grid achieved an integrated force value within 0.6% of this case. From these results, the 150-by-150 node grid was selected as the minimum resolution necessary for spatial convergence.

Table 4.3 Spatial Convergence Test Cases

Nodes in Axial Direction	Nodes in Normal Direction	Total Grid Nodes	Execution Time (min:sec)
50	50	2,500	3:21
75	75	5,625	8:56
100	100	10,000	18:23
125	125	15,625	31:03
150	150	22,500	45:17
200	200	40,000	107:37

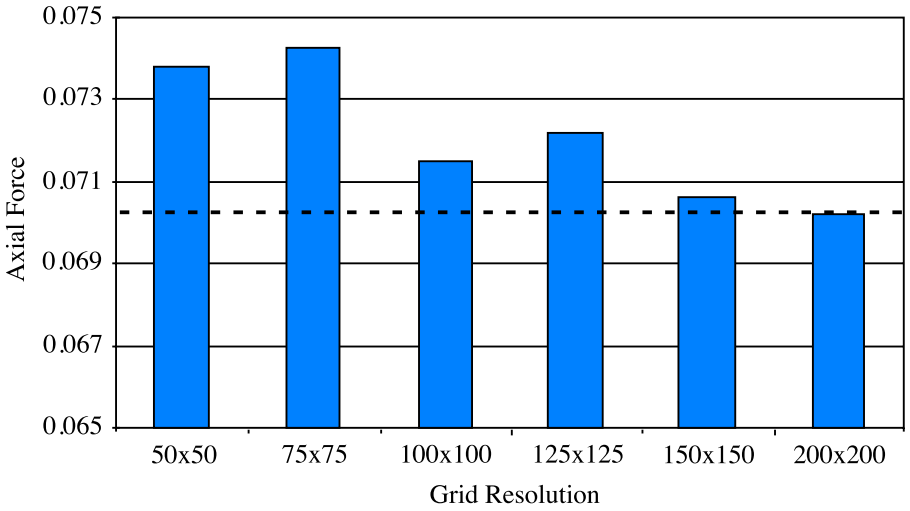

Figure 4.6 Net Axial Force versus Grid Resolution

4.6 Model Verification

Before proceeding with the RSM, a test case was conducted to verify the accuracy of the flow solver created. A well-established program from NASA called SEAGULL was used to benchmark the code to be used for the RSE generation. SEAGULL is an implicit, perfect gas 2-D Euler flow solver[34]. The code uses a shock-fitting method, as opposed to the shock-capturing method, so it executes fairly quickly. This code was written in Fortran by the NASA Langley Research Center in the 1970's. The main drawback of SEAGULL is that it is not written in an object-oriented language and it is not easy to modify, script, or integrate with other codes.

The test case examined was for a Mach 7 freestream scramjet engine. The nozzle ramp geometry begins with an expansion of 21° and smoothly decreases to about 2° to minimize the divergence losses. The engine exit conditions and freestream parameters are presented in Table 4.4.

Table 4.4 Verification Case Variable Settings

Parameter	Setting
M_e	1.368
γ_e	1.25
P_e/P_∞	45.8
ρ_∞/ρ_e	0.314
M_∞	7.0
Alt (Kft)	80
h/L	0.05
θ_1 (°)	21
θ_2 (°)	2

Figure 4.7 compares the new CFD flow solver results with those produced from SEAGULL. Plotted in the figure is the normalized pressure distribution versus axial distance. Excellent agreement can be seen between the two pressure ratios distributions. Figure 4.8 provides the resultant flowfield Mach number contours and Figure 4.9 provides the pressure contours from the new solver. Evident in the contour maps is the expected outer and inner shockwaves and the shear layer, both originating from the cowl trailing edge and extending downstream.

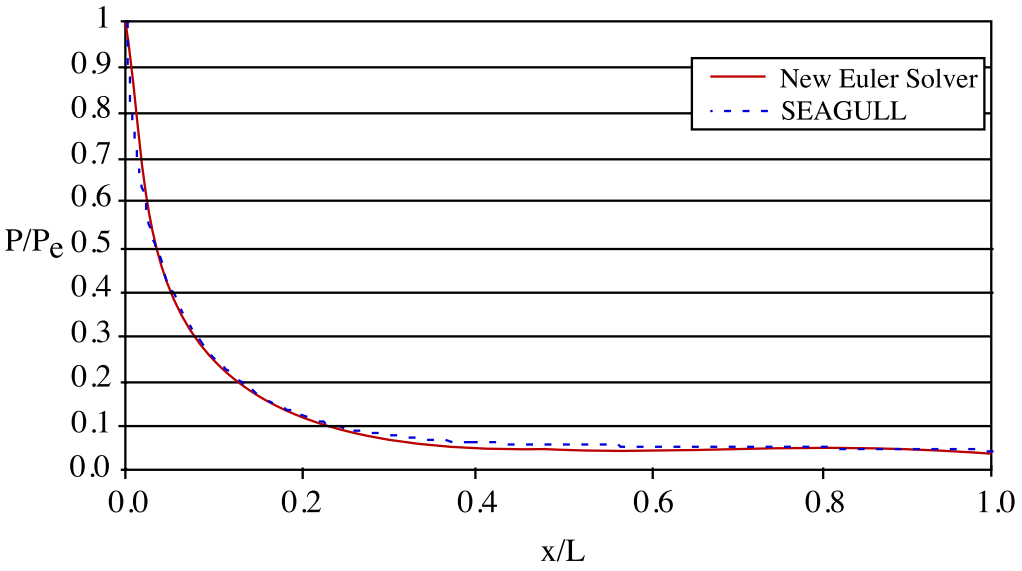

Figure 4.7 Nozzle Surface Static Pressure Comparisons with SEAGULL

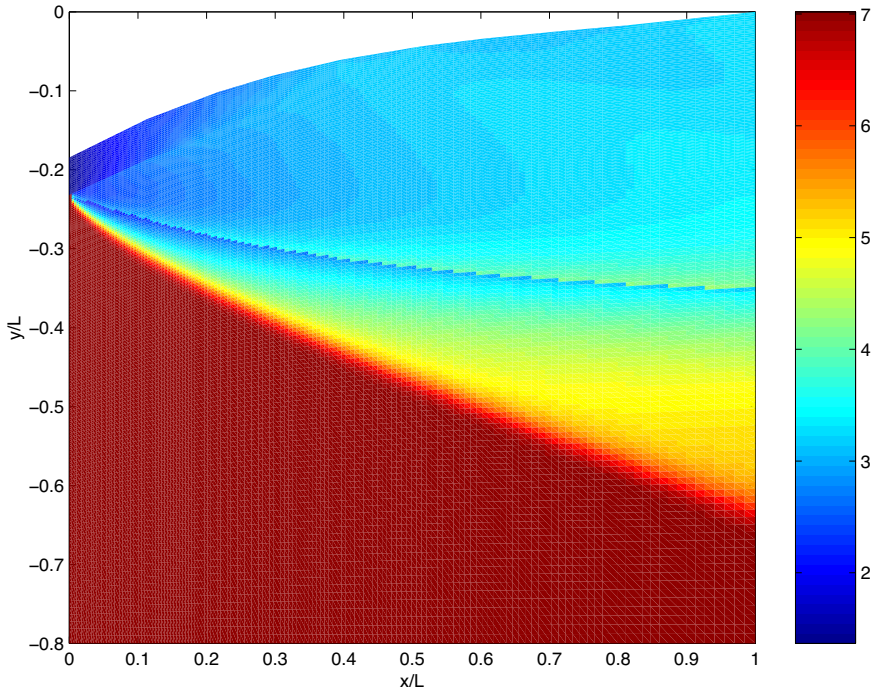

Figure 4.8 Mach Number Contours for Flow Solver Verification Test

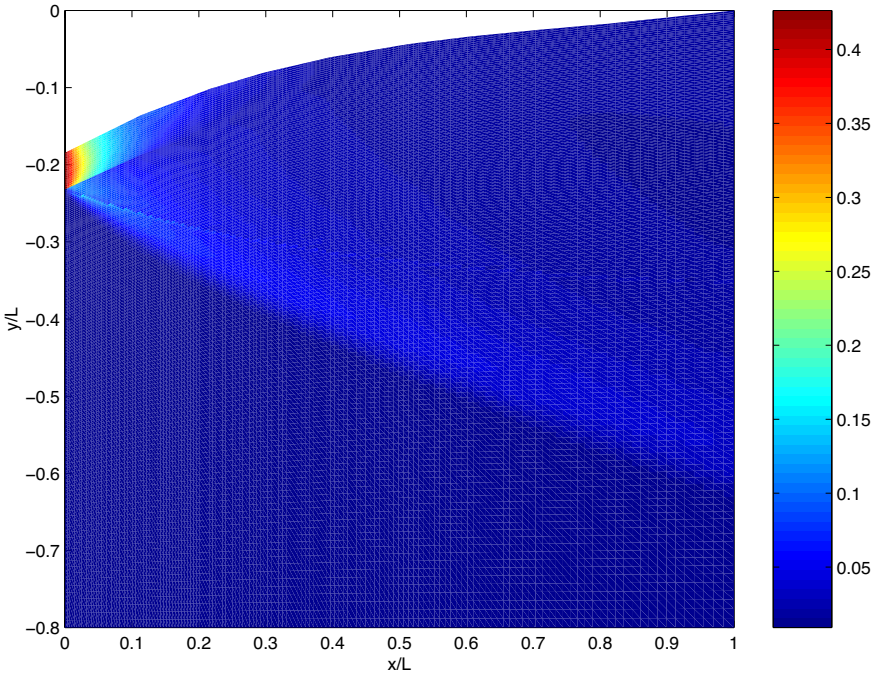

Figure 4.9 Static Pressure Contours for Flow Solver Verification Test

Presented in Table 4.5 are the actual values obtained for the axial and normal force integrated pressure ratio distributions. Additionally, results from the HUD boundary layer code that is integrated into SEAGULL have been included for the axial force values. Notice that the effect of the skin friction is to decrease the inviscid axial force by approximately 2%. Additional cases at Mach 3.5 and Mach 10 indicated that the skin friction effect decreases with increasing flight Mach number. For the Mach 3.5 case, the decrease in axial force was 5%. For the Mach 10 case, this effect had been reduced to less than a 1% reduction in the inviscid axial force.

Table 4.5 Flow Solver Verification Test Results

	SEAGULL No Friction	SEAGULL With friction	New Euler Solver No Friction
Axial Force	0.03283	0.03217	0.03225
Normal Force	0.10649	0.10649	0.10649

CHAPTER V

RESPONSE SURFACE METHODOLOGY

5.1 Overview

The procedure for performing a Response Surface Methodology (RSM) requires four steps[8,52]. The first step is the selection of the system response(s) and identification of all the input parameters that effect this response. These parameters must each be assigned a lower and upper bound appropriate for the design space being investigated. The second step involves performing a 'screening test'. This screening test involves examining the response's sensitivity to the main effects only (i.e. a single parameter). This linear model is generated by performing a two-level Design of Experiments (DOE) analysis. The purpose of the screening test is to identify the factors that have the most significant effect on the responses. Inherent to this test is the assumption that the main effects will contribute more to the variance of the response than any higher order interactions. With this information, it might be possible to reduce the number of input parameters. Once the most significant contributors have been identified, they become the input parameters to the RSE's. Any parameters that are determined to have a negligible or small effect on the response will be eliminated as a RSE variable and be set to their nominal value. As the third step, the three-level RSE generation can now take place. For generation of the RSE experiment design,

many options exist (eg. Box Behnken, CCD, Full-Factorial)[53]. Each of these options have their benefits and consequences. For a given design type, the number of input parameters will determine the number of cases that must be analyzed to map out the design space and generate the meta-model. For large number of variables (6+), there can be a significant difference in the number of cases required for different experiment designs, as shown in Table 5.1.

Table 5.1 Sampling of Experiment Designs for 7 Variables

Experiment Design	Number of Experiments
Box-Behnken	57
Central-Composite (Fractional Factoral)	79
Central-Composite (Fractional Factoral)	143
Full-Factorial	2,187

For designing the necessary experiments, compiling the data, and interpreting the results, a software package developed by the SAS Institute known as JMP (pronounced 'jump') will be used[54].

5.2 Screening Test

Table 5.2 shows the nine nozzle design variables (see Figure 4.1) and their ranges used for the screening test runs. In order to maintain reasonable variable range and setting combinations, two separate screening tests were constructed. One of these sets used variable ranges appropriate during supersonic flight conditions, while the other set used variable

ranges appropriate for hypersonic flight conditions. Note that the ranges for all geometric parameters are identical.

Table 5.2 Screening Test Variable Ranges

Variable	Supersonic Set	Hypersonic Set
M_e	1.2-3	1.2-4
γ_e	1.2-1.4	1.2-1.4
P_e/P_∞	10-100	5-100
ρ_∞/ρ_e	0.1-5	0.1-3
M_∞	2.5-6	6-12
Alt (Kft)	40-90	70-120
h/L	0.05-0.15	0.05-0.15
θ_1 (°)	10-25	10-25
θ_2 (°)	0-10	0-10

For the tests, three responses were examined and used as the overall metrics for evaluating if any potential variables are to be screened out. The three responses are the axial force, normal force, and the moment arm (S) for the nozzle, provided by Equations 5.1, 5.2, and 5.3. At the vehicle level, these responses are all in a body-frame coordinate system. Note that in the moment arm calculation, the parameter Θ is a theoretical expansion angle between the start and end points on the nozzle surface. This provides a convenient and easy way to compute and visualize the moment arm.

$$Axial\ Force = \int_0^h (\mathrm{P}dy) \tag{5.1}$$

$$Normal\ Force = \int_0^1 (\mathrm{Pdx}) \tag{5.2}$$

$$S = \frac{TotalMoment}{AxialForce \cdot \sin(\Theta) + NormalForce \cdot \cos(\Theta)} \tag{5.3}$$

Using the JMP software, a two-level Plackett-Burman (P-B) DOE was created for each screening variable set. The P-B designs required twelve runs each for analyzing the main effects. Appendix B contains the P-B experiment designs and computed responses from the Euler flow analysis for both the supersonic and hypersonic sets.

Supersonic Set Results

Pareto plots showing the individual contribution of each input parameter to the variance of the response were generated using JMP and are presented in Figures 5.1-5.3. Contributing up to 25% of the variance for the axial force and 32% for the normal force, the strong impact of the h/L parameter on all three responses is evident in the variance distributions. The initial expansion angle (θ_1) and the core Mach number (M_e) are also dominant effects for the axial and normal forces. Of interest is the pressure ratio which appears to have only minor influence on either nozzle forces.

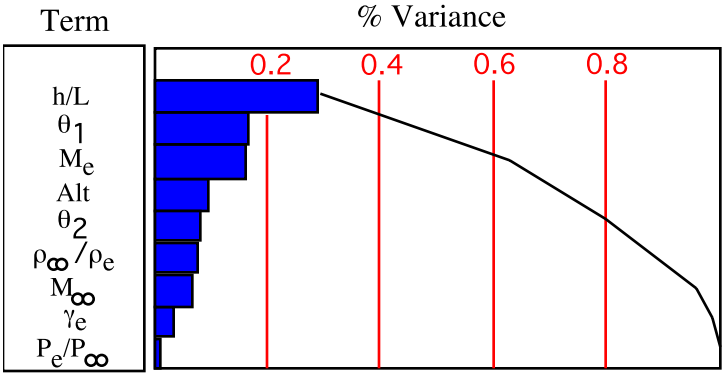

Figure 5.1 Axial Force Pareto Chart (Supersonic Case)

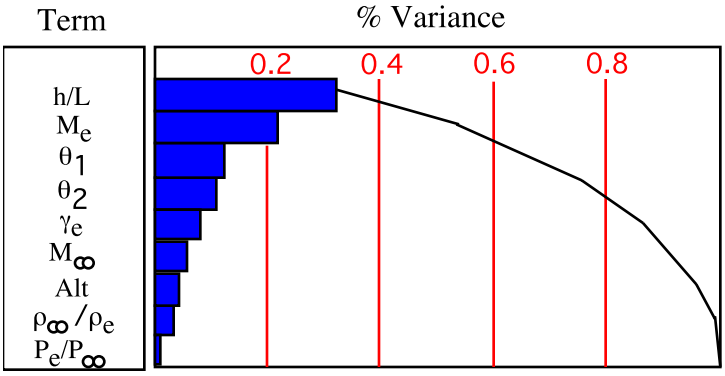

Figure 5.2 Normal Force Pareto Chart (Supersonic Case)

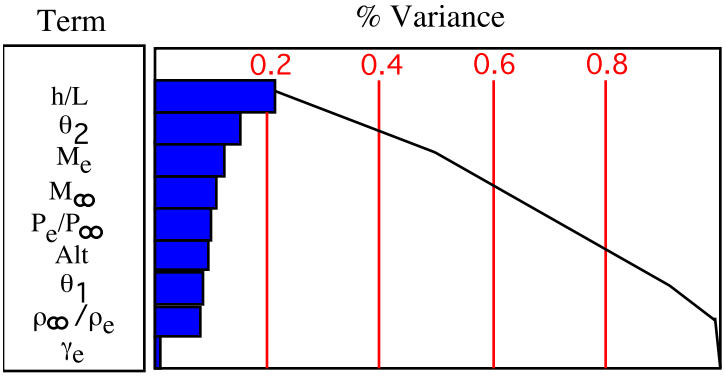

Figure 5.3 Moment Arm Pareto Chart (Supersonic Case)

For a screening analysis it is desireable to retain at least 80% of the responses's variance. Generally, a few variables will comprise a majority of the variance. For the supersonic cases, it was possible to eliminate two factors, P_e/P_∞ and γ_e, from the RSE list of input parameters while still maintaining 90% of the response variance. Even though the engine specific heat ratio effect made up about 7% of the normal force variance, the alternative was to eliminate the freestream Mach number parameter. But, this would have resulted in losing this effect for the axial force variance. Since accuracy in the nozzle's axial force is more desirable than for the normal force, the engine specific heat ratio was selected as the variable to be screened out. These two parameters were set to nominal values of 40.0 and 1.3 for P_e/P_∞ and γ_e respectively.

Hypersonic Set Results

Pareto plots were generated again using JMP for the hypersonic set and are presented in Figures 5.4-5.6. As expected, the exit Mah number and geometric parameters were the top variance contributors for all three hypersonic responses. The initial expansion angle and the core Mach number are still dominant effects for the axial force. Note that while the axial force factors are almost identical in significance to the supersonic set results, the normal force and moment arm results are not.

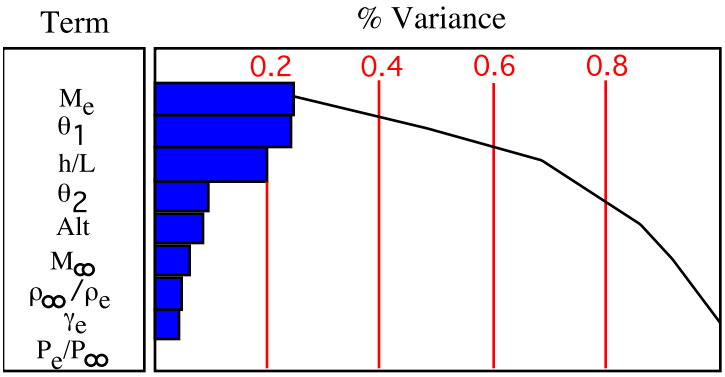

Figure 5.4 Axial Force Pareto Chart (Hypersonic Case)

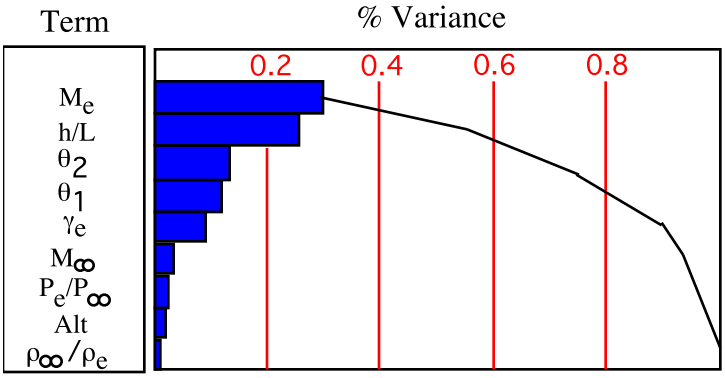

Figure 5.5 Normal Force Pareto Chart (Hypersonic Case)

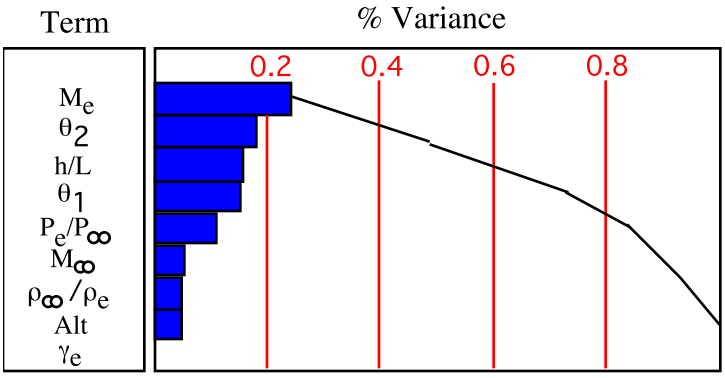

Figure 5.6 Moment Arm Pareto Chart (Hypersonic Case)

The results of the hypersonic runs were more difficult to interpret and select the screening variables. From the axial force chart (Figure 5.4), the three lowest parameters in order of significance are the density ratio, engine specific heat ratio, and pressure ratio. Note that the engine specific heat ratio and density ratio have about the same contribution levels. In Figure 5.5, the bottom three parameters for the normal force are the pressure ratio, density ratio, and altitude. Note that the density and pressure ratios have swapped their order of signicance. Ideally, the bottom two parameters for the normal force would have been the pressure ratio and the engine specific heat ratio. A quick look at the moment arm result shows that the engine specific heat ratio appears to have no effect on that response, but the pressure ratio has a fairly significant effect on the moment arm. For this reason, the pressure ratio (P_e/P_∞) and density ratio (ρ_∞/ρ_e) were selected to be screened. The altitude was kept due to its significance on the axial force and moment arm. The specific heat ratio was kept due to the normal force. All three responses still retain over 80% of the response variance with these two parameters screened out. These parameters will be set to the nominal values of 52.5 and 1.05 for P_e/P_∞ and ρ_∞/ρ_e respectively.

5.3 Central-Composite Design

With the results of the screening test, the input parameter sets were reduced to seven variables each. A three-level fractional factoral Central Composite Design (CCD) experiment was created for both supersonic and hypersonic sets. Data obtained from this experiment design will be used to construct the RSE's. For the seven design parameters, 143 Euler runs were required to fill out the CCD's (see Appendix C). Referring to Table 5.1, this experiment design was selected over the Box-Behnken (BB) design because many

of the responses at corner points in the design space need to be represented (eg. low M_∞ and low Alt, high M_∞ and high Alt). The BB design specifically avoids these variable setting combinations, which is useful for some problems, but would have resulted in missed effects. The full-factorial design was not selected for the obvious reason of too many required experiments. Finally, the other fractional factorial CCD was not selected based on initial testing. While it requires only about 60% of the runs necessary in the maximum resolution design, this design missed many of the necessary interactions and did not provide sufficient predictions of the responses.

The three responses from the screening test have now been replaced with five different responses. These new responses are the pressure ratio (local-to-engine exit static pressure, P/P_e), acting on the nozzle surface at a given axial location. The five selected locations are at axial positions, $x/L)_i$'s, of 0.1, 0.2, 0.6, 0.9, and 1.0. The pressure ratio at $x/L)_{0.0}$ is known since its value will always be 1.0.

These responses make up the data points necessary for reconstructing the complete pressure distribution of the nozzle. Using the Chi-Square regression analysis (see section 4.4) that fits a 5^{th} order polynomial curve, a continous and smooth distribution can be obtained. The Chi-Square analysis results in the generation of six polynomial coefficients (a_i's), of which a_0 will always be 1.0. The form of this polynomial and the equation for computing the pressure ratio at any axial station is shown in Equation 4.5.

CHAPTER VI

RESPONSE SURFACE EQUATIONS

6.1 Full-RSE Model Generation

All cases from the CCD DOE were analyzed using the CFD solver that was created. Approximately 250 hours of CPU time was required on a 350 Mhz R12000-class Unix workstations with a minimum of 480 MB of RAM. The values for the responses obtained for all 286 runs are included in Appendix D.

The JMP software was then used to compute the RSE's for each response (see Equation 1.1). With seven variables, the 2nd order meta-model requires 36 coefficients. Although this seems like it requires a significant number of computations to obtain the pressure distribution, it is still insignificant compared to the hundreds of millions of operations required for direct generation using the CFD results. Appendix E contains the five RSE's and the values for the coefficients in each for both supersonic and hypersonic sets.

The accuracy of the RSE predictions compared to the actual, provided response can be measured in terms of the R^2 value. The measure of the fit is computed as:

$$R^2 = 1 - \frac{SSE}{SSM} \tag{6.1}$$

where *SSE* is the sum of squares for the error and *SSM* is the total sum of the squares of the mean. Another metric is the adjusted-R^2 value, in which the R^2 value from Equation 6.1 is 'adjusted' by the number of variables (k) and experiments (n) in the RSE equation. This metric, shown in Equation 6.2, allows for comparing meta-models with a different number of coefficients.

$$\text{Adjusted } R^2 = \left(1 - \left(1 - R^2\right)\left(\frac{n-1}{n-k-1}\right)\right) \tag{6.2}$$

Supersonic Set RSE's

Table 6.1 shows the R^2 and adjusted-R^2 values for each of the five supersonic-set responses. Most parameters had R^2 values in excess of 0.985, indicating a fairly good fit. It would appear that the more difficult responses to fit are those for the pressure ratio locations at 0.1 and 1.0. The adjusted-R^2 values display a similar trend, as expected. The adjusted values will be used for comparison in a later test.

Table 6.1 R^2 and Adjusted-R^2 Values for Full-RSE Supersonic Sets

Response	R^2 Value	Adjusted-R^2 Value
$x/L)_{0.1}$	0.9842	0.9799
$x/L)_{0.2}$	0.9973	0.9965
$x/L)_{0.6}$	0.9912	0.9883
$x/L)_{0.9}$	0.9878	0.9838
$x/L)_{1.0}$	0.9852	0.9804

Hypersonic Set RSE's

Table 6.2 shows the R^2 and adjusted-R^2 values for each of the five hypersonic-set responses. Note that the R^2 values for these responses do not appear to be as good as those for the supersonic set. The responses with the poorest fit are those further downstream, at axial locations of 0.9, and 1.0. An examination of the prediction results showed that the lack of response fit were consistently occurring at parameter settings with high pressure ratios (i.e. 100) and low engine exit Mach numbers (i.e. 1.2). These particular settings will almost never occur for a real engine design. The high pressure ratios typically occur at high altitude flight conditions where the ambient pressure is very low, and the low exit Mach numbers typically occur at lower flight speeds and altitudes. Unfortunately, the responses at these points impact the fit at other settings.

Table 6.2 R^2 and Adjusted-R^2 Values for Full-RSE Hypersonic Set

Response	R^2 Value	R^2-Adjusted Value
$x/L)_{0.1}$	0.9795	0.9727
$x/L)_{0.2}$	0.9899	0.9866
$x/L)_{0.6}$	0.9852	0.9804
$x/L)_{0.9}$	0.9792	0.9724
$x/L)_{1.0}$	0.9733	0.9645

6.2 Stepwise Regression RSE Results

In an effort to reduce the number of coefficients composing the response, a stepwise regression analysis was performed. This technique consists of systematically entering and removing (i.e. setting to zero) terms in the full-RSE and computing the new R^2 and adjusted-R^2 values. By examining the F-ratio statistic, the likelihood of the term actually being non-zero due to random error or noise in the model can be determined. This technique is also commonly referred to as 'reduced order RSE methods' [55].

The stepwise process can proceed in a number of ways. The most common are the 'forward' and 'backward' progressing steps. For the forward stepping, all terms in the RSE are initially removed from the model. At each step, one term is added and the new adjusted-R^2 value computed. For the backward stepping, all terms in the RSE are initially included in the model and for each step, a term is progressively removed from the model.

Both the forward and backward methods were applied on each response for both the supersonic and hypersonic sets. Tables 6.3 and 6.4 show the best value obtained for the R^2 and adjusted-R^2 values from either method. Note that in most cases, the number of coefficients making up the RSE model was reduced from the original 36 to approximately 19. In all cases, the forward step regression method yielded the best results.

Table 6.3 Supersonic Set Stepwise-Regression Results

Response	R^2	Adjusted-R^2 Value	Number Terms
$x/L)_{0.1}$	0.9838	0.9823	13
$x/L)_{0.2}$	0.9972	0.9968	21
$x/L)_{0.6}$	0.9909	0.9898	17
$x/L)_{0.9}$	0.9875	0.9857	19
$x/L)_{1.0}$	0.9849	0.9826	20

Table 6.4 Hypersonic Set Stepwise Regression Results

Response	R^2	Adjusted-R^2 Value	Number Terms
$x/L)_{0.1}$	0.9788	0.9765	15
$x/L)_{0.2}$	0.9896	0.9880	20
$x/L)_{0.6}$	0.9845	0.9832	12
$x/L)_{0.9}$	0.9786	0.9759	17
$x/L)_{1.0}$	0.9726	0.9691	17

Of interest is the fact that the stepwise regression analysis was able to reduce the number of terms by up to 23 coefficients in some cases. Not surprisingly though is that each response model became unique and eliminated different parameters from the full-RSE model. Additionally, all R^2 values were reduced by only a small amount from their values in Tables 6.1 and 6.2, but the adjusted-R^2 value was increased noticeably for some of the responses. It is felt that although a significant number of terms could be eliminated from each RSE, this reduction is still not substantial enough to warrant the increased complexity involved in tracking a total of ten separate reduced-order RSE models.

6.3 Confidence Test Cases for Variable Settings In-Bounds

With the successful execution of the CFD solver and generation of the RSE's, both the supersonic and hypersonic sets predictions were compared with actual CFD results for two test cases (i.e. total of four). The variable settings for these cases are all at values whose ranges were within the bounds of the RSE-model generation. These confidence tests will be the true measure of the RSE's ability to predict the nozzle performance.

Supersonic Tests

The two verification cases performed used the input values provided in Table 6.5. Note that the ge and P/P variables, where were set at their nominal values as a result of the screening test, have been reintroduced to the problem. Although not required by the RSE's, they will be set at values different than their nominal settings used in the RSE generation and used for the direct generation CFD runs. This will serve to verify the results of the first screening test.

Table 6.5 Verification Case Variable Settings, In-Bounds

	Supersonic Case #1	Supersonic Case #2
M_e	2	2.5
ρ_∞ / ρ_e	1.0	0.75
Alt (Kft)	50	80
θ_1 (^{o})	15	10
θ_2 (^{o})	2	10
P_e/P_∞	5	10
M_∞	2.5	5.5
γ_e	1.386	1.285
h/L	0.12	0.15

Figures 6.1 and 6.2 show the plots for the pressure distribution versus axial distance for the RSE predictions and actual CFD results. Both figures show good agreement between the predicted and actual distributions, with consistent trends. Note the small error though at the tail edge of the nozzle for Case #2. The error in these latter points in responsible for generating the overpredicted distribution in the middle section of the nozzle. This error is attributable to the poorer fit, evident in the R^2-value, for the response predictions points $x/L)_{0.9}$ and $x/L)_{1.0}$. Although this error seems significant, the fact that it is occurring after most of the flow has expanded reduces its importance. Table 6.6 shows the integrated results from the CFD runs and those obtained from the RSE predictions. The calculation was performed by applying Equations 4.1-4.3 to the polynomial fit generated from the Chi-Square analysis for each case.

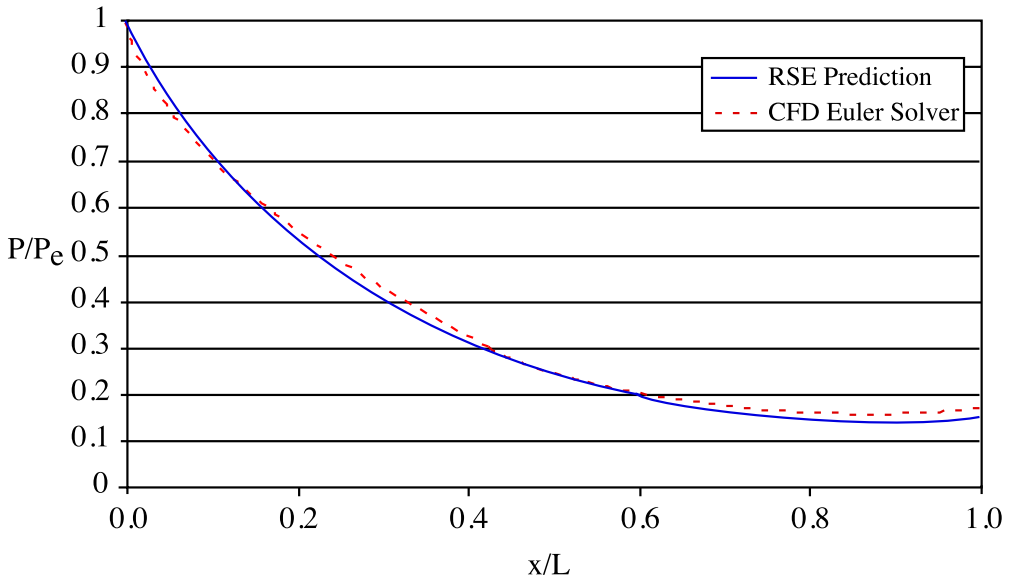

Figure 6.1 Supersonic Case #1 Verification Test Pressure Distributions

Both the RSE predictions appear to perform fairly well, as evidenced by the values presented in Table 6.6 and plotted distributions. The axial force has a relative error of 1.85% for Case #1 and 0.15% for Case #2. The normal force has a relative error of 3.18% for Case #1 and 0.15% for Case #2. Note that for Case #2, the superior integrated results are due to the cancellation of small overpredictions and underpredictions for the distribution. The distribution errors will become apparent in the moment arm predictions. Case #1's distribution is actually in much better overall agreement, although its integrated results are not as good. Some of the errors present can also be attributed to the P_e/P_∞ and γ_e parameters, which were fixed at their nominal values for the RSE generation. Additionally, while the RSE computations are nearly instantaneous, the CFD results required about 30 minutes of computer resources for both cases.

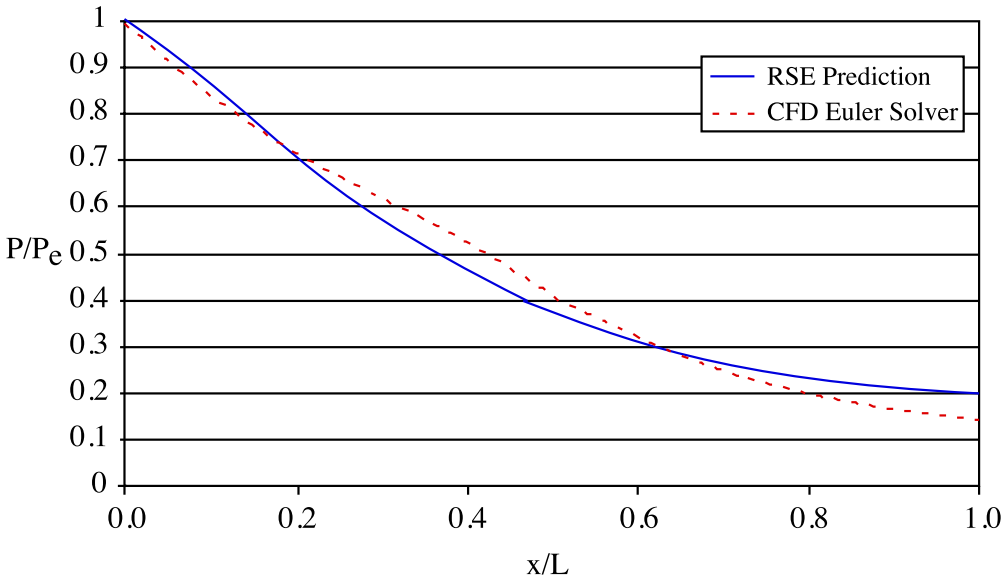

Figure 6.2 Supersonic Case #2 Verification Test Pressure Distributions

Table 6.6 Integrated Results for Supersonic Verification Cases, In-Bounds

	Case #1		Case #2	
	CFD	Predicted	CFD	Predicted
Axial Force	0.06791	0.06667	0.08065	0.08053
Normal Force	0.34822	0.33715	0.45741	0.45673
Moment Arm	0.33835	0.33229	0.34927	0.36246

Hypersonic Tests

These verification cases used the input values shown in Table 6.7. Note again that the P_e/P_∞ and ρ_∞/ρ_e variables have been reintroduced to the problem. This will serve to verify the results of the second screening test.

Table 6.7 Verification Case Variable Settings, In-Bounds

	Hypersonic Case #1	Hypersonic Case #2
M_e	3.3	2.19
ρ_∞/ρ_e	0.15	0.4
Alt (Kft)	115	80
θ_1 (^{o})	20	12
θ_2 (^{o})	9	5
P_e/P_∞	60	30
M_∞	12	7.5
γ_e	1.24	1.26
h/L	0.08	0.12

Figures 6.3 and 6.4 show the plots for the pressure distribution versus axial distance for the RSE predictions and actual CFD results. Both figures show good overall agreement. Table 6.8 shows the integrated results from the CFD runs and the RSE's.

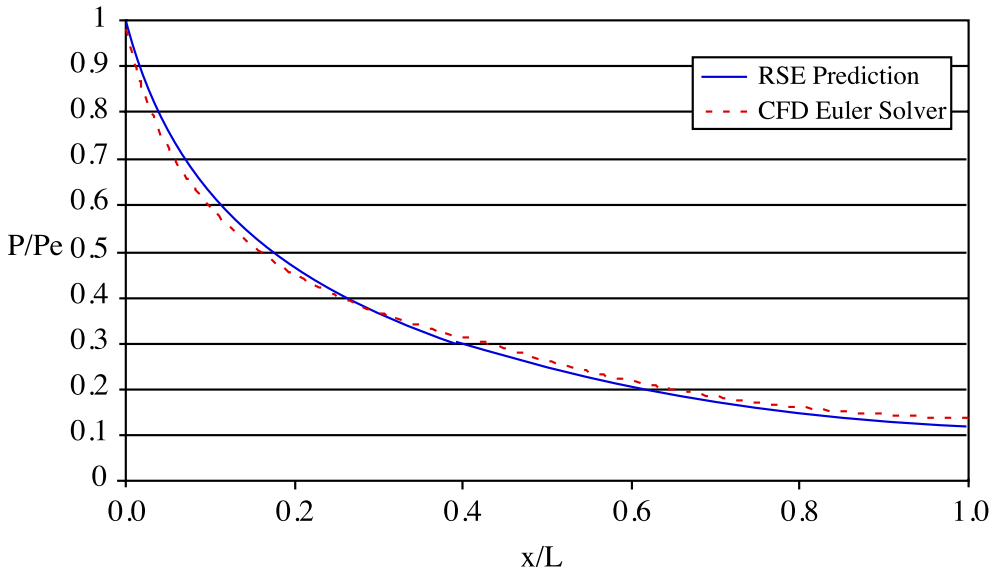

Figure 6.3 Hypersonic Case #1 Verification Test Pressure Distributions

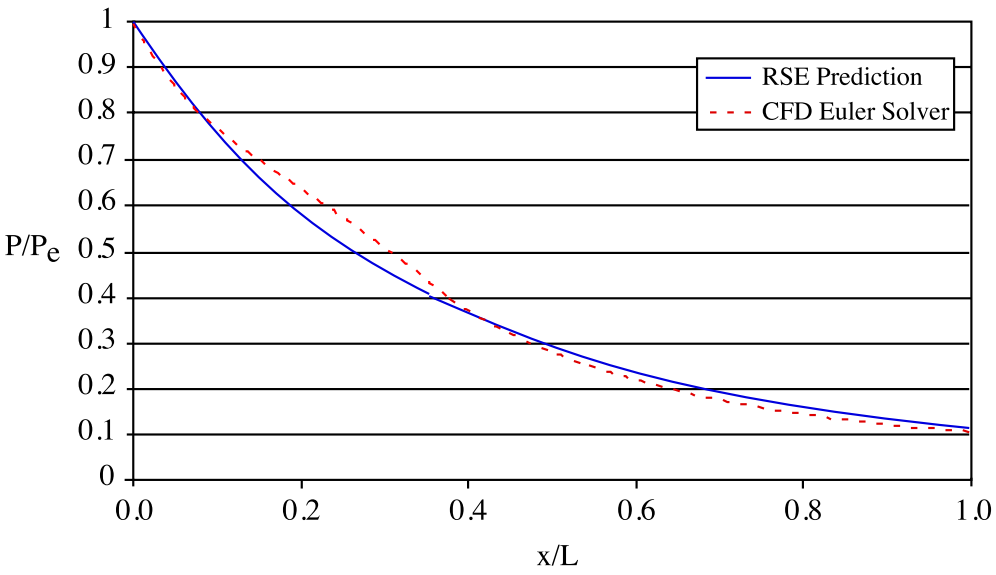

Figure 6.4 Hypersonic Case #2 Verification Test Pressure Distributions

The axial force has a relative error of -0.77% for Case #1 and -2.34% for Case #2. The normal force has a relative error of -2.02% for Case #1 and -1.91% for Case #2.

Table 6.8 Integrated Results for Hypersonic Verification Cases, In-Bounds

	Case #1		Case #2	
	CFD	Predicted	CFD	Predicted
Axial Force	0.09511	0.09437	0.06599	0.06445
Normal Force	0.32072	0.31424	0.37504	0.36789
Moment Arm	0.35796	0.34574	0.31867	0.33146

6.4 Confidence Test Cases for Variable Settings Out-of-Bounds

In order to test how well the RSE models perform when extrapolating outside of their design variable ranges, out-of-bounds confidence tests were performed. These verification cases used the input values shown in Table 6.9. Note that only variables that contribute smaller effects to the responses are placed outside their normal operating ranges. It is expected that if any of the geometric parameters were set at values outside their ranges, the errors will be significant due to the large impact these parameters already have on the value of the response.

Figures 6.5 and 6.6 show the plots for the pressure distribution versus axial distance for the out-of-bounds confidence tests. The supersonic set shows good trend agreement with the CFD solver results, with a small underprediction of the pressures from x/L)=0.2 to x/L)=0.6. Table 6.10 provides the integrated results from the CFD runs and for those based on the RSE predictions.

Table 6.9 Out-of-Bounds Verification Case Variable Settings

	Supersonic Case #3	Hypersonic Case #3
M_e	3.0	2.5
ρ_∞ / ρ_e	0.25	0.1
Alt (Kft)	100	140
θ_1 (°)	17.0	15
θ_2 (°)	7.0	10
P_e/P_∞	60.0	40
M_∞	7.0	14
γ_e	1.26	1.22
h/L	0.075	0.1

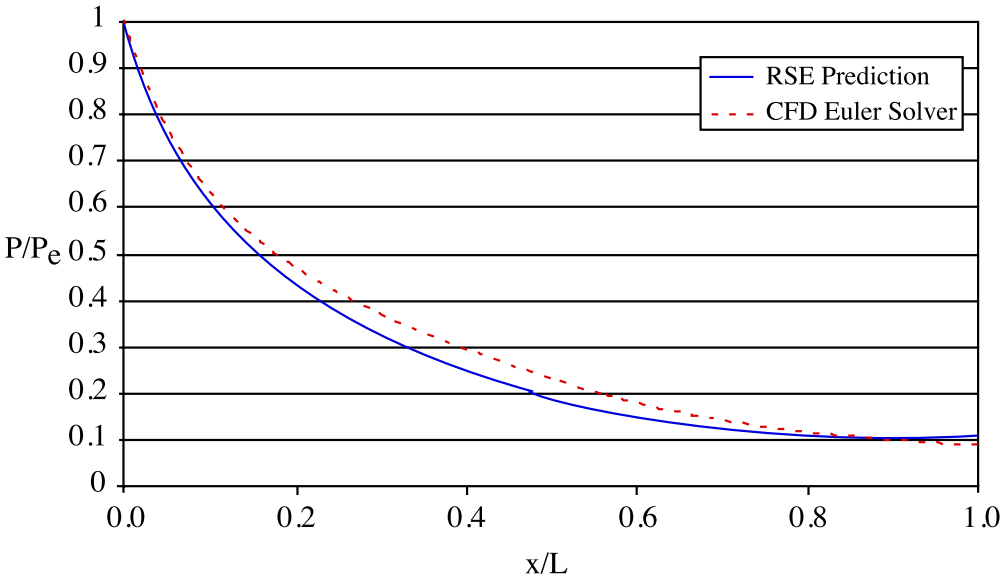

Figure 6.5 Supersonic Case #3 Verification Test Pressure Distributions

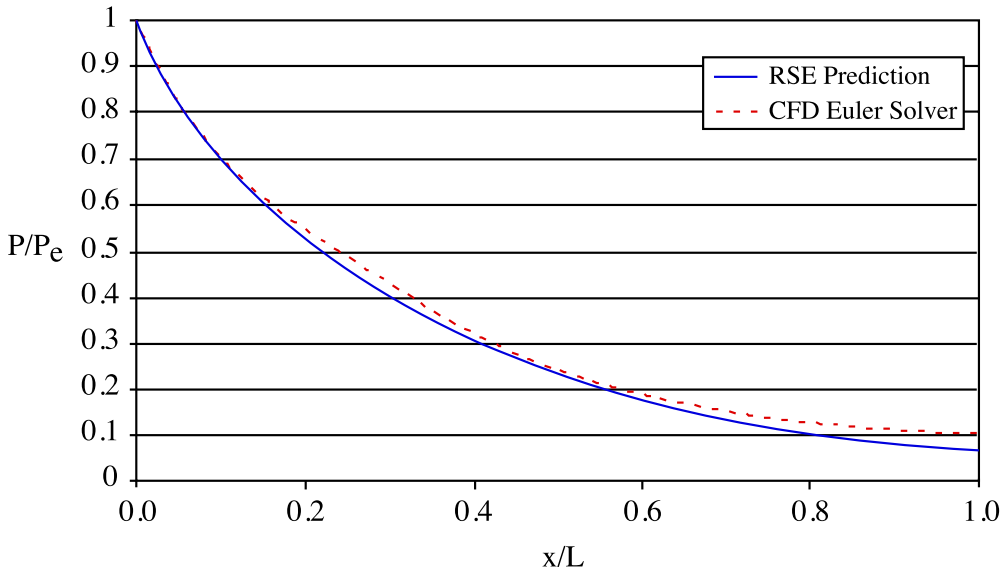

Figure 6.6 Hypersonic Case #3 Verification Test Pressure Distributions

The axial force has a relative error of -6.9% for the supersonic case and –4.78% for the hypersonic case. The normal force has a relative errors of -7.26% and –5.54% for the supersonic and hypersonic cases, respectively. Although the supersonic error values are much higher than for cases with parameter values in-bounds, the results are still within the desired accuracy. This demonstrates that the RSE equations continue to predict the correct distribution outside their intended variable ranges, but with slowly increasing errors. For the hypersonic cases, the distribution does not appear to match as well as the supersonic cases, but the integrated error is much less. This is mainly due to the "sum of the small errors" effect, with overpredicted values canceling out underpredicted values.

Table 6.10 Out-of-Bounds Verification Case Integrated Results

	Supersonic Case #3		Hypersonic Case #3	
	CFD	Predicted	CFD	Predicted
Axial Force	0.07595	0.07071	0.08064	0.07679
Normal Force	0.30088	0.27902	0.33407	0.31556
Moment Arm	0.31859	0.31975	0.31993	0.30489

CHAPTER VII

SCCREAM DESIGN TOOL

To properly assess the advantages and disadvantages of various A/B design options at the conceptual vehicle level, an engine performance analysis tool is required. This tool must be capable of modeling engine performance effects that will subsequently be propagated throughout the conceptual design process via trajectory analysis, weight assessment, fuel balance calculations, thermal environment, life cycle cost, etc. For a given engine configuration, the tool will need to generate engine thrust and Isp as a function of altitude and Mach number for a variety of operating modes.

A new computer program for the analysis of advanced engines has been created. Called SCCREAM, for Simulated Combined-Cycle Rocket Engine Analysis Module, it is intended for use in the conceptual phase of air-breathing launch vehicle design[56,57,58]. The analysis methods implemented in SCCREAM are consistent with those described in the chapter titled "Propulsion System Performance Modeling".

7.1 Code Structure

SCCREAM is written in the object-oriented (OO) C++ programming language. One of the basic tenets of OO programming is code modularity, thus SCCREAM is constructed from numerous C++ 'class' data structures (i.e. modules)[59]. This modularity allows for the code to be reusable, quickly incorporate new analysis capabilities, and to be easily configured to model new engine designs. The basic file structure of the code is shown in Figure 7.1, with arrows representing the direction of data transfer and file access privileges.

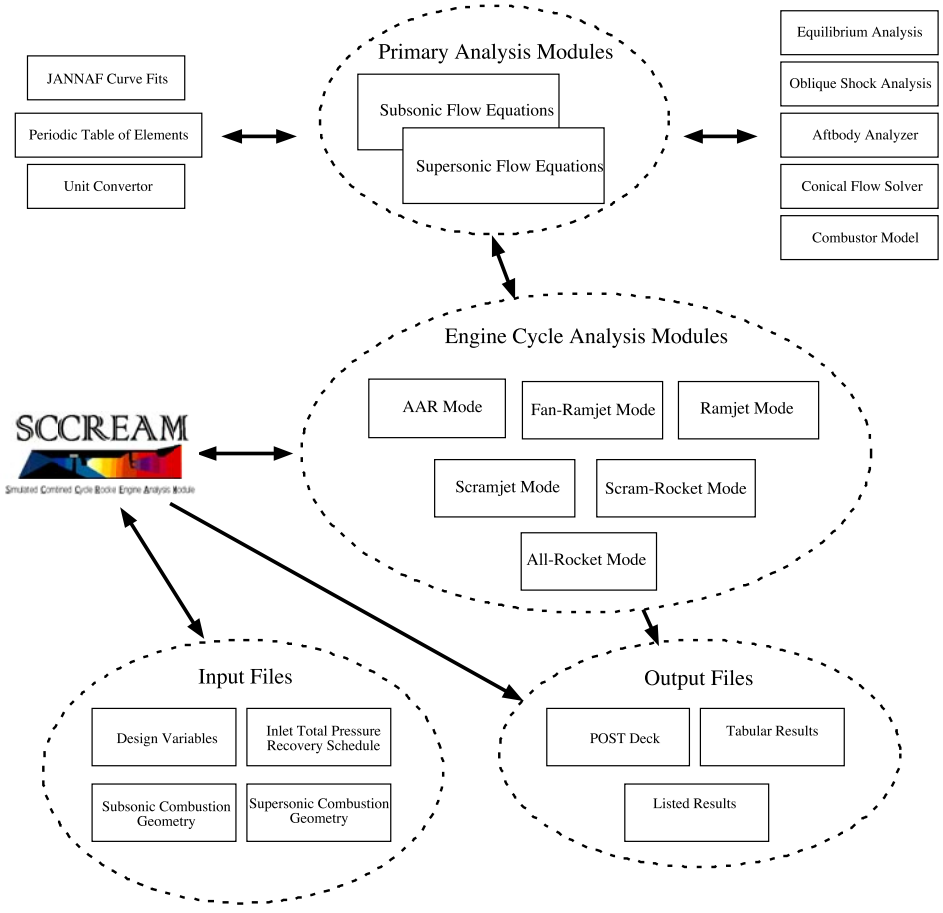

Figure 7.1 SCCREAM Code Flowchart

7.2 Modeling Capabilities

7.2.1 Engine Modes

SCCREAM has the capability to predict performance for a variety of engine operating configurations or 'modes'. Theses modes include: air-augmented rocket (AAR) or ejector mode, fan-ramjet (FRJ), ramjet (RJ), scramjet (SJ), scram-rocket (SR), and all-rocket. The ramjet and scramjet modes can be for RBCC configurations (rocket in the duct) or traditional RJ and SJ configurations.

In AAR mode, the internal rocket thrusters are firing in the engine and the inlet is entraining air due to the pumping effect of the rockets in the duct. The thrusters can be operated over a range of throttled mass flowrates, with a 0% throttle (i.e. rocket flow is off) yielding the same performance results as the RJ mode at similar flight conditions. These two flows mix and the combined, chemically reacted 'mixed-out' flow is assumed to be subsonic. Additional fuel can be added to this flow in the main combustor to react with the excess oxygen. Typical Isp values for this mode are from 350-450 seconds at SLS conditions with hydrogen fuel. The ratio of the entrained air flow to rocket mass flow, known as the bypass ratio, is typically between 0.5 and 2 at SLS conditions.

In FRJ mode, a single-stage fan is located in the engine downstream of the diffuser and upstream of the rocket thrusters. The internal rocket thrusters are off, but the main combustor is supplying fuel to the captured airflow. It should be noted that this fan is also operational in the AAR mode. Performance for the fan is specified by providing the total pressure rise across the stage. The fan typically provides about a 500 second increase in Isp over the ramjet mode Isp.

In RJ mode, the rocket thrusters and fan (if present) are not operating. With the exception of a possibly large static pressure rise in the mixer section, the engine operates as a traditional ramjet engine. Maximum ramjet performance typically occurs around Mach 4, with Isp's in the range of 3,500-4,500 seconds for hydrogen fuels. Similarly, in SJ mode, the rocket thrusters and fan are not operating. Maximum scramjet performance typically occurs around Mach 8 with Isp's around 2,500 seconds.

In SR mode, the rocket thrusters are reignited and mix with the incoming supersonic airstream. The resulting 1-D, 'mixed-out' flow is now assumed to be supersonic. Additional fuel is injected in the main combustor and all combustion processes occur supersonically. Like the AAR mode, the rocket thruster can be operated over a range of throttled mass flowrates. SR mode Isp's are typically from 450-700 seconds.

In the all-rocket mode configuration, the internal thrusters are ignited but airflow is not allowed to enter the engine (i.e. inlets are sealed shut). The rocket flow is allowed to expand throughout the entire engine and onto any aftbody surfaces, therefore a very high expansion ratio (ε) nozzle is assumed for the thrusters. For throttled mass flow cases, the rocket throat area determined at the 100% throttle case is maintained and the chamber pressure (P_c) is varied to choke the reduced mass flowrate. For a high-performance thruster chamber and large expansion ratio, the all-rocket mode Isp can be from 455 to 470 seconds.

7.2.2 Propellant Types

SCCREAM's equilibrium chemistry routine is capable of modeling chemical reactions with 12 product species. The species included are: H_2, H, O_2, O, OH, H_2O, N_2, N, NO, Ar, CO,

and CO_2. Curve fit data for the formation enthalpy, sensible enthalpy, Gibbs free energy, and constant-pressure specific heats from the JANNAF tables have been generated to eliminate time-consuming property table lookups[60]. The general form of these models are as piecewise-continuous polynomials and exponential equations with temperature as the independent variable.

For the rocket thruster analysis, propellant combinations with gaseous oxygen (O_2) or hydrogen peroxide (H_2O_2) oxidizers can be selected. For the fuel options, thermodynamic data for gaseous hydrogen (H_2), methane (CH_4), propane (C_3H_8), and JP-5 ($C_{10}H_{22}$) have been included. These fuels can be used in any combination with the specified oxidizers. Additionally, mono-propellant hydrogen peroxide at a specified purity level (eg. 90% H_2O_2, 10% H_2O) can also be analyzed. Separate initial temperatures for both the fuel and oxidizer can be specified.

For the main combustor, the fuel options include: hydrogen, methane, propane, and JP-5. Similarly to the rocket, an initial fuel temperature can be specified. Disassociation of the air molecules (i.e. nitrogen and oxygen) at elevated temperatures is accounted for by the presence of monotamic nitrogen (N), nitrogen oxide (NO), and monotamic oxygen (O).

7.2.3 Aftbody Analysis

The RSE's and Chi-Square fitting routine have been incorporated into SCCREAM. For both the supersonic and hypersonic sets, the lower and upper variables ranges have been used as limits for parameter values. If a particular flight condition or engine design

generates a variable setting that exceeds the valid ranges, that variable is replaced with the minimum or maximum value. This is only used for obtaining the non-dimensional pressure distribution. The actual variable values are always used when dimensionalizing the integrated values (eg. a ramp angle). For AAR, FR, and RJ engine cycle analysis, the supersonic RSE set is used. For SJ and SR mode analysis, the hypersonic sets are used.

In the event that the static pressure at the combustor exit is equal to or below atmospheric pressure (i.e. overexpanded), the aftbody analysis is bypassed and the axial and normal force contributions from the nozzle section are zero.

7.2.4 Earth Atmosphere

To accommodate engine performance analysis over a wide range of altitudes, the 1962-year Standard Atmosphere model has been included to provide freestream static temperatures and static pressures for altitudes from sea-level to 250K ft. at increments of 5K ft. [61]. A linear interpolation routine is used to determine properties at altitudes other than those provided. The atmospheric density can be computed using the ideal gas law shown in Equation 3.4. Table 7.1 provides the mass fractions for the air composition. This composition is assumed to be constant at all altitudes.

Table 7.1 Composition of Air

Species	Mass Fraction (Y_i)
Nitrogen (N_2)	0.75529
Oxygen (O_2)	0.23146
Argon (Ar)	0.01325

7.2.4 Inlet Pressure Recovery Schedule

The default total pressure recovery in SCCREAM is based on a military inlet specification (MIL-SPEC) schedule, shown in Figure 7.2. These performance values assume the inlet is always operating at its design point (i.e. peak efficiency). This schedule can be easily replaced with any other schedule that can be represented as an n^{th}-order polynomial with the Mach number as the independent variable and the total pressure ratio as the dependent variable.

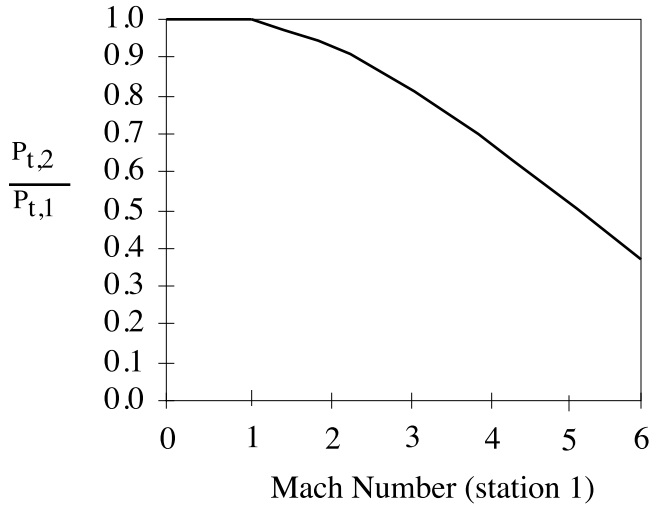

Figure 7.2 MIL-SPEC Inlet Total Pressure Schedule

7.3 User Interface

SCCREAM can operate either as a standalone program or as integrated tool in a larger multidisciplinary conceptual design process. Two options exist for interacting with the tool: a text-based mode and a web-based mode. The text-based mode is ideal for scripting and automating SCCREAM in the design environment. The preferred interface for manual user operation is via the World Wide Web (WWW) using standard web-browsing software.

7.3.1 Text-Based

The text-based mode of SCCREAM allows users to execute the code from a UNIX command line. All input files, as shown in Figure 7.1, are text based and can be easily read and modified by the user with any text editor.

Upon execution, the user is prompted to select the desired engine configuration to be analyzed by SCCREAM. There are eleven options and the selection will determine the combination of engine cycles that will be analyzed. For example, selection of the Ejector Scram-Rocket (ESR) engine will invoke the analysis modules for AAR, RJ, SJ, SR, and all-rocket modes. If the Ejector Ramjet (ERJ) engine is selected, only the AAR, RJ, and all-rocket modes will be analyzed. Additionally, the user has the option to specify a thrust requirement in AAR mode for RBCC engines. Using the defined engine geometry, SCCREAM will vary the flowrate of the rocket thrusters ($\dot{m}_{rocket}$) to match the total required thrust from the engine. This thrust requirement can be at any specified flight Mach number and altitude, but is typically performed at SLS conditions. Allowing for flight condition sizing is useful for a vehicle that performs a staging maneuver or accelerates down a mag-

lev track. During execution, the user is provided with real-time updates indicating successful or unsuccessful completion of a particular operating mode.

7.3.2 Web-Based

As previously mentioned, the web-based interface is the preferred method for operating SCCREAM. The web-interface allows for execution and retrieval of the results from SCCREAM over the web from any computing platform (eg. Mac, PC, Unix). The user is required to have an Internet browser (eg. Netscape, Internet Explorer). This interface provides options to access either a 'novice' or 'expert' version of the code, setup custom engine configurations, and view performance results after an analysis.

In addition to remote operation, the interface allows for easy error checking before program execution. Hyper-links for each variable are set up to provide a brief description of each input parameter and give typical ranges. Sample engine configurations with default settings have been included for a variety of A/B & RBCC vehicle designs.

Web-Wrapper

The web-interface is a wrapper around the text-based version of SCCREAM so the primary SCCREAM code, shown in Figure 7.1, is unaltered. The wrapper is composed of three different programming languages. They are the common Hyper-Text Markup Language (HTML), JavaScript, and Practical Extraction Report Language (Perl). Perl is used in CGI (Common Gateway Interface) scripts and allow the web page to issue commands to the fileserver[62]. This web-interface wrapper and its execution procedure is shown in Figure 7.3.

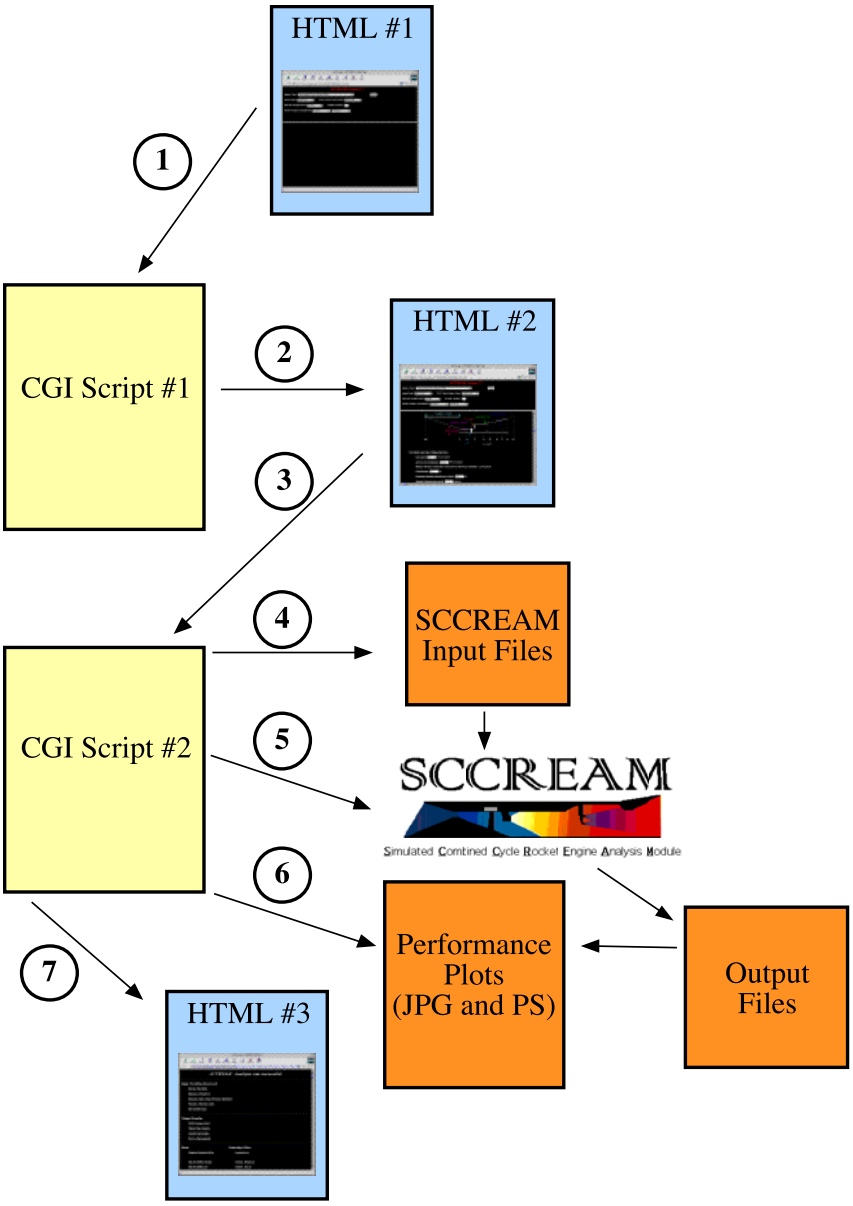

Figure 7.3 SCCREAM Web-Interface Wrapper

The interface wrapper can be broken into 7 distinct stages. The first stage involves the document HTML #1 obtaining some basic engine configuration information from the user

(eg. engine type, propellant combinations, forebody shape). This data is passed to CGI Script #1, which dynamically generates HTML #2. The input fields and default input values for this page have now been customized for the user based on data obtained from HTML #1.

JavaScript routines for error checking, dynamic page updates, and input variable range checking have also been incorporated in to HTML documents[63]. This helps to limit the possibility of errors being generated when SCCREAM executes. For example, if the user accidentally specifies a combustor efficiency greater than 100%, a warning message generated by the Javascripts will be displayed. This message will identify the name of the variable with the infeasible input value and state the allowable ranges. The JavaScript also creates a more dynamic page, with default input values automatically changing based upon a user's selections. As an example, if a non-supercharging RBCC engine (i.e. no fan in flowpath) is selected, the fan pressure ratio automatically defaults to 1.0, for no total pressure rise, and is eliminated as an available input field to the user. If the user selects the pure-ramjet option, all input fields associated with the rocket primary subsystem are eliminated.

The HTML portions utilizes the 'post' form method for transferring data to the machine hosting the SCCREAM executable[64]. The 'post' method is preferable over the 'get' method when transferring more than one piece of information. The web pages (HTML #1 and HTML #2) consists of radio buttons, pull-down menus, and text fields for the SCCREAM input parameters. This allows for easy configuration changes and updating of the engine model. Figure 7.4 provides a partial screen shot of the web interface for SCCREAM.

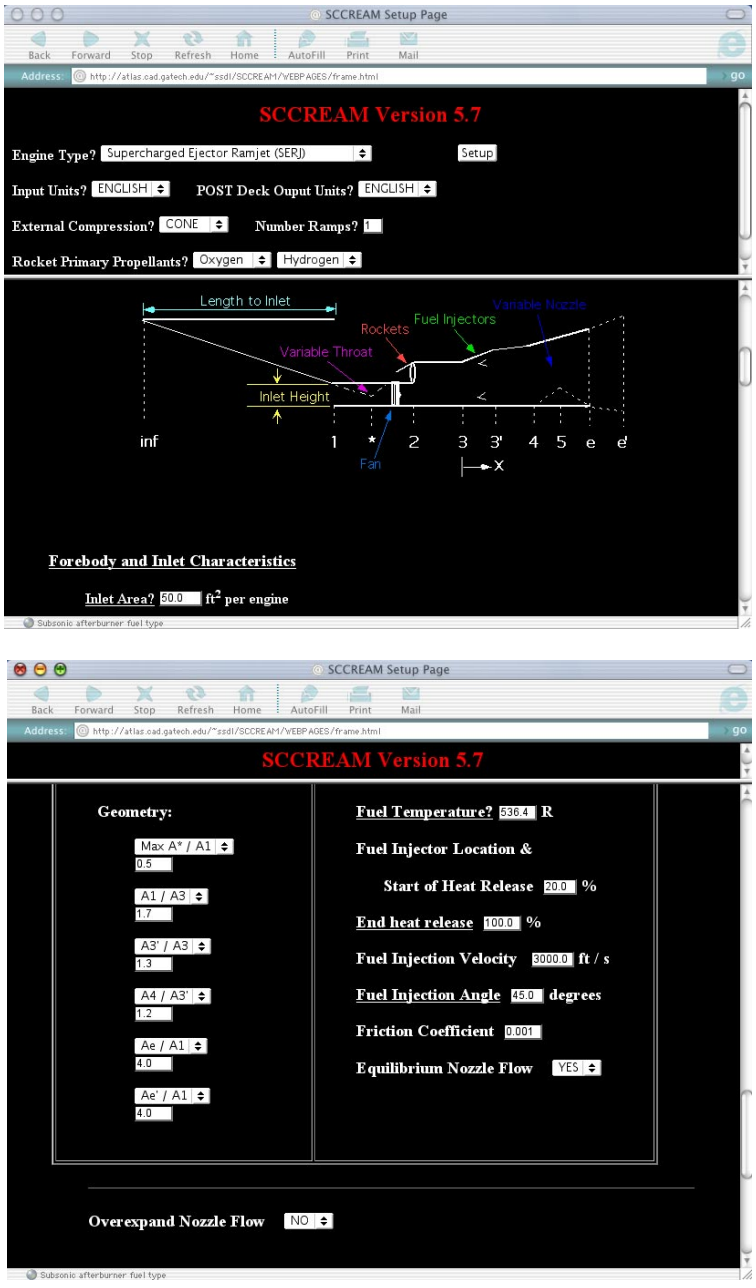

Figure 7.4 SCCREAM Web-Interface Snapshots

After the user has entered their engine model information, the data is passed to CGI Script #2. This script performs 4 tasks, the first of which is to generate the SCCREAM input files.

This script has file access to the host machine and can create and destroy files as necessary. Once all the input files have been written, the script executes SCCREAM through a 'system call' to the host workstation. SCCREAM is then executed using the previously generated text input files. Upon completion and successful execution of SCCREAM, the CGI script makes another function call to the GNUPLOT software [65]. A series of plot templates are used, along with SCCREAM's output files to generate postscript files of the engine performance. These postscript files can easily be converted to an image file, using 'GhostScript'[66], which allows the plots to be displayed to the user over the web. Finally, the CGI Script #2 dynamically generates HTML#3, with links to all output files generated for the user's design, as well as the plots in postscript and JPEG format.

7.4 Run-Time

Execution times range from a few seconds for an all-rocket analysis case to a few minutes for a standard, non-throttled A/B or RBCC engine configuration analysis on a 350 Mhz R12000 Unix workstation. A 'standard' engine map consists of 3 or 4 engine modes. Table 7.2 shows typical ranges for various engine modes constituting one full analysis run. Note that in contrast to many other analysis tools, SCCREAM is capable of analyzing hundreds of flight conditions in roughly the same amount of time as other codes take to analyze single flight condition.

For throttled engine cases, the run time will increase proportionately with the number of throttle settings. For the RJ and SJ mode operation, the 'throttle' applies to the equivalence ratio (ϕ) of the engine. This performance information is especially useful for flyback and cruise vehicle type scenarios (non-accelerator missions).

Table 7.2 Typical Analysis Ranges for Various Engine Modes

Engine Mode	Altitudes (Kft)	Altitude Stepsize (Kft)	Mach Numbers	Mach Number Stepsize	Total Cases Analyzed
AAR	0-60	10	0-3	0.25	91
RJ	30-80	10	2-6	0.25	102
SJ	70-110	10	6-12	0.5	65
All-rocket	-	-	-	-	1

7.5 Output-Files

SCCREAM generates a number of output files with results in a variety of formats. The files consist of all relevant engine performance parameters for every analysis case examined during a run. The primary output file and most critical in a design process is the engine deck. For propulsion system analysis and design purposes, a file containing all fluid property values through the engine is available. As previously mentioned, the web-interface also provides plotted maps of the engine performance for each mode.

7.5.1 POST Engine Deck

SCCREAM automatically creates formatted engine decks for the trajectory simulation program POST – Program to Optimize Simulated Trajectories[67]. The engine decks are either 2-D lookup tables with Mach number and altitude as independent variables or 3-D lookup tables with Mach number, altitude, and throttle setting as independent variables. This performance map allows the trajectory analyst more control over optimizing the flight path

of the vehicle. Instead of only providing the analyst with results over an assumed flight path, SCCREAM provides a flight envelope over which the engine operation and vehicle-level impact can be examined. Figure 7.5 provides a sample 3-D POST deck for a throttled engine's ramjet mode Isp. The throttle is represented by the variable 'eta'. The throttle settings are all normalized by the maximum throttle value.

```
 c Ramjet Mode Isp Values
l$tab table=5hisp3t,3, 3heta, 4hmach,
5hgdalt, 4,4,5,27*1,

 50000,
  2.0,
      1.0,    1413.12, / inlet is unstarted
    0.667,    1612.06, / inlet is unstarted
    0.333,    1845.88, / inlet is unstarted
      0.0,       0.0, / inlet is unstarted
  5.0,
      1.0,    1460.47, / inlet is started
    0.667,    1572.53, / inlet is started
    0.333,    1738.73, / inlet is started
      0.0,       0.0, / inlet is started
  7.0,
      1.0,    1338.87, / inlet is started
    0.667,    1372.43, / inlet is started
    0.333,    1221.65, / inlet is started
      0.0,       0.0, / inlet is started
```

Figure 7.5 Sample Engine Deck for POST

The static pressures inside an airbreathing engine can be substantial and will significantly effect the weight of an engine. The trajectory flown by the vehicle will have the strongest influence on the maximum internal pressures that will be experienced by the engine. In many cases, for freestream dynamic pressures (q_∞) greater than 1,500 psf, ramjet mode

static pressures in excess of 200 psi can easily develop as the flight Mach number is increased. This can significantly increase the weight of an engine, and this information needs to be supplied to an engine weight and structural model.

To allow for tracking of these engine pressures, included in the POST engine deck is a table that contains the maximum static pressure experienced by the engine at each flight condition. This information can easily be monitored during the trajectory and can be passed to an engine weight estimation code, like WATES, during each iteration of the vehicle closure process[68]. Alternatively, a maximum static pressure limit can be set in the trajectory model and POST can be constrained not to let the vehicle exceed this value over the course of the trajectory.

7.5.2 Plots

As mentioned previously, the web interface can generate performance plots for the users engine design. The plotting capability allows the designer to quickly assess their engine's performance and provides an easy method of comparing different engines.

The resultant JPEG image from GNUPLOT and Ghostscript can be displayed to the user through the web browser. The postscript file can also be downloaded by the user and provides a crisp, black and white image for the user to send to their local printer. Figure 7.4 provides a sample JPEG image taken directly from the SCCREAM web interface. It was generated for a Supercharged Ejector Ramjet (SERJ) engine with a sea-level static thrust of 75,000 lbs. and fan pressure ratio of 1.2. The rocket system used LOX/JP-5 propellants and the afterburner used JP-5.

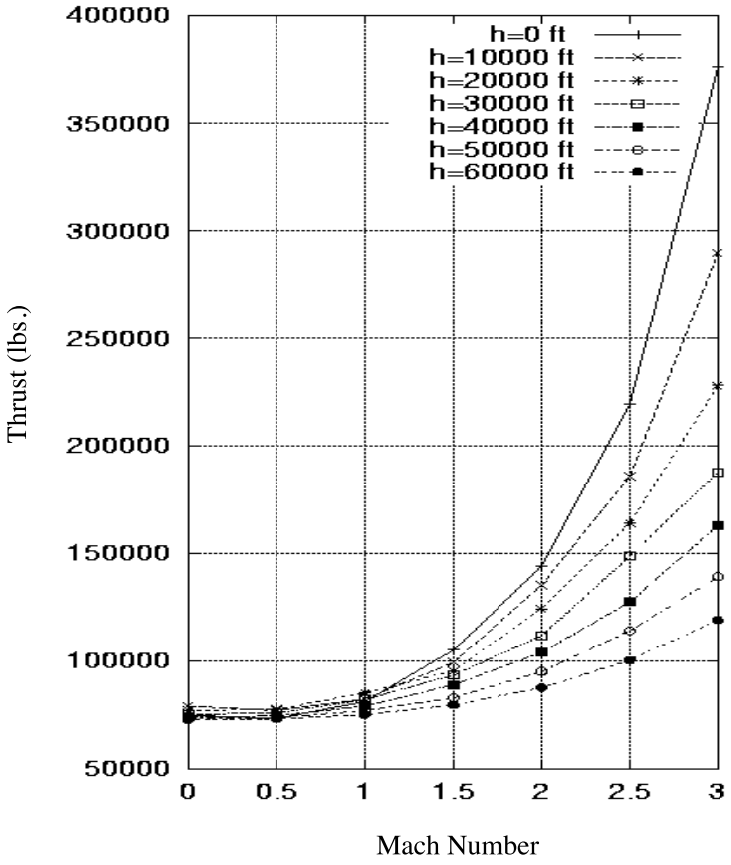

Figure 7.6 Sample Web-Interface Performance Plot

7.6 Verification Cases

Numerous verification runs were performed to benchmark SCCREAM performance predictions with those of other existing tools. While it cannot be determined exactly how the

engine performance will measure up under actual flight conditions, the relative accuracy of various prediction tools can be determined and any differences examined.

7.6.1 Chemistry Routine

Results from the chemistry model implemented in SCCREAM were compared with those obtained from the common, industry-accepted tool named CEA or Chemical Equilibrium with Applications[44]. CEA has been under development since 1975 at NASA Lewis Research Center, primarily under Gordon and McBride. The code features an extensive chemical database with thermodynamic data for hundreds of species. The code can handle a variety of equilibrium problem formulations (eg. t&p, h&p, s&p) for reactant and product species in both for gaseous and condensed forms.

For the verification cases, two propellant combinations were examined over a range of pressures and mixture ratios. The propellant combinations were oxygen-hydrogen and oxygen-methane. Two different equilibrium pressures were specified at 1,000 psi and 50 psi. For the O_2-H_2 case, mixture ratios of 1.5, 7.5, and 20 were examined. For the O_2-CH_4 system, mixture ratios of 2, 4, and 10 were considered. Note that the stoichiometric mixture ratios are 7.95 and 4 for O_2-H_2 and O_2-CH_4 systems, respectively. The cases considered ranged from very fuel rich, to near stoichiometric conditions, and then very fuel lean. For all cases, both the oxidizer and fuel were at an initial temperature of 536.4 R.

	P_c 50 psi MixR 1.5		P_c 1,000 psi MixR 7.5		P_c 50 psi MixR 20	
	SCCREAM	*CEA*	*SCCREAM*	*CEA*	*SCCREAM*	*CEA*
H_2O	0.18898	0.18899	0.6776	0.6791	0.4846	0.4847
H_2	0.8109	0.8109	0.1451	0.1448	0.0133	0.0135
O_2	0.0	0.0	0.0269	0.0266	0.3868	0.3868
$Tad\,(R)$	3,054	3,060	6,631	6,623	5,162	5,228
$\mathcal{MW}_{mix}$	5.04	5.04	15.26	15.27	22.95	22.95

Table 7.3 O_2-H_2 System Chemical Equilibrium Comparisons

	P_c 50 psi MixR 2		P_c 1,000 psi MixR 4		P_c 50 psi MixR 10	
	SCCREAM	*CEA*	*SCCREAM*	*CEA*	*SCCREAM*	*CEA*
H_2O	0.2922	0.2922	0.4558	0.4565	0.2833	0.2834
H_2	0.3579	0.3580	0.0539	0.0536	0.0056	0.0057
O_2	0.0	0.0	0.0706	0.0704	0.4683	0.4684
CO_2	0.0361	0.0361	0.1424	0.1423	0.1398	0.1397
CO	0.2939	0.2939	0.1410	0.1413	0.0197	0.0191
$T_{ad}\,(R)$	4,807	4,805	6,544	6,535	5,119	5,114
$\mathcal{MW}_{mix}$	15.88	15.88	22.74	22.75	28.14	28.14

Table 7.4 O_2-CH_4 System Chemical Equilibrium Comparisons

Table 7.3 and 7.4 present the results for the six different cases analyzed using SCCREAM and CEA. Note that for the O_2-H_2 case, only the mole fractions for the three major species (H_2, O_2, and H_2O) are provided. The mole fractions for the minor species present (O, H, and OH) were not included for brevity, but displayed similar levels of accuracy. For the O_2-CH_4 case, the carbon dioxide and carbon monoxide mole fractions are also provided.

For all cases, excellent agreement for the species mole fractions is obtained between the two codes. Additionally, the mixture molecular weight and adiabatic flame temperature are also in excellent agreement without any notable differences.

7.6.2 Combustor Model

To verify the combustor model implemented using the 'influence coefficient method', comparison cases were ran for a scramjet combustor using the industry accepted code, SRGULL [33]. SRGULL uses a 1-D Euler routine for its combustor analysis. This method is similar to the influence coefficient method, but without the assumption of a CPG at each local step. Similar to SCCREAM, the SRGULL user can establish the engine geometry, fuel injection position, heat release profile, and combustor efficiency.

For the test cases, a hydrogen fueled scramjet engine flying at a freestream Mach number of 6.5 and 8 were examined. The vehicle flying this engine had a 9° 2-D wedge forebody and flew along a constant dynamic pressure boundary of 2,000 psf. The combustor geometry modeled in SCCREAM and SRGULL were identical and corresponded to an ESJ engine design. Figure 7.7 provides the area ratios versus axial position for the test case.

After SRGULL completed its analysis, the conditions at the entrance to its combustor were used as the entrance conditions to the combustor in SCCREAM. These conditions included mass flowrate and composition (air), static pressure, static temperature, Mach number, and gamma. A constant average friction coefficient of 0.0018 was specified for SCCREAM, obtained as the average value computed in SRGULL. The fuel injection occured at an x/L value of 55%, which also corresponded to the start of the heat release/chemical reaction. A linear profile was established in SRGULL, which is the standard profile used in SCCREAM, and the end of the heat release was at an x/L value of 95%. Parallel fuel injection at a velocity of 6,000 ft/s was specified for both models. At both the Mach 6.5 and 8 conditions, an equivalence ratio of 1.0 was possible without causing a thermal choke in either combustor.

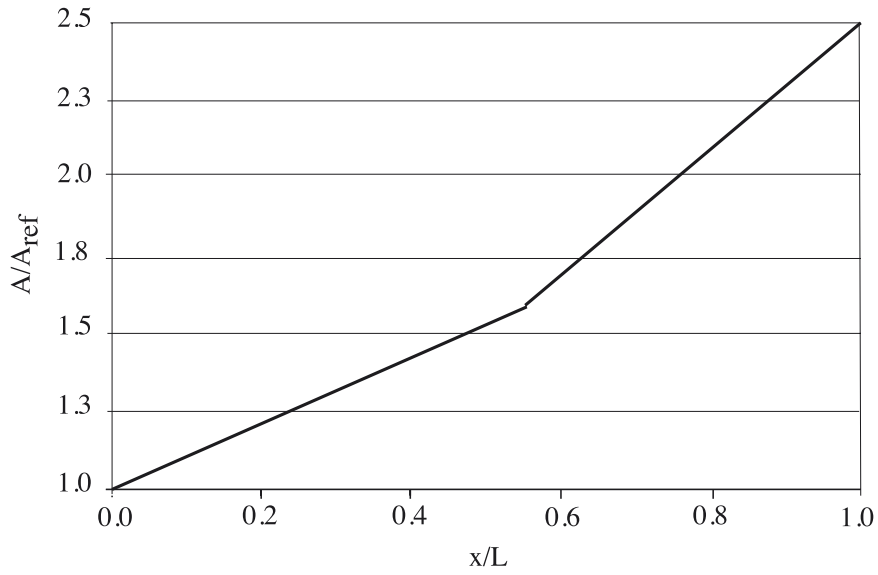

Figure 7.7 Combustor Model Verification Case Geometry

Figure 7.7 shows the Mach number distribution generated by SCCREAM and SRGULL for the Mach 8 flight conditions. The Mach 6.5 results were very similar and have not been included for brevity.

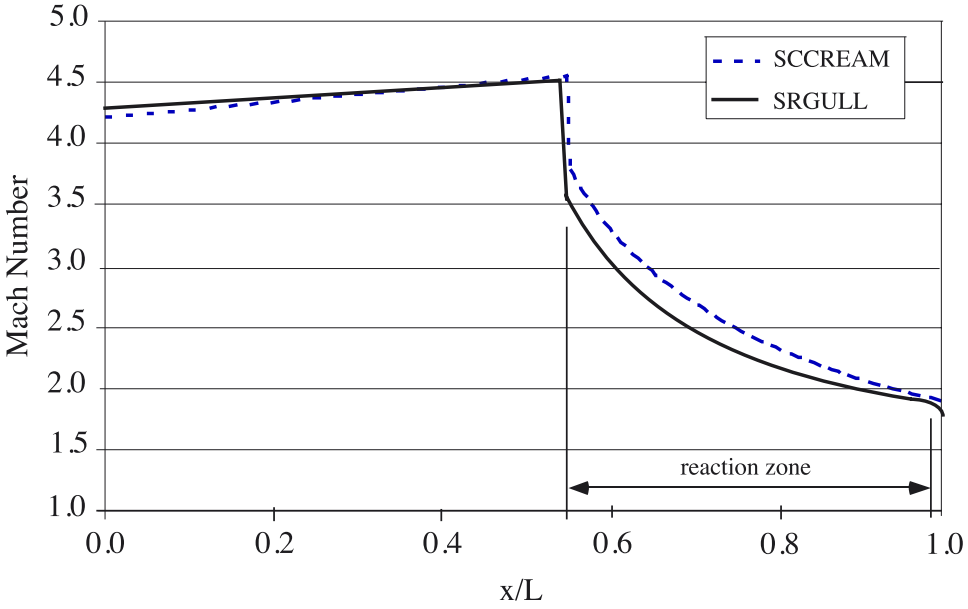

Figure 7.8 Combustor Model Verification - Mach Number Distribution

In the non-reacting region of the combustor (up to x/L=55%), SCCREAM and SRGULL have nearly identical profiles. At the location of the fuel injection, the sudden drop in Mach number is due to the addition of the fuel. SCCREAM appears to slightly underpredict the strength of this drop, but the effect is clearly captured. The remaining portion of the combustor is the chemically reacting region. SCCREAM and SRGULL both display very similar trends and profile shapes over the entire heat release process. Differences between the two curves appear to be caused by the initial differences from the fuel injection. If the magnitude of these effects agreed, it is believed that the heat release profiles would agree almost exactly.

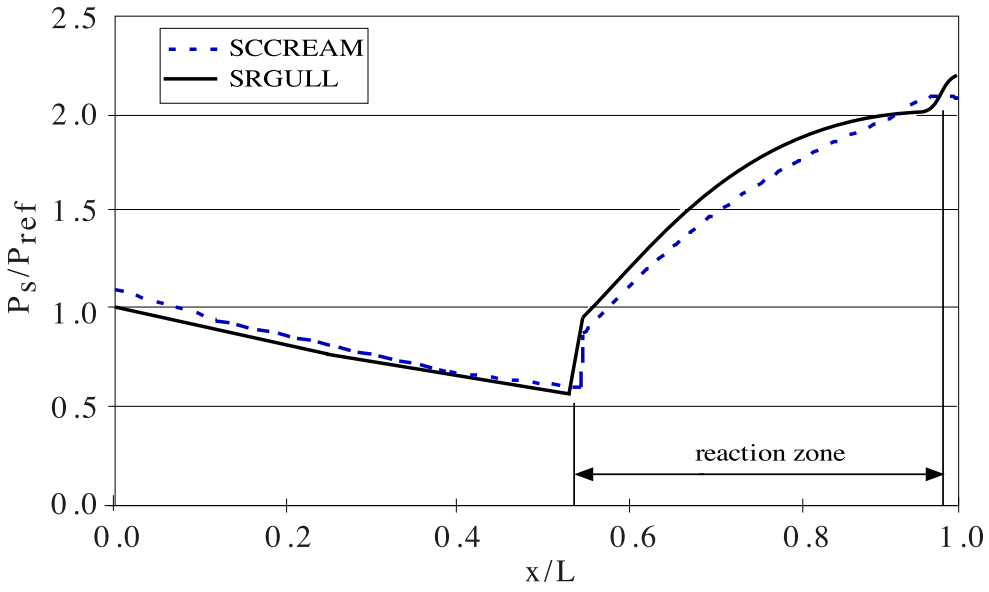

Figure 7.9 Combustor Model Verification - Static Pressure Distribution

Figure 7.9 shows the static pressure distribution in the engine. Once again, excellent agreement is obtained between the two codes. For brevity, the Mach 6.5 static pressure distribution displayed similar trends and will not be provided. These results demonstrate the proper implementation of the combustor model, correct calculation of the total temperature gradient, and prediction of the chemical composition gradients.

7.6.3 RJPA Comparisons

For comparison runs with SCCREAM, the ramjet and scramjet mode performance was analyzed and compared with RJPA for Mach numbers from 3 to 12 [29]. A generic engine configuration with moderate internal area contraction and exit flow expansion was selected.

The RJPA engine model is divided into 4 main components: the inlet, diffuser, combustor, and nozzle sections. For establishing the inlet flow conditions, the static conditions for temperature, velocity, and pressure behind the bow shock were specified for each case. These values were obtained from SCCREAM for a 2-D wedge forebody with a ramp angle of 10^{o}. The physical area of the inlet at the cowl leading edge was 20 ft^2.

The diffuser section consisted of defining the exit area, total pressure recovery, and initial guesses for the specific heat ratio. The exit area from the diffuser corresponded with the area at station '3' in SCCREAM, and was set to a value of 10 ft^2. The total pressure recovery was made to correspond to the value used by SCCREAM, at each flight condition. Any heat and friction losses in the diffuser were ignored.

A diverging combustor design was selected, so the exit area from the combustor (station 4) was 16.8 ft^2. A constant skin friction coefficient of 0.001 was defined for both modes. The equivalence ratio and initial guesses for the static pressure at the exit plane were also defined in RJPA. For cases below Mach 4, the equivalence ratio had to be reduced in order to prevent choking due to the heat addition in the combustor. If the specified equivalence ratio (ϕ) is too high in RJPA, a solution cannot be obtained. For these same cases, SCCREAM automatically throttled back the fuel flow rate from the maximum specified value of 1.0. The phi determined by SCCREAM provided starting points for determining an allowable ϕ in RJPA. It should be noted that the allowable fuel flowrate from SCCREAM was slightly higher than the value allowed by RJPA. To ensure a fair comparison, SCCREAM was run again with the same phi used by RJPA.

For the nozzle expansion, an efficiency of 98.5% and an exit area of 65 ft^2 was defined. A frozen-to-equilibrium nozzle flow ratio of 66%/34% was also used for determining the thrust and Isp values. SCCREAM and RJPA can perform the nozzle analysis for both a frozen and equilibrium flow. The frozen flow case should have lower thrust and Isp, when compared to the equilibrium case. Real nozzle performance is somewhere in between these two bounds, with chemical kinetic models suggesting it is closer to the frozen flow results. By defining a frozen-to-equilibrium ratio of 66%/34%, the non-equilibrium flow performance can be estimated by taking 66% of the frozen flow results and 34% of the equilibrium flow results. The performance results presented are for this 'real' flow case.

Figure 7.10 provides the comparative results for the thrust coefficient versus freestream Mach number. The cowl area of 20 ft^2 was used to normalize the thrust coefficient (see Equation 3.56) with a dynamic pressure of approximately 2,000 psf.

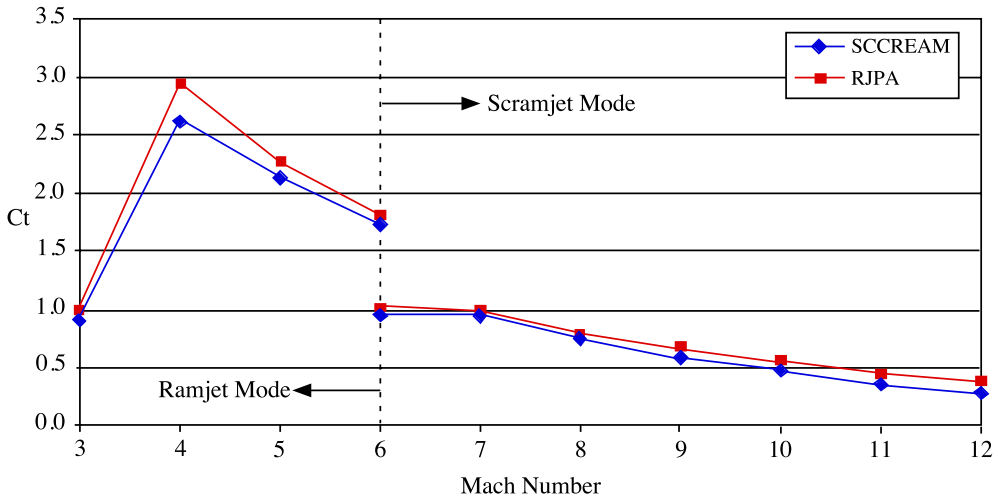

Figure 7.10 Thrust Coefficient versus Mach Number Comparisons

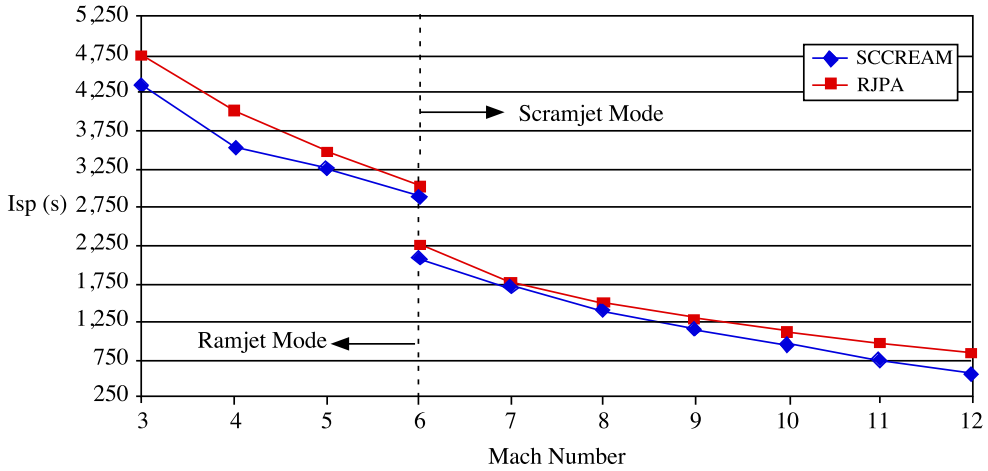

Figure 7.11 Specific Impulse versus Mach Number Comparisons

In the Mach number range of 5 to 10, SCCREAM and RJPA match fairly well, with relative differences less than 10%. At the lower Mach numbers, it appears SCCREAM underpredicts the thrust level predicted by RJPA. This is currently being attributed to SCCREAM not modeling the pre-combustion static pressure rise (i.e. the 'PSPCI' parameter in RJPA) from the shock train. This pressure rise results in different flow conditions at the start of the combustion process, which in turn affect the flow conditions exiting the combustor. These differences diminish at the higher Mach number conditions, where the effect of the shock train pressure rise also diminishes.

At Mach numbers above 10, the differences between RJPA and SCCREAM appear to be slowly increasing. SCCREAM appears to become more conservative in its performance predictions. The exact reason for this cannot be identified, but one source of difference may be due to the combustor models, with SCCREAM's marching solution and RJPA's jump solution.

Figure 7.11 provides the Isp versus Mach number comparisons. As expected based on the thrust coefficient trends, SCCREAM underpredicts the Isp predicted by RJPA at the lower, reduced ϕ, Mach numbers. From Mach 5 to 10, good correspondence between the two codes is displayed again. Above Mach 10, SCCREAM has a lower Isp in a manner consistent with the thrust coefficient profile.

7.6.4 JANNAF RBCC Workshop Results

SCCREAM was entered in an engine cycle-code comparison workshop at the year-2000 JANNAF Conference in Monterey, CA. There were multiple participants including representatives from NASA MSFC, NASA Glenn, Pratt and Whitney, and Johns-Hopkins University APL. Each participant was required to analyze similar, generic RBCC engine designs operating in three different cycle modes (AAR, ramjet, and scramjet), using their organizations preferred code. Table 7.5 summarizes some of the engine design parameters used for generation of the results. Figure 7.12 shows the thrust coefficient prediction generated by each organization using their codes. Most of the differences were due to a lack of definition on some variables that left them open to be interpreted differently be each participant. For example, a base area (A_b) was specified and some users assumed this area included the thruster exit area while others assumed it did not.

Table 7.5 JANNAF Workshop Engine Design Parameters

Engine Parameter	Value
Projected Inlet Area (ft^2)	100.0
Base Area (ft^2)	10.0
Wall-to-Combustor Inlet Area Ratio	40.0
Exit-to-Inlet Area Ratio	3.0
$\eta_{combustor}$	90.0%
η_{nozzle}	97.5%
$P_{c,thruster}$ (psia)	2,000
$\varepsilon_{thruster}$	12

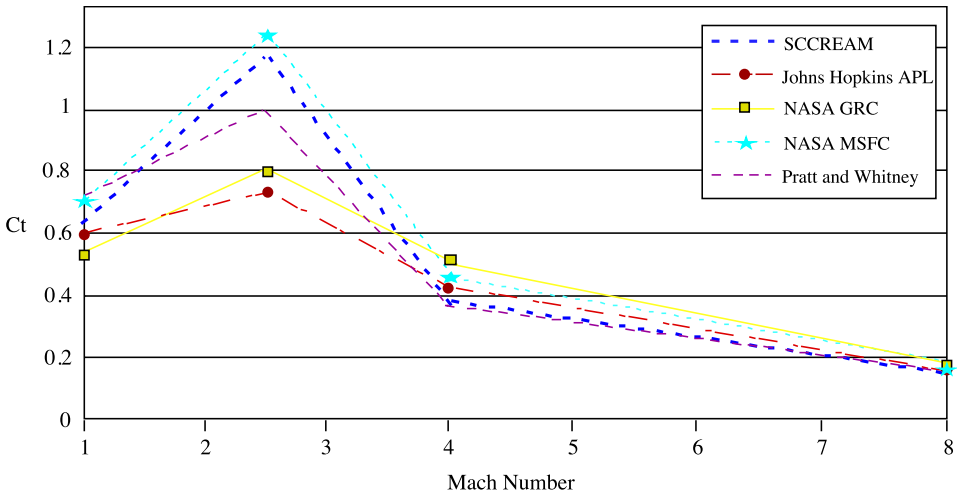

Figure 7.12 JANNAF Workshop Engine Thrust Coefficient Results

CHAPTER VIII

APPLICATION: *ABLV-GT2* SSTO VEHICLE

The *ABLV-GT2* is a conceptual design for an advanced reusable launch vehicle based on the current NASA Langley Research Center (LaRC) ABLV concept[69]. It is a Vision Vehicle class, horizontal takeoff, horizontal landing single-stage-to-orbit vehicle. Main propulsion is provided by an Aerojet-derived LOX/LH2 rocket-based combined cycle engine design. The *ABLV-GT2* is designed to deliver 10,000 lbs. to low Earth orbit (LEO) from Kennedy Space Center (KSC).

8.1 *ABLV-GT2* Vehicle Concept

The *ABLV-GT2* operates from a notional airfield at KSC. The vehicle is designed for a nominal thrust-to-weight ratio of 0.65 during takeoff. The vehicle accelerates onto a 1,800 psf dynamic pressure boundary at Mach 3, where the ramjet engines can be used (inlet is started). The vehicle initially injects to a 30x100 nmi. orbit in a 28.5^{o} inclination. The vehicle coasts to apogee position and the throttled main engines, which serve the dual purpose as OMS engines, are re-ignited to circularize the vehicle into a 100 nmi. payload delivery orbit.

Upon orbital insertion, the payload is released and the vehicle is de-orbited for the return to KSC. A deorbit delta-V capability of 350 fps is allotted for in the OMS propellants. Figure 8.1 provides a pictorial overview of the entire mission.

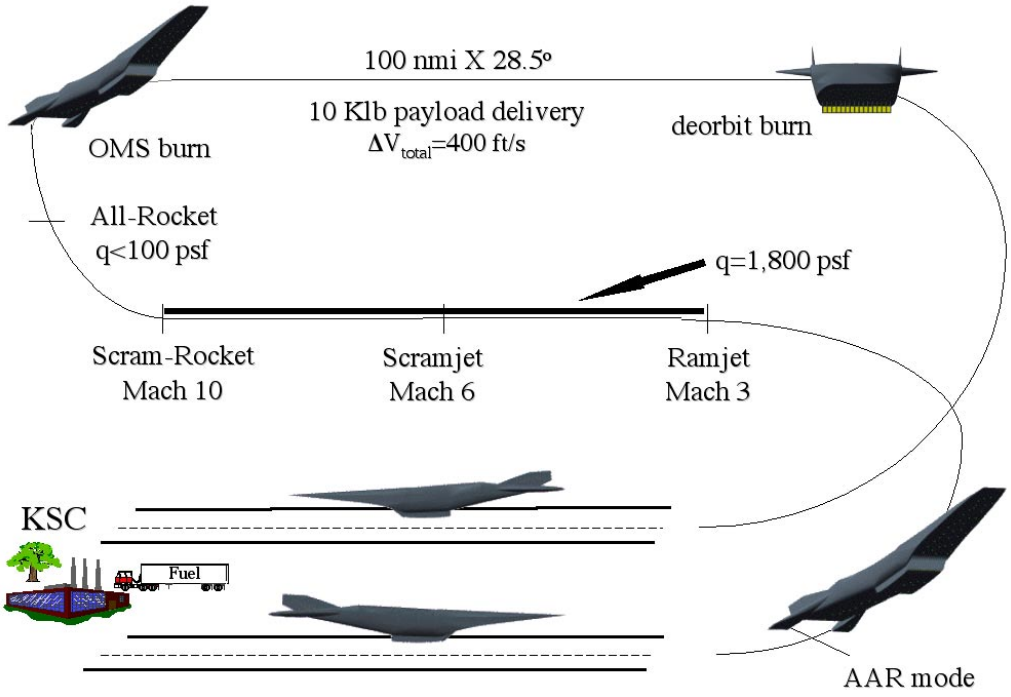

Figure 8.1 ABLV-GT2 Mission Overview

8.2 Configuration and Aerodynamics

A fuselage outer mold line (OML) representative of the LaRC configuration was created using SDRC I-DEAS, a solid modeling program[70]. The OML was used for determining surface areas for thermal protection system (TPS) coverage, estimating the primary airframe structural mass, and defining the aerodynamic model.

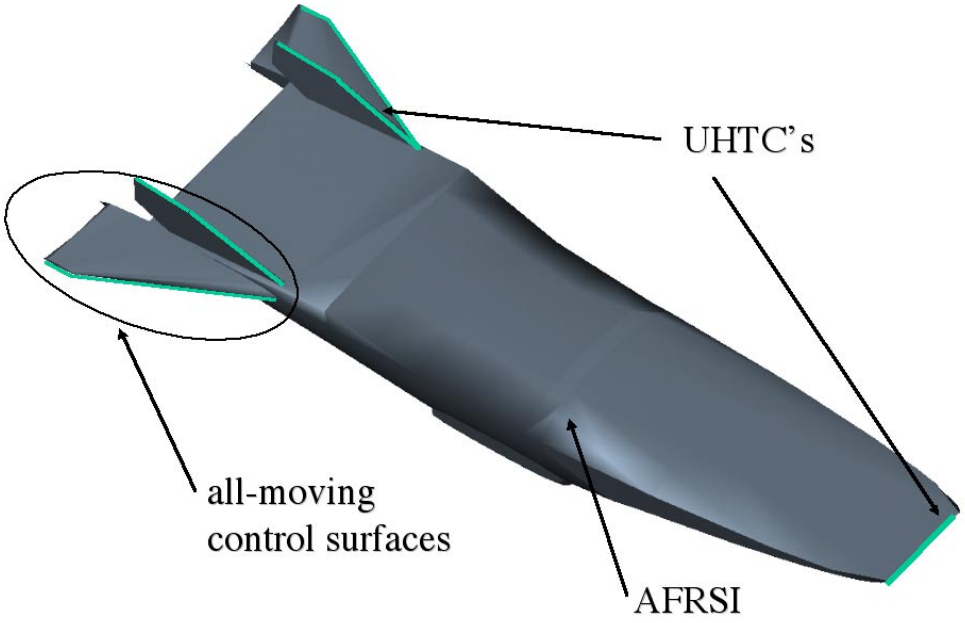

Figure 8.2 ABLV-GT2 External Fuselage CAD Model

As shown in Figure 8.3, a transparent view of the fuselage, the fore and aft vehicle volumes are occupied by LH2 tanks. These tanks are integral, that is, they share a common wall with the airframe where possible. An 11 ft. 11 ft. x 24 ft. cargo bay was reserved for the 10,000 lb. payload. This is a smaller payload than the LaRC reference concept, due to the reduced payload mass. It is estimated that this payload bay could accommodate up to 10 passengers. Two non-integral, multi-lobed LOX tanks hold the required oxidizer and are located adjacent to the payload bay. Note that this internal tank arrangement is different than the Langley reference. In the Langley configuration, the LOX tanks are located in the nose and tail sections of the vehicle. For the *ABLV-GT2*, with its inherently higher mixture ratio, placing the dense LOX tanks in the center of the fuselage will reduce the bending loads on the vehicle. Separate spherical tanks adjacent to the payload bay contain the OMS

propellants. Storage compartments for the main and nose landing gear are also present in the model. Small helium, gaseous hydrogen (GH2), and gaseous oxygen (GOX) tanks for the RCS are located in the nose and tail sections of the vehicle.

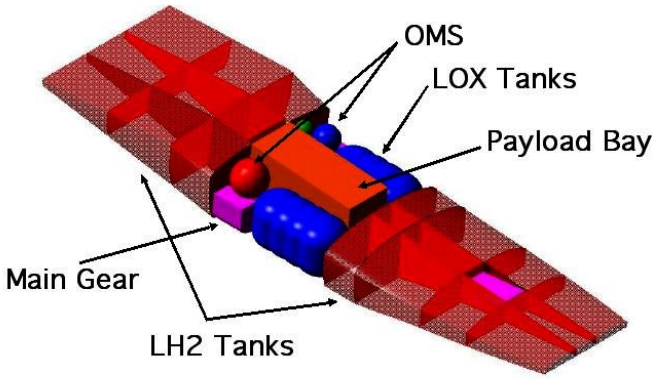

Figure 8.3 ABLV-GT2 Internal Fuselage CAD Model

One of the key outputs of the CAD discipline is the fraction of total internal fuselage volume that is occupied by ascent propellants (packaging efficiency factor, PEF). Since the tank configuration changes slightly with vehicle scale (payload volume is fixed), three different internal layouts were created — one each at three different vehicle length scales of 80%, 100%, and 120% of the 'as drawn' vehicle. A 1-D curve was created to allow interpolation, but no extrapolation, between the points on the curve. As an example, the as-drawn vehicle length of 190.5 feet tip-to-tail corresponds to a PEF of 70.8%.

An aerodynamic database consisting of tables with lift and drag coefficients were available from a previous study [71]. These values were obtained from the Aerodynamic Preliminary Analysis Software, or APAS [72]. At each Mach number and altitude combination of interest, analysis was performed over a range of angles-of-attack (AOA) from -10^{o} to 20^{o}, in 5^{o} increments. For all cases, the 'wings' were at zero incidence with respect to the vehicle centerline. These data tables were then provided to the trajectory program. Subsequent vehicle scaling was done photographically and the aerodynamic coefficients were assumed to remain constant during scaling. The aerodynamic analysis was therefore only required at the start of the design process. Note that in the force accounting system used, all forebody and upper surface pressures were included as aerodynamic drag and the propulsive forces used the 'cowl-to-tail' accounting system.

8.3 Mass Properties

A three-level spreadsheet model consisting of approximately 75 parametric mass estimating relationships (MER's) was created to estimate the weight and size of the converged *ABLV-GT2* vehicle. For example, MER's were included that estimate the wing weight based on surface area and wing loading, the fuselage MER was based on a smeared unit weight of 2.5 psf, and the landing gear weight was estimated as 2.5% of the GLOW (gross liftoff weight). A fairly aggressive installed engine thrust-to-weight ratio (T/W_e) of 30 was assumed. This number does not include the additional dry weight margin of 15%.

For the *ABLV-GT2*, a lightweight thermal protection system (TPS) called AFRSI, for Advanced Flexible Reusable Surface Insulation, is used for the leeward fuselage surface.

Since the exposed wing is constructed of a high-temperature titanium-aluminide (Ti-Al), large sections of the wing are designed to be hot structure. To avoid the complexities of active cooling present on the reference concept, an ultra-high temperature ceramic (UHTC) is employed on the small radius nose and wing leading edges. This material is being developed by NASA Ames Research Center and is capable of withstanding temperatures as high as 4,500° F [73].

For the forebody ramp TPS, a unique LaRC designed C/SiC tile with multi-layer insulation (MLI), platinum, and gold plating was used [69]. A structural unit weight of 1.59 psf, provided in a published paper for the reference concept, was assumed for these TPS coverage areas.

Given a mass ratio (MR or propellant mass fraction) and a mixture ratio (MixR) requirement from the trajectory optimization simulation, the spreadsheet was used to scale the vehicle up or down until the available MR and MixR matched that required from the trajectory.

8.4 Trajectory Simulation

The trajectory analysis was performed by the three degree-of-freedom version of the Program to Optimize Simulated Trajectories—POST. POST is a Lockheed Martin and NASA code that is widely used for trajectory optimization problems in advanced vehicle design [67]. It is a generalized, event-oriented code that numerically integrates the equations of motion of a flight vehicle given definitions of aerodynamic coefficients, propulsion system characteristics, and a weight model. Numerical optimization is used to satisfy

trajectory constraints and minimize a user-defined objective function. The objective for the *ABLV-GT2* trajectory is to maximize the final vehicle insertion weight (i.e. minimize propellant used).

The trajectory for the *ABLV-GT2* is constrained by a dynamic pressure boundary, changes in pitch rates that provide smooth AAR and rocket pull-ups, and by orbital termination criteria. The dynamic pressure boundary flown is 1,800 psf during ramjet and scramjet modes (Mach 3 to Mach 10). The q-boundary is constrained through implementation of a linear feedback control guidance scheme in which the dynamic pressure is held constant by controlling angle-of-attack [74]. For the baseline case above Mach 10, the vehicle begins to pull up and the q-boundary constraint is no longer enforced. During the pull-up, the rockets in the flowpath are reignited, the inlets remain open, and the engines operate in 'scram-rocket' mode. This transition to all-rocket mode is complete by approximately Mach 13, when the freestream dynamic pressure drops below 100 psf. The *ABLV-GT2* flies to an optimal MECO condition such that the apogee altitude is 100 nmi. at an inclination of 28.5°. A minimum perigee constraint of 30 nmi. is also specified. Throttled main engine rocket thrusters are used as the OMS to circularize the orbit at 100 nmi. and later deorbit the vehicle. The propellants for these maneuvers are stored in separate tanks from the main propellants. The baseline LOX/LH2 OMS is designed to deliver 400 fps of on-orbit ΔV.

8.5 Propulsion System Design

The *ABLV-GT2* main propulsion system uses two liquid oxygen and hydrogen ejector scramjet (ESJ) RBCC engines to inject the vehicle into a 30 nmi. by 100 nmi. interim transfer orbit. The vehicle consists of two engines, each with 8 struts (total of 16). The struts

provide 3-D flow compression, structural integrity, and housing for the rocket subsystems. Figure 8.4 shows this unique engine concept developed by Aerojet. More details on the performance capability and physical design for this type of arrangement can be found in Reference 28.

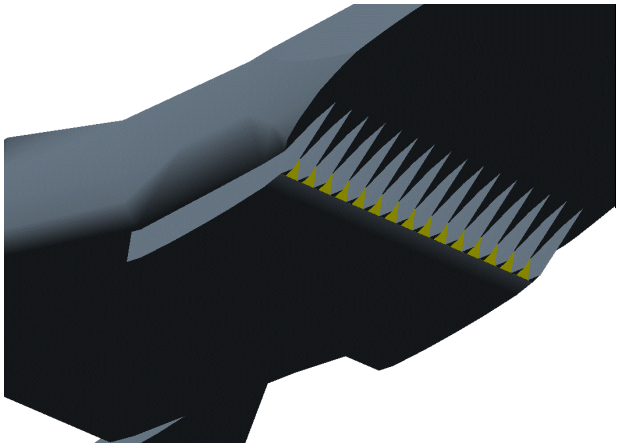

Figure 8.4 ABLV-GT2 RBCC Engine and Struts

The forebody design begins with a 6° compression ramp, followed by two additional ramps at 9° and 17°. At Mach 10, the bow shock will be focused on the cowl lip and the secondary shocks will be inside the inlet. The aftbody nozzle was shaped to provide a large expansion area for scramjet and all-rocket modes of operation, with an initial expansion angle of 20° decreasing to 5° at the tail tip. This corresponds to a theoretical nozzle expansion ratio of 6.6.

A LOX/LH2 rocket primary with a chamber pressure of 2,500 psi and mixture ratio of 6.5 was selected. The all-rocket performance calculations use the same rocket primary

subsystem from the AAR mode, but with the significantly higher expansion ratio (ε) of 400. The vacuum specific impulse for this system is 469 seconds.

SCCREAM provided the POST engine decks used during the vehicle closure process. Appendix F provides the propulsion system input variables values used for the analysis. The POST engine deck includes engine thrust, thrust coefficient (C_t), and I_{sp} for a range of altitudes and Mach numbers, for each of the 5 operating modes (AAR, RJ, SJ, SR, all-rocket). Due to numerical difficulties in the trajectory simulation, the ramjet, scramjet, and scram-rocket mode AOA data is at a single, averaged value for each mode, typically around 2^o for RJ and SJ modes and 5^o for SR mode. This value was adjusted during the vehicle closure to coincide with the actual flight AOA.

8.6 Results

Three different propulsion scenarios were examined for the *ABLV-GT2* vehicle. The first case used the CIM nozzle analysis. The second vehicle simulation used the new RSE-based aftbody performance thrust predictions. The third case incorporated both the new thrust and lift contributions from the nozzle. The lift values were added to the APAS aerodynamics deck using the same normalizing reference area convention. Unfortunately, POST does not currently support multiple lift and drag tables.

The 'closure' process used to obtain the results consisted of making an initial guess for the mass ratio and mixture ratio of the vehicle. These values were passed to the W&S discipline to determine the actual vehicle size for these assumed values. The parameters obtained from the W&S analysis (eg. GLOW, thrust required, aerodynamic reference area) were then sent

to the Propulsion discipline to size the engines and the Trajectory discipline to optimize the vehicle trajectory with the new size, weight, and engine performance. Between 10 and 15 iterations around the Propulsion – Trajectory - Weights loop, shown in the DSM in Figure 1.1, are required to obtain convergence. This entire process was repeated for both vehicles until the change in gross weight between successive iterations converged to within 0.1%. Table 8.1 provides a summary of the performance results for all three vehicle cases.

Table 8.1 ABLV-GT2 Performance Results

	CIM Nozzle	RSE Aftbody Nozzle No Propulsive Lift	RSE Aftbody Nozzle With Propulsive Lift
GLOW (lbs)	779,634	631,275	503,500
Dry (lbs)	137,425	114,575	91,865
Mass Ratio	4.879	4.684	4.573
Mixture Ratio	3.05	3.02	3.36
Length (ft)	157.4	144.7	128.4
Planform Loading (psf)	121.2	116.1	117.6
ΔV_{total} (ft/s)	39,150	38,180	34,850
ΔV_{drag} (ft/s)	12,400	11,350	8,025
Flight Time (s)	1,110	1,020	890

When the higher fidelity aftbody analysis results without the propulsive lift were incorporated into the design, the gross weight of the vehicle decreased by approximately 20% and the dry weight decreased by 17%. This decrease is mostly attributable to better engine performance at higher flight Mach numbers (i.e. SJ and SR modes). For the third case, both the gross and dry weight decreased another 20% when the additional aftbody lift effect was incorporated. The added lift reduced the vehicle angle of attack through much of

the trajectory, dramatically decreasing the drag losses. This effect can be measured in terms of the integrated drag losses term, ΔV_{drag}, provided in Table 8.1. Most of this benefit occurred in SR mode.

Figure 8.5, which shows the dynamic pressure (q_∞) versus Mach number profile from POST for all three vehicle cases. Up to the M_{tr} of 10, there are no significant differences in the q-paths. This is to be expected since POST was constrained to fly an 1,800 psf boundary from Mach 3 to Mach 10. At Mach 10, the vehicles begin their pull-up maneuver and transition to SR mode. Some small differences in the flight paths are evident here. POST is allowed to optimize the vehicle pitch rates during this mode and a required q-path is not defined. A significant increase in engine thrust is provided by this mode and the vehicle takes some time to adjust to this rapid change in acceleration. This is the cause for the initial increase in the q_∞-value from Mach 10 to Mach 11.

The effect of the propulsive lift on the vehicle can also be seen in the vehicle's angle of attack history. Figure 8.6 shows this profile from RJ mode through SR mode. Notice that for cases with no aftbody lift, the vehicles must fly at approximately 2° in RJ and 2.5° in SJ modes to maintain the specified q-path. When the propulsive lift is added on, the angle of attack is reduced to less than 1°. Similarly, in SR mode, the no-lift cases must pitch up to almost 8° during the pull-up maneuver, while the aftbody lift case only reaches 4° AOA.

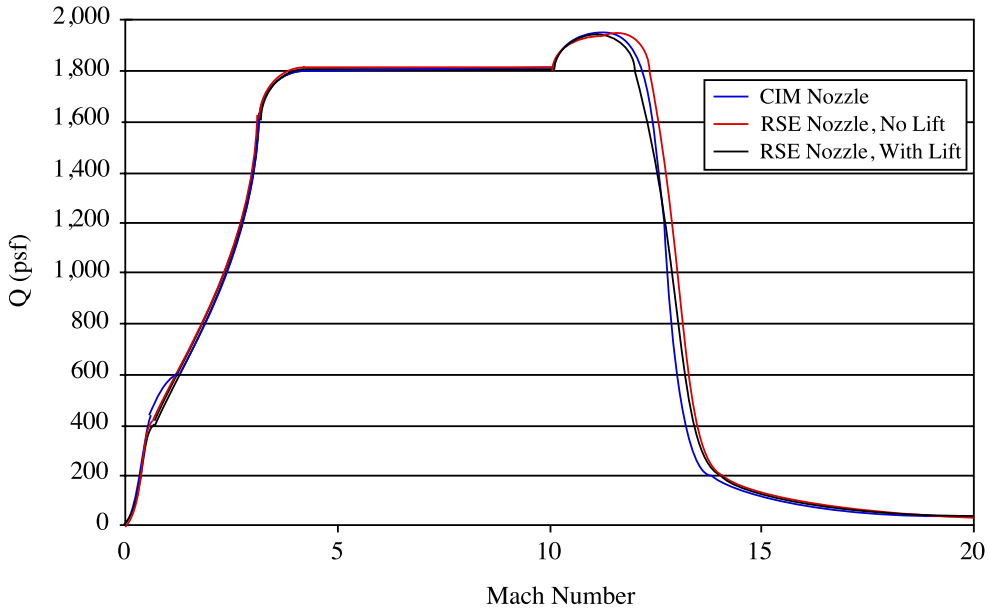

Figure 8.5 ABLV-GT2 Dynamic Pressure versus Mach Number Comparison

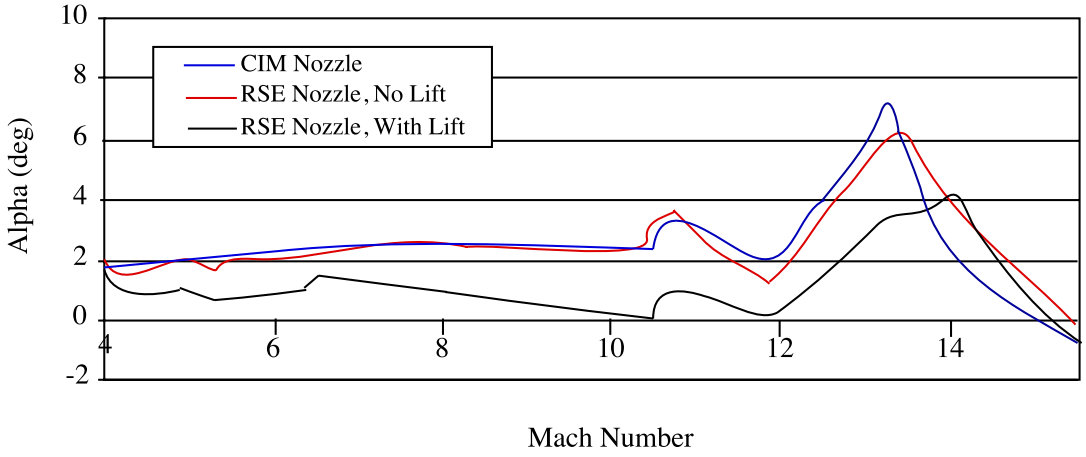

Figure 8.6 ABLV-GT2 Angle-of-Attack versus Mach Number Comparison

The last figure of interest is the vehicle altitude versus time results. This chart clearly shows the effect of the reduced drag and hence higher acceleration due to the propulsive lift. The

flight time with just the new propulsive thrust calculations was reduced by 90 seconds over the isentropic case. With the propulsive lift, an additional savings of 130 seconds is obtained.

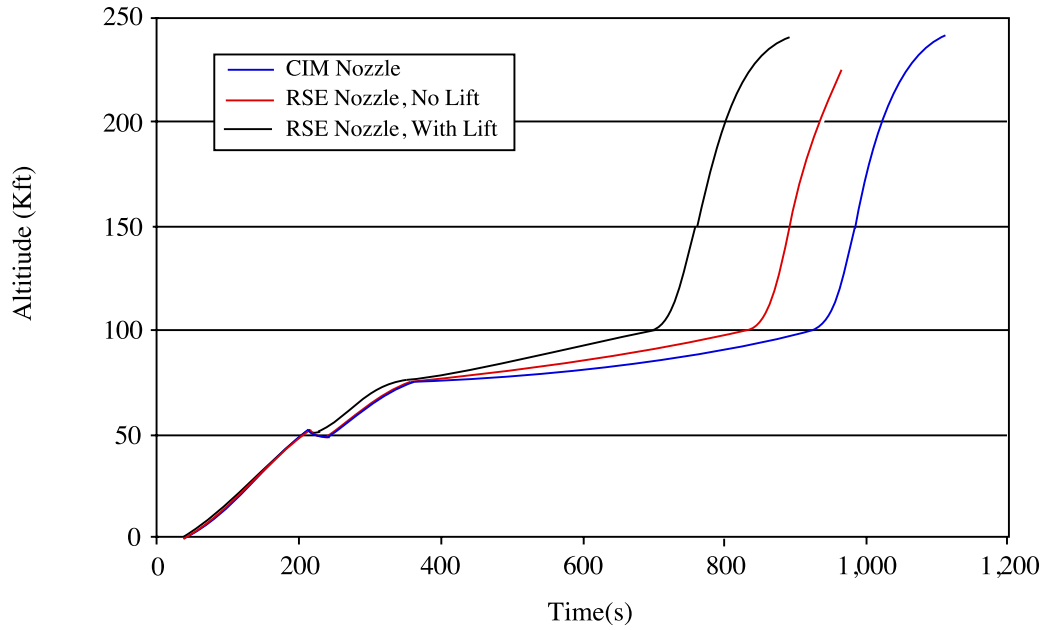

Figure 8.7 ABLV-GT2 Altitude versus Time Comparison

CHAPTER IX

CONCLUSIONS AND RECOMMENDATIONS

9.1 Conclusions

A technique for rapidly predicting aftbody nozzle performance for advanced hypersonic vehicles utilizing A/B and RBCC propulsion systems has been successfully implemented. This method involves a six step process that consists of:

1) Selection of an aftbody flow solver and identification of the relevant design variables.
2) Conducting a screening test to identify the most significant variables.
3) Designing an experiment array and performing multiple analysis runs for each experiment.
4) Obtaining the static pressures at select axial locations as the response values for each experiment in the array and generation of the RSE's.
5) Supplying the nozzle design parameter values to the RSE's to obtain the pressure ratio predictions. The predictions are then used to reconstruct the complete pressure distribution using a weighted least squares 5^{th} order polynomial fit.
6) The pressure ratio distribution is then numerically integrated to obtain the total aftbody axial force, normal force, and the pitch-plane moment.

Steps 1-4 require execution only once for a select range of variables and are the most time consuming part of the process. Steps 5 and 6 are then used repeatedly to provide nearly instantaneous aftbody performance results for a range of engine exhaust conditions, vehicle flight conditions, and nozzle geometries.

The results from the implementation of this technique and the performance modeling improvements made will be summarized next.

- A two-dimensional flow solver for the computation of inviscid, aftbody flowfields was created. Results from this code were verified with SEAGULL, a NASA-heritage perfect gas flowfield solver, for a Mach seven scramjet case. The two codes were shown to predict almost identical pressure distributions given the same nozzle geometry and initial flow conditions. Relative differences of less than 2% were obtained for both the integrated axial and normal forces.

- Two screening tests were conducted for nine aftbody design variables. Both tests indicated that the three geometric parameters (i.e. h/L, θ_1, and θ_2) along with the engine exit Mach number are the most significant factors affecting the aftbody pressure ratio (P/P_e) distribution. The results for the first test, based on variable ranges encountered for supersonic flight, identified the engine specific heat ratio (γ_e) and static pressure ratio (P_e/P_∞) as the factors with the smallest effects on the integrated pressure ratio distribution. The second test, based on variables ranges for hypersonic flight, identified the pressure ratio (P_e/P_∞) and density ratio (ρ_∞/ρ_e) as having negligible effects on the integrated pressure ratio distribution.

- Two sets of response surface equations were generated for use in either the supersonic or hypersonic flight regime. When combined with a Chi-Squared fitting algorithm, the results of the RSE's can be used to reconstruct the aftbody pressure distribution. The integrated axial and normal forces consistently provide results within +/-10% of the CPU intensive, two-dimensional Euler flow solutions.

- A design tool suitable for use in conceptual vehicle studies was created and various component models were compared with a number of industry standard analysis tools. This tool, called SCCREAM, is unique among all other propulsion analysis tools due to its quick execution speed, web-based user interface, detailed combustor model, aftbody nozzle analysis, and POST engine deck generation.

- The resulting response surface equations for the aftbody performance prediction were incorporated into SCCREAM and then demonstrated for a 3rd generation launch vehicle concept named the *ABLV-GT2*. With the new thrust predictions, the vehicle size in terms of gross weight was shown to decrease by approximately 20% in comparison with the CIM nozzle analysis. When the propulsive lift was added in, the vehicle's gross and dry weight were shown to decrease by an additional 20%. This decrease was mostly attributable to changes in the vehicle angle-of-attack during flight and the associated drag reduction.

Recall the pressure distributions provided in Figure 1.1 that compared the CFD solver predictions with the CIM nozzle case for a 10° SERN design at Mach 10. The RSE equation predictions can now be added to this figure to demonstrate the recent improvements made. The updated figure is shown as Figure 9.1. Note the significant improvement in matching the pressure distribution achieved by the RSE predictions. When

the integrated effects are determined for the RSE, agreement within 5% of the CFD solution for the forces and 4% for the moment arm is obtained. Recall again that the CIM results overpredicted the forces by 24%.

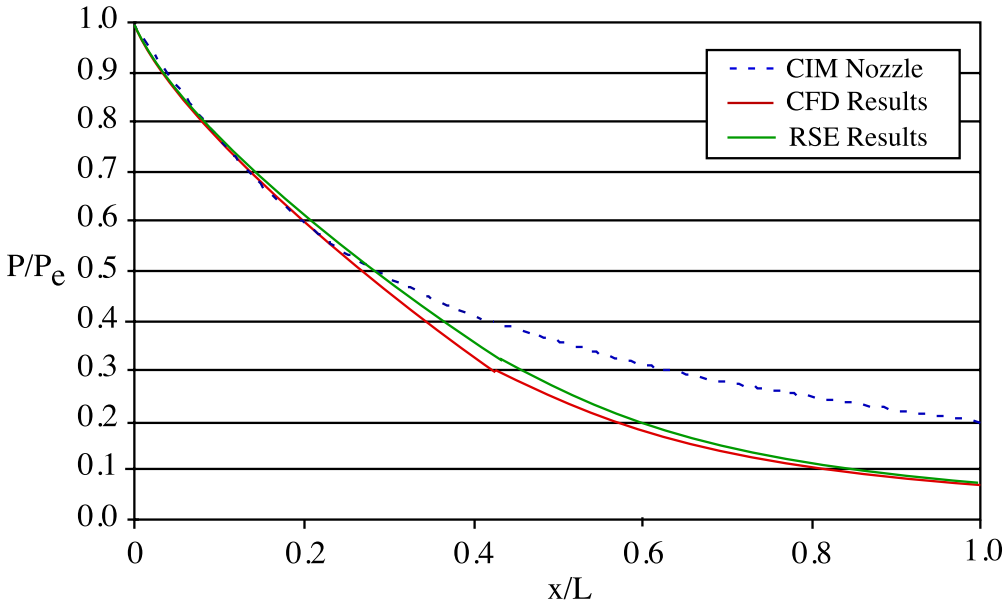

Figure 9.1 Updated *Figure 1.2* With RSE Predicted Distribution

The objective of this work was to enable a variety of new capabilities for the design analyst in the conceptual design environment. Three of the new capabilities identified were the ability to account for propulsive lift, optimize the vehicle aftbody nozzle shape and engine flowpath, and perform trajectory simulations that incorporate the vehicle's pitch-plane moment. These capabilities have all been enabled with the successful implementation of the rapid prediction method outlined. The first new capability was even demonstrated with the sample vehicle application (i.e. the ABLV-GT2). Improvements in accuracy and the ability to locate the optimal system configuration will be required to advance the current 'state of the art' in hypersonic launch vehicle design. With numerous launch vehicle studies continuing to yield infeasible and economically unviable configurations, the additional

parameters now available for optimization in the design process will hopefully yield a vehicle configuration that will eventually allow affordable and routine access to space.

9.2 Recommendations and Comments

The following are some observations from the work completed and suggestions for maximizing the usage of the propulsion system data now available.

- It is postulated that the methodology outlined in Figure 1.1 can also be utilized in a preliminary rather than conceptual vehicle design environment. Once a promising vehicle has been identified in the conceptual design phase and selected for advancement to preliminary design work, a new set of RSE's can be established that is more specific to the vehicle being considered. By tightening the parameter bounds or possibly eliminating some geometric parameters, increased levels of accuracy will be obtained.

- The present methodology forms a framework for future implementations like adding viscous effects and shear layers. Since the stated methodology is independent of the flowfield solver and its capabilites, higher level CFD analysis methods could be used for generating the responses. A thermally perfect gas, chemically reacting exhaust, or a Navier Stokes flow solver that accounts for the viscous effects on the aftbody, could be used in place of the inviscid Euler solver that was created and used for generating the current predictions.

- Utilizing the pressure distribution obtained from the RSE's and making some additional assumptions, a Mach number distribution along the nozzle surface can also be obtained. Similarly, a static temperature distribution and velocity along the surface can also be obtained. Using these fluid parameters, it would then be possible to incorporate a boundary layer routine for estimating the frictional forces on the nozzle surface. Additionally, the approximate temperature distribution obtained could be used for thermal protection system sizing on the aftbody structure.

- Further improvements in accuracy could possibly be obtained by using a different meta-model. While the RSE's where selected as the meta-model of choice due to their ease of use and computation efficiency, a different model type, like a neural network, could allow for additional variables and fewer experiments. The drawback to this sort of model will be the overhead associated with training and supporting such a system.

- While the current work used predictions for a 2-D nozzle flowfield, the method could be applied to results for a 3-D flowfield. In a 3-D flowfield, the engine has a finite width and the aftbody pressures will be reduced due to lateral relief along the edges of the nozzle. In addition to requiring a 3-D flow solver model, new geometic parameters such as the engine width-to-length ratio and the vehicle width to engine width ratio will also need to be incorporated in the meta-model generation.

- With the established set of RSE's, it is now possible to determine all of the pitch-plane moments on the vehicle during most of the atmospheric flight. To complete the toolset needed for trajectory simulations with the pitch-plane moment and dynamic stability analysis, variations in the vehicle's center of gravity (C.G.) during the trajectory must be determined. This will require 'real-time' analysis, especially for RBCC vehicle

configurations. The C.G. will be dependent on the engines burn time in each mode and the types of propellant consumed in a particular mode. An optimization algorithm could be devised to obtain the optimal balance between tank location, engine mode operation, and control surface sizing.

APPENDIX A

CHEMICAL EQUILIBRIUM DEFINITIONS AND COEFFICIENT MATRICES

Atoms (i's):

i=0	'O' atom
i=1	'H' atom
i=2	'C' atom
i=3	'N' atom
i=4	'Ar' atom

Molecules (j's):

j=0	'O_2'	j=7	'CO_2'
j=1	'H_2'	j=8	'CO'
j=2	'O'	j=9	'N_2'
j=3	'H'	j=10	'Ar'
j=4	'OH'	j=11	'NO'
j=5	'H_2O'	j=11	'N'

N_j: number moles of species i
N: total number of moles
$b_{o,i}$: initial number atoms in reactants

$a_{i,j}$: atoms of i in species j

$a_{i,j}$	*0*	*1*	*2*	*3*	*4*	*5*	*6*	*7*	*8*	*9*	*10*	*11*
0	2	0	1	0	1	1	2	1	0	0	1	0
1	0	2	0	1	1	2	0	0	0	0	0	0
2	0	0	0	0	0	0	1	1	0	0	0	0
3	0	0	0	0	0	0	0	0	2	0	1	1
4	0	0	0	0	0	0	0	0	0	1	0	0

$$\Delta \ln N_j = -\frac{\mu_i}{RT} + \sum_{i=0}^{4} a_{i,j} b_i + \Delta \ln N$$

where:

$$\mu_{i,j} = g^{o}{}_{i,T} + RT \ln\left(\frac{N_i}{N}\right) + RT \ln P$$

R universal gas constant
T adiabatic flame temperature (specified)
P reaction pressure (specified)

APPENDIX B

SCREENING TEST EXPERIMENT AND RESULTS

Supersonic Set

Run #	M_e	γ_e	ρ_∞/ρ_e	Alt	h/L	θ_1	θ_2	M_∞	P_e/P_∞	P*d*Ay	P*d*Ax	S
1	3	1.4	5	90	0.15	25	10	6	100	0.15175	0.43480	0.43971
2	1.2	1.4	0.1	90	0.15	25	0	2.5	10	0.06873	0.23774	0.40659
3	1.2	1.2	5	40	0.15	25	10	2.5	10	0.07802	0.20475	0.32399
4	3	1.2	0.1	90	0.025	25	10	6	10	0.05603	0.14955	0.34675
5	1.2	1.4	0.1	40	0.15	10	10	6	100	0.04080	0.23136	0.24573
6	1.2	1.2	5	40	0.025	25	0	6	100	0.02122	0.06237	0.28931
7	1.2	1.2	0.1	90	0.025	10	10	2.5	100	0.00983	0.05576	0.11372
8	3	1.2	0.1	40	0.15	10	0	6	10	0.06878	0.65103	0.42681
9	3	1.4	0.1	40	0.025	25	0	2.5	100	0.03484	0.09968	0.27038
10	3	1.4	5	40	0.025	10	10	2.5	10	0.02611	0.14806	0.23491
11	1.2	1.4	5	90	0.025	10	0	6	10	0.01644	0.13902	0.35493
12	3	1.2	5	90	0.15	10	0	2.5	100	0.06615	0.61837	0.41967

Hypersonic Set

Run #	M_e	γ_e	ρ_∞/ρ_e	Alt	h/L	θ_1	θ_2	M_∞	P_e/P_∞	P*d*Ay	P*d*Ax	S
1	4	1.4	3	120	0.15	25	10	12	100	0.16931	0.49799	0.47305
2	1.2	1.4	0.1	120	0.15	25	0	6	5	0.07807	0.28331	0.43253
3	1.2	1.2	3	70	0.15	25	10	6	5	0.08667	0.23735	0.38108
4	4	1.2	0.1	120	0.025	25	10	12	5	0.10238	0.29136	0.43096
5	1.2	1.4	0.1	70	0.15	10	10	12	100	0.04119	0.23359	0.24844
6	1.2	1.2	3	70	0.025	25	0	12	100	0.03704	0.11592	0.33443
7	1.2	1.2	0.1	120	0.025	10	10	6	100	0.01785	0.10121	0.16544
8	4	1.2	0.1	70	0.15	10	0	12	5	0.07848	0.82958	0.49131
9	4	1.4	0.1	70	0.025	25	0	6	100	0.07728	0.28039	0.43211
10	4	1.4	3	70	0.025	10	10	6	5	0.05268	0.29879	0.31624
11	1.2	1.4	3	120	0.025	10	0	12	5	0.02334	0.20271	0.37282
12	4	1.2	3	120	0.15	10	0	6	100	0.07508	0.75897	0.46552

APPENDIX C

CENTRAL COMPOSITE EXPERIMENT DESIGNS

Supersonic Set

Run #	M_e	ρ_e/ρ_∞	Alt	h/L	θ_1	θ_2	M_∞
1	1.2	0.1	40	0.05	10	0	2.5
2	1.2	0.1	40	0.05	10	0	6
3	1.2	0.1	40	0.05	10	10	2.5
4	1.2	0.1	40	0.05	10	10	6
5	1.2	0.1	40	0.05	25	0	2.5
6	1.2	0.1	40	0.05	25	0	6
7	1.2	0.1	40	0.05	25	10	2.5
8	1.2	0.1	40	0.05	25	10	6
9	1.2	0.1	40	0.15	10	0	2.5
10	1.2	0.1	40	0.15	10	0	6
11	1.2	0.1	40	0.15	10	10	2.5
12	1.2	0.1	40	0.15	10	10	6
13	1.2	0.1	40	0.15	25	0	2.5
14	1.2	0.1	40	0.15	25	0	6
15	1.2	0.1	40	0.15	25	10	2.5
16	1.2	0.1	40	0.15	25	10	6
17	1.2	0.1	90	0.05	10	0	2.5
18	1.2	0.1	90	0.05	10	0	6
19	1.2	0.1	90	0.05	10	10	2.5
20	1.2	0.1	90	0.05	10	10	6
21	1.2	0.1	90	0.05	25	0	2.5
22	1.2	0.1	90	0.05	25	0	6
23	1.2	0.1	90	0.05	25	10	2.5
24	1.2	0.1	90	0.05	25	10	6
25	1.2	0.1	90	0.15	10	0	2.5
26	1.2	0.1	90	0.15	10	0	6
27	1.2	0.1	90	0.15	10	10	2.5

28	1.2	0.1	90	0.15	10	10	6
29	1.2	0.1	90	0.15	25	0	2.5
30	1.2	0.1	90	0.15	25	0	6
31	1.2	0.1	90	0.15	25	10	2.5
32	1.2	0.1	90	0.15	25	10	6
33	1.2	5	40	0.05	10	0	2.5
34	1.2	5	40	0.05	10	0	6
35	1.2	5	40	0.05	10	10	2.5
36	1.2	5	40	0.05	10	10	6
37	1.2	5	40	0.05	25	0	2.5
38	1.2	5	40	0.05	25	0	6
39	1.2	5	40	0.05	25	10	2.5
40	1.2	5	40	0.05	25	10	6
41	1.2	5	40	0.15	10	0	2.5
42	1.2	5	40	0.15	10	0	6
43	1.2	5	40	0.15	10	10	2.5
44	1.2	5	40	0.15	10	10	6
45	1.2	5	40	0.15	25	0	2.5
46	1.2	5	40	0.15	25	0	6
47	1.2	5	40	0.15	25	10	2.5
48	1.2	5	40	0.15	25	10	6
49	1.2	5	90	0.05	10	0	2.5
50	1.2	5	90	0.05	10	0	6
51	1.2	5	90	0.05	10	10	2.5
52	1.2	5	90	0.05	10	10	6
53	1.2	5	90	0.05	25	0	2.5
54	1.2	5	90	0.05	25	0	6
55	1.2	5	90	0.05	25	10	2.5
56	1.2	5	90	0.05	25	10	6
57	1.2	5	90	0.15	10	0	2.5
58	1.2	5	90	0.15	10	0	6
59	1.2	5	90	0.15	10	10	2.5
60	1.2	5	90	0.15	10	10	6
61	1.2	5	90	0.15	25	0	2.5
62	1.2	5	90	0.15	25	0	6
63	1.2	5	90	0.15	25	10	2.5
64	1.2	5	90	0.15	25	10	6
65	3	0.1	40	0.05	10	0	2.5
66	3	0.1	40	0.05	10	0	6
67	3	0.1	40	0.05	10	10	2.5
68	3	0.1	40	0.05	10	10	6
69	3	0.1	40	0.05	25	0	2.5
70	3	0.1	40	0.05	25	0	6
71	3	0.1	40	0.05	25	10	2.5
72	3	0.1	40	0.05	25	10	6
73	3	0.1	40	0.15	10	0	2.5
74	3	0.1	40	0.15	10	0	6
75	3	0.1	40	0.15	10	10	2.5
76	3	0.1	40	0.15	10	10	6
77	3	0.1	40	0.15	25	0	2.5
78	3	0.1	40	0.15	25	0	6
79	3	0.1	40	0.15	25	10	2.5
80	3	0.1	40	0.15	25	10	6
81	3	0.1	90	0.05	10	0	2.5
82	3	0.1	90	0.05	10	0	6

83	3	0.1	90	0.05	10	10	2.5
84	3	0.1	90	0.05	10	10	6
85	3	0.1	90	0.05	25	0	2.5
86	3	0.1	90	0.05	25	0	6
87	3	0.1	90	0.05	25	10	2.5
88	3	0.1	90	0.05	25	10	6
89	3	0.1	90	0.15	10	0	2.5
90	3	0.1	90	0.15	10	0	6
91	3	0.1	90	0.15	10	10	2.5
92	3	0.1	90	0.15	10	10	6
93	3	0.1	90	0.15	25	0	2.5
94	3	0.1	90	0.15	25	0	6
95	3	0.1	90	0.15	25	10	2.5
96	3	0.1	90	0.15	25	10	6
97	3	5	40	0.05	10	0	2.5
98	3	5	40	0.05	10	0	6
99	3	5	40	0.05	10	10	2.5
100	3	5	40	0.05	10	10	6
101	3	5	40	0.05	25	0	2.5
102	3	5	40	0.05	25	0	6
103	3	5	40	0.05	25	10	2.5
104	3	5	40	0.05	25	10	6
105	3	5	40	0.15	10	0	2.5
106	3	5	40	0.15	10	0	6
107	3	5	40	0.15	10	10	2.5
108	3	5	40	0.15	10	10	6
109	3	5	40	0.15	25	0	2.5
110	3	5	40	0.15	25	0	6
111	3	5	40	0.15	25	10	2.5
112	3	5	40	0.15	25	10	6
113	3	5	90	0.05	10	0	2.5
114	3	5	90	0.05	10	0	6
115	3	5	90	0.05	10	10	2.5
116	3	5	90	0.05	10	10	6
117	3	5	90	0.05	25	0	2.5
118	3	5	90	0.05	25	0	6
119	3	5	90	0.05	25	10	2.5
120	3	5	90	0.05	25	10	6
121	3	5	90	0.15	10	0	2.5
122	3	5	90	0.15	10	0	6
123	3	5	90	0.15	10	10	2.5
124	3	5	90	0.15	10	10	6
125	3	5	90	0.15	25	0	2.5
126	3	5	90	0.15	25	0	6
127	3	5	90	0.15	25	10	2.5
128	3	5	90	0.15	25	10	6
129	1.2	2.55	65	0.1	17.5	5	4.25
130	3	2.55	65	0.1	17.5	5	4.25
131	2.1	0.1	65	0.1	17.5	5	4.25
132	2.1	5	65	0.1	17.5	5	4.25
133	2.1	2.55	40	0.1	17.5	5	4.25
134	2.1	2.55	90	0.1	17.5	5	4.25
135	2.1	2.55	65	0.05	17.5	5	4.25
136	2.1	2.55	65	0.15	17.5	5	4.25
137	2.1	2.55	65	0.1	10	5	4.25

138	2.1	2.55	65	0.1	25	5	4.25
139	2.1	2.55	65	0.1	17.5	0	4.25
140	2.1	2.55	65	0.1	17.5	10	4.25
141	2.1	2.55	65	0.1	17.5	5	2.5
142	2.1	2.55	65	0.1	17.5	5	6
143	2.1	2.55	65	0.1	17.5	5	4.25

Hypersonic Set

Run #	M_e	γ_e	Alt	h/L	θ_1	θ_2	M_∞
1	1.2	1.2	70	0.05	10	0	6
2	1.2	1.2	70	0.05	10	0	12
3	1.2	1.2	70	0.05	10	10	6
4	1.2	1.2	70	0.05	10	10	12
5	1.2	1.2	70	0.05	25	0	6
6	1.2	1.2	70	0.05	25	0	12
7	1.2	1.2	70	0.05	25	10	6
8	1.2	1.2	70	0.05	25	10	12
9	1.2	1.2	70	0.15	10	0	6
10	1.2	1.2	70	0.15	10	0	12
11	1.2	1.2	70	0.15	10	10	6
12	1.2	1.2	70	0.15	10	10	12
13	1.2	1.2	70	0.15	25	0	6
14	1.2	1.2	70	0.15	25	0	12
15	1.2	1.2	70	0.15	25	10	6
16	1.2	1.2	70	0.15	25	10	12
17	1.2	1.2	120	0.05	10	0	6
18	1.2	1.2	120	0.05	10	0	12
19	1.2	1.2	120	0.05	10	10	6
20	1.2	1.2	120	0.05	10	10	12
21	1.2	1.2	120	0.05	25	0	6
22	1.2	1.2	120	0.05	25	0	12
23	1.2	1.2	120	0.05	25	10	6
24	1.2	1.2	120	0.05	25	10	12
25	1.2	1.2	120	0.15	10	0	6
26	1.2	1.2	120	0.15	10	0	12
27	1.2	1.2	120	0.15	10	10	6
28	1.2	1.2	120	0.15	10	10	12
29	1.2	1.2	120	0.15	25	0	6
30	1.2	1.2	120	0.15	25	0	12
31	1.2	1.2	120	0.15	25	10	6
32	1.2	1.2	120	0.15	25	10	12
33	1.2	1.4	70	0.05	10	0	6
34	1.2	1.4	70	0.05	10	0	12
35	1.2	1.4	70	0.05	10	10	6
36	1.2	1.4	70	0.05	10	10	12
37	1.2	1.4	70	0.05	25	0	6
38	1.2	1.4	70	0.05	25	0	12
39	1.2	1.4	70	0.05	25	10	6
40	1.2	1.4	70	0.05	25	10	12

41	1.2	1.4	70	0.15	10	0	6
42	1.2	1.4	70	0.15	10	0	12
43	1.2	1.4	70	0.15	10	10	6
44	1.2	1.4	70	0.15	10	10	12
45	1.2	1.4	70	0.15	25	0	6
46	1.2	1.4	70	0.15	25	0	12
47	1.2	1.4	70	0.15	25	10	6
48	1.2	1.4	70	0.15	25	10	12
49	1.2	1.4	120	0.05	10	0	6
50	1.2	1.4	120	0.05	10	0	12
51	1.2	1.4	120	0.05	10	10	6
52	1.2	1.4	120	0.05	10	10	12
53	1.2	1.4	120	0.05	25	0	6
54	1.2	1.4	120	0.05	25	0	12
55	1.2	1.4	120	0.05	25	10	6
56	1.2	1.4	120	0.05	25	10	12
57	1.2	1.4	120	0.15	10	0	6
58	1.2	1.4	120	0.15	10	0	12
59	1.2	1.4	120	0.15	10	10	6
60	1.2	1.4	120	0.15	10	10	12
61	1.2	1.4	120	0.15	25	0	6
62	1.2	1.4	120	0.15	25	0	12
63	1.2	1.4	120	0.15	25	10	6
64	1.2	1.4	120	0.15	25	10	12
65	4	1.2	70	0.05	10	0	6
66	4	1.2	70	0.05	10	0	12
67	4	1.2	70	0.05	10	10	6
68	4	1.2	70	0.05	10	10	12
69	4	1.2	70	0.05	25	0	6
70	4	1.2	70	0.05	25	0	12
71	4	1.2	70	0.05	25	10	6
72	4	1.2	70	0.05	25	10	12
73	4	1.2	70	0.15	10	0	6
74	4	1.2	70	0.15	10	0	12
75	4	1.2	70	0.15	10	10	6
76	4	1.2	70	0.15	10	10	12
77	4	1.2	70	0.15	25	0	6
78	4	1.2	70	0.15	25	0	12
79	4	1.2	70	0.15	25	10	6
80	4	1.2	70	0.15	25	10	12
81	4	1.2	120	0.05	10	0	6
82	4	1.2	120	0.05	10	0	12
83	4	1.2	120	0.05	10	10	6
84	4	1.2	120	0.05	10	10	12
85	4	1.2	120	0.05	25	0	6
86	4	1.2	120	0.05	25	0	12
87	4	1.2	120	0.05	25	10	6
88	4	1.2	120	0.05	25	10	12
89	4	1.2	120	0.15	10	0	6
90	4	1.2	120	0.15	10	0	12
91	4	1.2	120	0.15	10	10	6
92	4	1.2	120	0.15	10	10	12
93	4	1.2	120	0.15	25	0	6
94	4	1.2	120	0.15	25	0	12
95	4	1.2	120	0.15	25	10	6

96	4	1.2	120	0.15	25	10	12
97	4	1.4	70	0.05	10	0	6
98	4	1.4	70	0.05	10	0	12
99	4	1.4	70	0.05	10	10	6
100	4	1.4	70	0.05	10	10	12
101	4	1.4	70	0.05	25	0	6
102	4	1.4	70	0.05	25	0	12
103	4	1.4	70	0.05	25	10	6
104	4	1.4	70	0.05	25	10	12
105	4	1.4	70	0.15	10	0	6
106	4	1.4	70	0.15	10	0	12
107	4	1.4	70	0.15	10	10	6
108	4	1.4	70	0.15	10	10	12
109	4	1.4	70	0.15	25	0	6
110	4	1.4	70	0.15	25	0	12
111	4	1.4	70	0.15	25	10	6
112	4	1.4	70	0.15	25	10	12
113	4	1.4	120	0.05	10	0	6
114	4	1.4	120	0.05	10	0	12
115	4	1.4	120	0.05	10	10	6
116	4	1.4	120	0.05	10	10	12
117	4	1.4	120	0.05	25	0	6
118	4	1.4	120	0.05	25	0	12
119	4	1.4	120	0.05	25	10	6
120	4	1.4	120	0.05	25	10	12
121	4	1.4	120	0.15	10	0	6
122	4	1.4	120	0.15	10	0	12
123	4	1.4	120	0.15	10	10	6
124	4	1.4	120	0.15	10	10	12
125	4	1.4	120	0.15	25	0	6
126	4	1.4	120	0.15	25	0	12
127	4	1.4	120	0.15	25	10	6
128	4	1.4	120	0.15	25	10	12
129	1.2	1.3	95	0.1	17.5	5	9
130	4	1.3	95	0.1	17.5	5	9
131	2.6	1.2	95	0.1	17.5	5	9
132	2.6	1.4	95	0.1	17.5	5	9
133	2.6	1.3	70	0.1	17.5	5	9
134	2.6	1.3	120	0.1	17.5	5	9
135	2.6	1.3	95	0.05	17.5	5	9
136	2.6	1.3	95	0.15	17.5	5	9
137	2.6	1.3	95	0.1	10	5	9
138	2.6	1.3	95	0.1	25	5	9
139	2.6	1.3	95	0.1	17.5	0	9
140	2.6	1.3	95	0.1	17.5	10	9
141	2.6	1.3	95	0.1	17.5	5	6
142	2.6	1.3	95	0.1	17.5	5	12
143	2.6	1.3	95	0.1	17.5	5	9

APPENDIX D

CENTRAL COMPOSITE EXPERIMENT RESULTS

Supersonic Set

Run #	$x/L)_{0.1}$	$x/L)_{0.2}$	$x/L)_{0.6}$	$x/L)_{0.9}$	$x/L)_{1.0}$
1	0.291537	0.120996	0.022447	0.017728	0.017566
2	0.290297	0.11912	0.043988	0.047687	0.049177
3	0.296512	0.123871	0.017551	0.010409	0.009485
4	0.274162	0.106053	0.029278	0.02564	0.024865
5	0.211408	0.102037	0.02429	0.025367	0.026344
6	0.201021	0.094488	0.026913	0.03827	0.042804
7	0.198409	0.089685	0.016265	0.014625	0.014468
8	0.201035	0.092792	0.018714	0.021518	0.022783
9	0.671225	0.433169	0.123935	0.072042	0.064444
10	0.684370	0.448065	0.126348	0.077824	0.073305
11	0.656671	0.407818	0.098953	0.050793	0.043493
12	0.665306	0.414289	0.096943	0.050848	0.04442
13	0.450397	0.318195	0.137981	0.095339	0.089927
14	0.448865	0.314754	0.132234	0.096552	0.09320
15	0.442767	0.298448	0.112464	0.068494	0.061722
16	0.437443	0.295615	0.105733	0.069686	0.064399
17	0.291537	0.120996	0.022447	0.017728	0.017566
18	0.290297	0.119120	0.043988	0.047687	0.049177
19	0.296512	0.123871	0.017551	0.010409	0.009485
20	0.274162	0.106053	0.029278	0.02564	0.024865
21	0.211408	0.102037	0.02429	0.025367	0.026344
22	0.201021	0.094488	0.026913	0.03827	0.042804
23	0.198409	0.089685	0.016265	0.014625	0.014468
24	0.201035	0.092792	0.018714	0.021518	0.022783

25	0.671225	0.433169	0.123935	0.072042	0.064444
26	0.68437	0.448065	0.126348	0.077824	0.073305
27	0.656671	0.407818	0.098953	0.050793	0.043493
28	0.665306	0.414289	0.096943	0.050848	0.04442
29	0.450397	0.318195	0.137981	0.095339	0.089927
30	0.448865	0.314754	0.132234	0.096552	0.0932
31	0.443691	0.29818	0.112262	0.067606	0.06072
32	0.437443	0.295615	0.105733	0.069686	0.064399
33	0.305272	0.136388	0.049112	0.049509	0.051169
34	0.333156	0.154144	0.078606	0.075095	0.075359
35	0.318668	0.141110	0.042604	0.034577	0.033614
36	0.314397	0.136635	0.055840	0.044588	0.042680
37	0.225150	0.108533	0.053909	0.063335	0.068337
38	0.219846	0.106498	0.062820	0.072797	0.077548
39	0.214790	0.097802	0.038605	0.038542	0.039817
40	0.219679	0.101434	0.045878	0.045199	0.046248
41	0.681438	0.460504	0.142284	0.093987	0.089114
42	0.690637	0.468435	0.148158	0.116065	0.115236
43	0.662412	0.424354	0.108895	0.060668	0.054331
44	0.673947	0.443457	0.118127	0.075252	0.070287
45	0.458754	0.328160	0.142170	0.117782	0.118344
46	0.456441	0.336465	0.147927	0.135596	0.139929
47	0.447696	0.301921	0.107720	0.077226	0.074052
48	0.443859	0.315832	0.115952	0.089738	0.088197
49	0.333243	0.155166	0.059155	0.058424	0.059744
50	0.333156	0.154144	0.078606	0.075095	0.075359
51	0.318668	0.141110	0.042604	0.034576	0.033611
52	0.314397	0.136635	0.055840	0.044588	0.042680
53	0.225151	0.108533	0.053908	0.063334	0.068336
54	0.219846	0.106498	0.062820	0.072797	0.077548
55	0.214790	0.097802	0.038605	0.038541	0.039814
56	0.219679	0.101434	0.045878	0.045199	0.046248
57	0.681438	0.460504	0.142284	0.093987	0.089114
58	0.690637	0.468435	0.148158	0.116065	0.115236
59	0.662412	0.424354	0.108895	0.060668	0.054331
60	0.673947	0.443457	0.118127	0.075252	0.070287
61	0.458754	0.328160	0.142171	0.117783	0.118346
62	0.456444	0.336465	0.147927	0.135596	0.139929
63	0.447696	0.301921	0.107720	0.077226	0.074052
64	0.443859	0.315832	0.115952	0.089738	0.088197
65	0.654049	0.438700	0.102386	0.055969	0.052891
66	0.656577	0.451531	0.116073	0.059926	0.055233
67	0.641126	0.418170	0.087755	0.034020	0.027360
68	0.633971	0.396066	0.076254	0.028896	0.023724
69	0.405859	0.272461	0.118396	0.110839	0.113821
70	0.397148	0.271800	0.117303	0.111109	0.114314
71	0.392812	0.246851	0.078999	0.061456	0.060146
72	0.381147	0.243868	0.087525	0.067779	0.066204
73	0.868778	0.800381	0.541831	0.356372	0.322937
74	0.866579	0.796067	0.531283	0.351437	0.318467
75	0.843618	0.726470	0.394933	0.231425	0.203639
76	0.844779	0.727786	0.397607	0.237666	0.209649
77	0.686252	0.583940	0.506261	0.463676	0.455418
78	0.689649	0.591536	0.523150	0.487268	0.477135
79	0.665519	0.529789	0.360143	0.306417	0.293153

80	0.670035	0.529008	0.351514	0.287087	0.271334
81	0.657441	0.437073	0.095785	0.053353	0.051334
82	0.661492	0.451630	0.102067	0.054769	0.053288
83	0.641126	0.418170	0.087755	0.03402	0.02736
84	0.637031	0.401464	0.074858	0.028591	0.023342
85	0.405859	0.272461	0.118396	0.110839	0.113821
86	0.397148	0.271800	0.117303	0.111109	0.114314
87	0.392812	0.246851	0.078999	0.061456	0.060146
88	0.381147	0.243868	0.087525	0.067779	0.066204
89	0.868778	0.800381	0.541831	0.356372	0.322937
90	0.872900	0.806101	0.564476	0.369803	0.336028
91	0.843618	0.726470	0.394933	0.231425	0.203639
92	0.841634	0.724275	0.39866	0.226389	0.198089
93	0.686447	0.578043	0.49498	0.465696	0.461496
94	0.689649	0.591536	0.52315	0.487268	0.477135
95	0.665519	0.529789	0.360143	0.306417	0.293153
96	0.663895	0.531022	0.364847	0.315627	0.301926
97	0.662481	0.455268	0.130691	0.087545	0.083488
98	0.667288	0.477152	0.127511	0.097198	0.096378
99	0.644848	0.414256	0.092008	0.047939	0.042238
100	0.642967	0.424205	0.083979	0.04779	0.043335
101	0.416115	0.284669	0.141887	0.138511	0.144507
102	0.406846	0.303178	0.164922	0.170140	0.181075
103	0.396459	0.262003	0.091511	0.077000	0.076514
104	0.381162	0.256007	0.107077	0.087276	0.086811
105	0.865632	0.793932	0.539641	0.361153	0.329814
106	0.868778	0.800439	0.562391	0.36799	0.335588
107	0.845579	0.728879	0.408959	0.243829	0.214179
108	0.843618	0.726500	0.40902	0.233521	0.203513
109	0.685182	0.576025	0.498943	0.478627	0.475886
110	0.688044	0.588539	0.539875	0.523312	0.515682
111	0.668661	0.529693	0.361344	0.318194	0.303908
112	0.664564	0.530669	0.370532	0.337358	0.322654
113	0.662666	0.457294	0.130929	0.08822	0.083994
114	0.667288	0.477152	0.127511	0.097198	0.096378
115	0.644846	0.414253	0.092007	0.047939	0.042238
116	0.663997	0.449859	0.106790	0.062031	0.056455
117	0.41167	0.284883	0.139969	0.139236	0.145185
118	0.406846	0.303178	0.164922	0.17014	0.181075
119	0.394953	0.255298	0.101668	0.083073	0.082264
120	0.394996	0.279248	0.110166	0.092379	0.092710
121	0.866261	0.795481	0.556344	0.375510	0.343068
122	0.868778	0.800439	0.562391	0.36799	0.335588
123	0.845111	0.728265	0.397709	0.231549	0.202688
124	0.843618	0.726500	0.40902	0.233521	0.203513
125	0.685194	0.577788	0.504258	0.492269	0.489637
126	0.686252	0.583940	0.535127	0.514183	0.508018
127	0.670852	0.529013	0.356504	0.304346	0.291129
128	0.665519	0.529789	0.370013	0.337368	0.323810
129	0.44275	0.248025	0.070769	0.05564	0.055493
130	0.680749	0.539471	0.279370	0.184412	0.171565
131	0.632960	0.476303	0.165255	0.093641	0.082498
132	0.636626	0.476006	0.156817	0.104165	0.098435
133	0.636279	0.470174	0.152994	0.099791	0.094176
134	0.636279	0.470174	0.152994	0.099791	0.094176

135	0.457446	0.251991	0.066413	0.052619	0.052399
136	0.726502	0.594827	0.28591	0.184034	0.169288
137	0.764484	0.581018	0.155861	0.08684	0.077923
138	0.522379	0.379146	0.158697	0.122266	0.120146
139	0.644664	0.491754	0.179699	0.12758	0.123393
140	0.627946	0.456605	0.140578	0.08305	0.075917
141	0.638949	0.467715	0.155798	0.100602	0.094658
142	0.632969	0.477116	0.159144	0.107436	0.102182
143	0.636279	0.470174	0.152994	0.099791	0.094176

Hypersonic Set

Run #	$x/L)_{0.1}$	$x/L)_{0.2}$	$x/L)_{0.6}$	$x/L)_{0.9}$	$x/L)_{1.0}$
1	0.313643	0.136974	0.060851	0.059727	0.060238
2	0.313227	0.157908	0.093960	0.081028	0.078852
3	0.308210	0.132925	0.045342	0.037314	0.035753
4	0.289383	0.141513	0.068218	0.049299	0.046142
5	0.209953	0.102286	0.050092	0.058655	0.062521
6	0.222237	0.101922	0.064806	0.068908	0.071347
7	0.204360	0.093955	0.036852	0.036384	0.037322
8	0.252756	0.113327	0.047668	0.045274	0.045868
9	0.772905	0.556603	0.162715	0.105546	0.099166
10	0.700253	0.466498	0.169273	0.159361	0.159113
11	0.756203	0.534226	0.134342	0.073701	0.065070
12	0.684307	0.440328	0.130104	0.102614	0.097842
13	0.528564	0.393636	0.167839	0.134172	0.132308
14	0.528644	0.396630	0.167902	0.150727	0.160392
15	0.515547	0.368703	0.133831	0.093952	0.088577
16	0.488258	0.342916	0.123507	0.090575	0.094255
17	0.313643	0.136974	0.060851	0.059727	0.060238
18	0.313227	0.157908	0.093960	0.081028	0.078852
19	0.289508	0.124713	0.044805	0.036833	0.035410
20	0.305960	0.148223	0.071187	0.051805	0.048338
21	0.210146	0.100665	0.049853	0.058267	0.062454
22	0.229851	0.107735	0.064900	0.070384	0.073163
23	0.240014	0.107333	0.037227	0.035522	0.036641
24	0.252756	0.113327	0.047668	0.045274	0.045868
25	0.772905	0.556603	0.162715	0.105546	0.099166
26	0.700253	0.466498	0.169273	0.159361	0.159113
27	0.756203	0.534226	0.134342	0.073701	0.065070
28	0.684307	0.440328	0.130104	0.102614	0.097842
29	0.528564	0.393636	0.167839	0.134172	0.132308
30	0.528644	0.396630	0.167902	0.150727	0.160392
31	0.474192	0.325569	0.118133	0.083525	0.078964
32	0.473182	0.327391	0.116202	0.093136	0.095531
33	0.284351	0.113576	0.043133	0.046254	0.047737
34	0.285912	0.120703	0.067961	0.062975	0.062689
35	0.276560	0.104658	0.027931	0.023541	0.022659
36	0.277982	0.110600	0.046128	0.034462	0.032149
37	0.182749	0.081555	0.035995	0.045862	0.051198

38	0.184664	0.081017	0.041912	0.051364	0.056099
39	0.177560	0.075009	0.024287	0.024408	0.025790
40	0.178935	0.074598	0.028382	0.028468	0.029481
41	0.672677	0.439238	0.119171	0.075567	0.070833
42	0.672696	0.439723	0.128918	0.118831	0.121831
43	0.654785	0.410471	0.091608	0.047584	0.040890
44	0.654797	0.410884	0.096382	0.066950	0.064593
45	0.431151	0.303374	0.127074	0.103420	0.102106
46	0.431199	0.303624	0.126942	0.113908	0.119734
47	0.419544	0.279761	0.096701	0.067377	0.063351
48	0.418387	0.280227	0.096324	0.070674	0.069336
49	0.284351	0.113576	0.043133	0.046254	0.047737
50	0.285912	0.120703	0.067961	0.062975	0.062689
51	0.276560	0.104658	0.027931	0.023541	0.022659
52	0.277982	0.110600	0.046128	0.034462	0.032149
53	0.182749	0.081555	0.035995	0.045862	0.051198
54	0.184664	0.081017	0.041912	0.051364	0.056099
55	0.177560	0.075009	0.024287	0.024408	0.025790
56	0.178935	0.074598	0.028382	0.028468	0.029481
57	0.672677	0.439238	0.119171	0.075567	0.070833
58	0.672696	0.439723	0.128918	0.118831	0.121831
59	0.653456	0.412121	0.094564	0.049328	0.042407
60	0.654797	0.410884	0.096382	0.066950	0.064593
61	0.431151	0.303374	0.127074	0.103420	0.102106
62	0.431199	0.303624	0.126942	0.113908	0.119734
63	0.421570	0.281725	0.099053	0.068859	0.064807
64	0.418387	0.280227	0.096324	0.070674	0.069336
65	0.705087	0.540612	0.182553	0.121720	0.113853
66	0.707550	0.561515	0.197522	0.144338	0.140376
67	0.683811	0.498315	0.141833	0.073325	0.062995
68	0.677821	0.498786	0.135708	0.075448	0.066171
69	0.459095	0.327990	0.216260	0.217506	0.224749
70	0.453357	0.332199	0.229236	0.233346	0.243989
71	0.443472	0.295223	0.153637	0.130603	0.128158
72	0.433173	0.293595	0.154909	0.132052	0.129760
73	0.893021	0.846696	0.749181	0.602693	0.552279
74	0.900869	0.857864	0.769677	0.618294	0.563026
75	0.864476	0.758427	0.497167	0.352359	0.311614
76	0.862658	0.756269	0.498472	0.358232	0.315713
77	0.737411	0.664164	0.670530	0.769408	0.790733
78	0.748452	0.681464	0.698561	0.817473	0.843236
79	0.713158	0.596240	0.454333	0.445954	0.447632
80	0.716181	0.602391	0.464310	0.459949	0.462939
81	0.705087	0.540612	0.182553	0.121720	0.113853
82	0.707550	0.561515	0.197522	0.144338	0.140376
83	0.683811	0.498315	0.141833	0.073325	0.062995
84	0.677821	0.498786	0.135708	0.075448	0.066171
85	0.459095	0.327990	0.216260	0.217506	0.224749
86	0.453357	0.332199	0.229236	0.233346	0.243989
87	0.443472	0.295223	0.153637	0.130603	0.128158
88	0.433173	0.293595	0.154909	0.132052	0.129760
89	0.893021	0.846696	0.749181	0.602693	0.552279
90	0.900869	0.857864	0.769677	0.618294	0.563026
91	0.863593	0.757330	0.498653	0.359515	0.318422
92	0.862658	0.756269	0.498472	0.358232	0.315713

93	0.742124	0.672772	0.684550	0.790113	0.811344
94	0.748452	0.681464	0.698561	0.817473	0.843236
95	0.713158	0.596240	0.454333	0.445954	0.447632
96	0.716181	0.602391	0.464310	0.459949	0.462939
97	0.670234	0.519312	0.177501	0.116538	0.109114
98	0.670236	0.519787	0.183220	0.130998	0.127960
99	0.637089	0.449529	0.113720	0.054872	0.045982
100	0.637090	0.449813	0.115928	0.057769	0.049171
101	0.404187	0.288072	0.226488	0.241930	0.254897
102	0.404187	0.288072	0.229999	0.254861	0.272740
103	0.382607	0.247573	0.139843	0.122896	0.121805
104	0.382607	0.247573	0.141272	0.126581	0.126507
105	0.885880	0.838162	0.751697	0.622687	0.570357
106	0.885880	0.838162	0.751927	0.624968	0.573119
107	0.843158	0.723857	0.446805	0.317996	0.281233
108	0.842008	0.722540	0.446063	0.317281	0.279372
109	0.709165	0.638181	0.681259	0.846460	0.899313
110	0.716296	0.648135	0.697410	0.871946	0.929625
111	0.677867	0.556325	0.424869	0.432433	0.442050
112	0.679939	0.559778	0.430396	0.440058	0.449968
113	0.670234	0.519312	0.177501	0.116538	0.109114
114	0.670236	0.519787	0.183220	0.130998	0.127960
115	0.637089	0.449529	0.113720	0.054872	0.045982
116	0.637090	0.449813	0.115928	0.057769	0.049171
117	0.404187	0.288072	0.226488	0.241930	0.254897
118	0.404187	0.288072	0.229999	0.254861	0.272740
119	0.382607	0.247573	0.139843	0.122896	0.121805
120	0.382607	0.247573	0.141272	0.126581	0.126507
121	0.885880	0.838162	0.751697	0.622687	0.570357
122	0.885880	0.838162	0.751927	0.624968	0.573119
123	0.844246	0.725213	0.446585	0.312664	0.275889
124	0.842008	0.722540	0.446063	0.317281	0.279372
125	0.703953	0.628357	0.665000	0.824245	0.877155
126	0.716296	0.648135	0.697410	0.871946	0.929625
127	0.676838	0.552957	0.419271	0.424998	0.434447
128	0.679939	0.559778	0.430396	0.440058	0.449968
129	0.444469	0.248002	0.075206	0.069598	0.070512
130	0.707919	0.582520	0.410085	0.331705	0.309653
131	0.686217	0.545469	0.235305	0.155987	0.145151
132	0.647380	0.498951	0.217713	0.142415	0.131584
133	0.666420	0.521507	0.225575	0.147896	0.136734
134	0.666420	0.521507	0.225575	0.147896	0.136734
135	0.488374	0.305799	0.084659	0.068856	0.068354
136	0.757422	0.637789	0.397064	0.267740	0.242829
137	0.787677	0.652821	0.207067	0.115969	0.102096
138	0.555118	0.417084	0.230736	0.180279	0.175306
139	0.678546	0.547955	0.260965	0.186511	0.177958
140	0.654289	0.495878	0.192040	0.114985	0.103003
141	0.667091	0.521264	0.228153	0.147857	0.136041
142	0.666420	0.521516	0.225156	0.148195	0.138466
143	0.666420	0.521507	0.225575	0.147896	0.136734

APPENDIX E

RESPONSE SURFACE EQUATION COEFFICIENTS

Supersonic RSE's

Parameter	$x/L)_{0.1}$	$x/L)_{0.2}$	$x/L)_{0.6}$	$x/L)_{0.9}$	$x/L)_{1.0}$
Intercept	-0.429426	-0.656713	-0.005021	0.201417	0.220654
M_e	0.592250	0.589568	-0.089006	-0.152321	-0.154993
ρ_∞/ρ_e	0.008140	0.000168	0.005799	0.008388	0.010131
Alt	-0.000086	-0.000211	0.001342	0.000437	0.000251
h/L	7.310527	6.880756	-1.623398	-2.424747	-2.387412
θ_1	-0.010464	-0.002752	0.003337	-0.006158	-0.007461
θ_2	-0.000122	0.000225	0.010773	0.010783	0.010851
M_∞	-0.000500	-0.010662	0.006657	-0.002868	-0.004272
M_e* M_e	-0.091036	-0.093000	0.019078	0.022221	0.022158
ρ_∞/ρ_e *M_e	-0.001395	-0.001046	-0.000570	-0.000361	-0.000459
ρ_∞/ρ_e *ρ_∞/ρ_e	-0.000116	0.001179	0.000237	-0.000521	-0.000852
*Alt**M_e	0.000004	0.000010	0.000014	0.000014	0.000019
*Alt**ρ_∞/ρ_e	0.000006	0.000007	0.000004	0.000000	-0.000001
*Alt*Alt*	0.000001	0.000002	-0.000011	-0.000004	-0.000002
*h/L**M_e	-0.340211	0.260603	1.476237	1.246411	1.165270
*h/L**ρ_∞/ρ_e	-0.026815	-0.021034	-0.032287	-0.020707	-0.018595
*h/L*Alt*	-0.000430	-0.000426	0.000090	0.000012	0.000045
*h/L*h/L*	-17.40584	-18.26763	6.618163	6.519827	6.105137
θ_1*M_e	-0.002142	-0.004041	-0.000418	0.002383	0.002788

$\theta_1 * \rho_\infty/\rho_e$	-0.000067	-0.000098	-0.000024	0.000077	0.000108
θ_1*Alt	-0.000002	-0.000002	-0.000002	0.000000	0.000001
θ_1*h/L	-0.018666	-0.043484	-0.012322	0.024990	0.029730
$\theta_1 * \theta_2$	0.000141	0.000196	-0.000042	0.000045	0.000061
θ_2*M_e	-0.000516	-0.001760	-0.004017	-0.004027	-0.004072
$\theta_2 * \rho_\infty/\rho_e$	-0.000003	-0.000030	-0.000150	-0.000263	-0.000308
$\theta_2 * Alt$	0.000000	0.000001	0.000000	-0.000002	-0.000002
$\theta_2 * h/L$	-0.006273	-0.023710	-0.066151	-0.059927	-0.058430
$\theta_2 * \theta_1$	0.000023	0.000062	-0.000029	-0.000125	-0.000154
$\theta_2 * \theta_2$	0.000033	0.000204	0.000021	0.000132	0.000163
$M_\infty * M_e$	-0.000271	0.000404	0.000289	-0.000489	-0.000724
$M_\infty * \rho_\infty/\rho_e$	0.000201	0.000535	0.000456	0.000461	0.000469
$M_\infty * Alt$	0.000002	0.000009	0.000008	0.000004	0.000005
$M_\infty * h/L$	0.014083	0.008278	-0.003444	-0.003690	-0.005067
$M_\infty * \theta_1$	-0.000114	-0.000020	0.000024	0.000072	0.000069
$M_\infty * \theta_2$	-0.000084	-0.000132	-0.000180	-0.000216	-0.000235
$M_\infty * M_\infty$	0.000154	0.001090	-0.000700	0.000650	0.000927

Hypersonic RSE's

Parameter	$x/L)_{0.1}$	$x/L)_{0.2}$	$x/L)_{0.6}$	$x/L)_{0.9}$	$x/L)_{1.0}$
Intercept	0.247430	0.645303	-0.412520	0.101824	0.440777
M_e	0.334700	0.384388	-0.051888	-0.233537	-0.264455
γ_e	-0.496079	-1.358614	0.508837	0.187371	-0.173485
Alt	-0.000195	-0.001189	0.001050	0.000990	0.000724
h/L	8.212618	8.390059	0.394171	-2.115018	-2.672394
θ_1	-0.004704	-0.010490	0.004326	-0.009398	-0.015173
θ_2	0.001718	0.004421	0.022732	0.035445	0.039071
M_∞	-0.013146	-0.016612	0.010827	0.013088	0.010243
$M_e * M_e$	-0.045696	-0.052351	0.007068	0.025632	0.026386
$\gamma_e * M_e$	0.033588	0.026973	0.019123	0.039880	0.050761

γ_e *γ_e	0.104034	0.434064	-0.228221	-0.121249	0.000108
Alt*M_e	0.000003	0.000008	0.000002	-0.000001	-0.000001
Alt*γ_e	0.000021	0.000084	-0.000037	-0.000169	-0.000169
Alt*Alt	0.000001	0.000006	-0.000005	-0.000004	-0.000003
h/L*M_e	-0.311327	0.075841	1.207769	1.304075	1.274717
h/L*γ_e	-0.407977	-0.885994	-0.767985	-0.251476	-0.056918
h/L*Alt	-0.000615	-0.000471	-0.000168	-0.000088	-0.000100
h/L*h/L	-17.144060	-18.430140	4.828037	7.153883	6.890013
θ_1*M_e	-0.001130	-0.002636	-0.000032	0.002848	0.003722
θ_1*γ_e	-0.006059	-0.001490	0.002894	0.004983	0.006337
θ_1*Alt	0.000000	-0.000002	-0.000001	-0.000001	-0.000001
θ_1*h/L	-0.015613	-0.018874	-0.021546	0.028574	0.047500
θ_1*θ_1	0.000100	0.000304	-0.000176	-0.000041	0.000006
θ_2*M_e	-0.000629	-0.001853	-0.005014	-0.006235	-0.006452
θ_2*γ_e	-0.000904	-0.001988	-0.005284	-0.009136	-0.010850
θ_2*Alt	-0.000002	-0.000003	-0.000001	-0.000001	-0.000001
θ_2*h/L	-0.014839	-0.034663	-0.106650	-0.132429	-0.134049
θ_2*θ_1	0.000044	0.000075	0.000032	-0.000247	-0.000345
θ_2*θ_2	0.000026	0.000162	-0.000092	0.000013	0.000085
M_∞*M_e	0.000439	0.000742	-0.000088	-0.000268	-0.000335
M_∞*γ_e	0.006798	0.006146	-0.002353	-0.003707	-0.003605
M_∞*Alt	0.000004	0.000004	0.000001	0.000002	0.000002
M_∞*h/L	-0.016970	-0.024617	-0.008372	0.013592	0.018469
M_∞*θ_1	0.000127	0.000105	-0.000030	-0.000052	-0.000031
M_∞*θ_2	-0.000040	-0.000078	-0.000138	-0.000215	-0.000247
M_∞*M_∞	0.000111	0.000391	-0.000237	-0.000265	-0.000124

APPENDIX F

ABLV-GT2 ENGINE DESIGN VARIABLES FOR SCCREAM

All dimensional quantities for reference length of 150 ft:

Vehicle Forebody/ 2-D External Compression System Design:

Forebody Width 30.5 ft
Cowl Height 1.9 ft

Ramp #	Length (ft)	Angle (deg)
#1	40.6	6.0
#2	15.4	9.0
#3	13.0	17.0

Engine Areas:

Station	Area(ft2)
1	58.0
2	51.1
3	58.0
4	82.3
e	123.2
e'	383.3

Engine Efficiency's:

Component	η (%)
Mixer	95.0
Combustor	95.0
Nozzle	98.0

Subsonic Combustion Fuel Injectors:

Initial Temperature	536.4 R
Injection Velocity	3,000 ft/s
Injection Angle	Parallel

Injector Location	20% of length station 3 to 4
Friction Coefficient	0.001

Supersonic Combustion Fuel Injectors:

Initial Temperature	536.4 R
Injection Velocity	4,000 ft/s
Injection Angle	Parallel
Injector Location	5% of length station 3 to 4
Friction Coefficient	0.001

Rocket ThrusterSpecifications:

Initial H_2 Temperature	536.4 R
Initial O_2 Temperature	536.4 R
Mixture Ratio	6.5
Chamber Pressure	2,500 psi
Actual Expansion Ratio	10.0
All-Rocket Mode Expansion Ratio	400.0

Aftbody Geometry:

Nozzle Length	37.1 ft
Initial Expansion Angle	20^o
Final Expansion Angle	5^o
Height-to-Length Ratio	0.109

Engine Thrust-to-Weight Ratio	30.0
Vehicle Takeoff Thrust-to-Weight Ratio	0.65
Approximate Engine Bypass Ratio	1.3

REFERENCES

1. Olds, J.R., *Multidisciplinary Design Techniques Applied To Conceptual Aerospace Vehicle Design*, Thesis Dissertation, North Carolina State University, Raleigh, NC., 1993.

2. Ruffin, S.M. and Spaid, F.W., "Hypersonic Single Expansion Ramp Nozzle Simulations.", Journal of Spacecraft and Rockets, Nov.-Dec. 1992.

3. Anonymous, NASA Computational Fluid Dynamics Conference, Vol. 2: Sessions VII-XII, Conference Publication 10038, NASA Ames Research Center, Moffett Field, CA, 1989.

4. Nasuit, F., and Onofri, M., "Analysis of In-Flight Behavior of Truncated Plug Nozzles.", presented at the 36th AIAA/ASME/SAE/ASEE Joint Propulsion Conference and Exhibit, AIAA 2000-3289, Huntsville, AL, July 2000.

5. Farrell, D.J. and Stemler, J.N., "ABLV Status Review - Slush Hydrogen Version of the ABLV-7C.", Boeing Phantom Works, April 2000.

6. Hunt, J.L., and Petley, D.H., "Airbreathing Launch Vehicle Study Status Overview.", NASA Langley Research Center, Oct. 1999.

7. Olds, J.R., and Bradford, J.E., "SCCREAM: A Conceptual Rocket-Based Combined-Cycle Engine Performance Analysis Tool.", AIAA Journal of Propulsion and Power, Vol. 17, No. 2, March-April 2001.

8. Mavris, D.N., and Bandte, O., "Economic Uncertainty Assessment Using A Combined Design of Experiments/Monte Carlo Simulation Approach with Application to an HSCT.", 17th Annual Conference of the International Society of Parametric Analysts, San Diego, CA., May 1995.

9. Heiser, W.H., and Pratt, D.T., *Hypersonic Airbreathing Propulsion*, American Institute of Aeronautics and Astronautics, Washington D.C., 1994.

10. Heppenheimer, T.A., *A Brief History of Flight*, John Wiley and Sons, New York, 2001.

11. Friedman, N., *U.S. Naval Weapons*, Naval Institute Press, Annapolis, MD., 1982.

12. Rich, B.R., and Janes, L., *Skunk Works*, Little, Brown, and Company, Boston, MA., 1994.

13. Roudakov, A.S., "Flight Testing of An Axisymetric Scramjet: Russian Recent Advances.", IAF Paper No. 93-S.4.485, 1993.

14. Curran, E.T., "Scramjet Engines: The First Forty Years," ISABE 97-7005, XIII International Symposium on Air-Breathing Engines, Chattanooga, TN., Sept. 1997.

15. Escher, W. J. D., and Flornes, B. J., "A Study of Composite Propulsion Systems For Advanced Launch Vehicle Applications.", Marquardt Corporation, Final Report for NASA Contract NAS7-377, Vols. 1-7, Van Nuys, CA, April 1967.

16. Foster, R. W., Escher, W., and Robinson J., "Air Augmented Rocket Propulsion Concepts.", Astronautics Corporation, Final Report for USAF Contract USAF AFAL-TR-88-004, Madison, WI, April 1988.

17. Escher, W.J.D., "A U.S. History of Airbreathing/Rocket Combined-Cycle (RBCC) Propulsion for Powering Future Aerospace Transports With A Look Ahead To The Year 2020.", SAIC, Hunstville, AL, Dec. 1999.

18. Escher, W. J. D., ed., *The Synerjet Engine: Airbreathing/Rocket Combined-Cycle Propulsion for Tomorrow's Space Transports*, SAE PT-54, Society of Automotive Engineers, Warrendale, PA, 1997.

19. Olds, J.R., Bradford, J.E., et al. "Hyperion: An SSTO Vision Vehicle Concept Utilizing Rocket Based Combined Cycle Propulsion.", AIAA 99-4944, 9th International Space Planes and Hypersonic Systems and Technologies Conference, Norfolk, VA., Nov. 1999.

20. Olds, J. R. and Bellini, P. X., "Argus, a Highly Reusable SSTO Rocket-Based Combined Cycle Launch Vehicle with Maglifter Launch Assist.", AIAA 98-1557, AIAA 8th International Space Planes and Hypersonic Systems and Technologies Conference, Norfolk, VA, April 1998.

21. Olds, J.R., Ledsinger, L., Bradford, J., Charania, A., McCormick, D., "Stargazer: A TSTO Bantam-X Vehicle Concept Utilizing Rocket-Based Combined-Cycle Propulsion.", AIAA 99-4888, 9th International Space Planes and Hypersonic Systems and Technologies Conference, Norfolk, VA, Nov. 1999.

22. Lockwood, M.K., and Hunt, J.L., "Design and Analysis of a Two-Stage-to-Orbit Airbreathing Hypersonic Vehicle Concept.", AIAA 96-2890, 32nd AIAA/ASME/SAE /ASEE Joint Propulsion Conference, Lake Buena Vista, FL, July 1996.

23. Nasuti, F. and Onofri, M., "NASA's Hyper-X Program." IAF-00-V.4.01, 51st International Astronautical Congress, Rio de Janeiro, Brazil, October 2000.

24. Reubush, D., "Hyper-X Stage Separation – Background and Status.", AIAA 99-4818, 9th International Space Planes and Hypersonic Systems and Technologies Conference, Norfolk, VA., Nov. 1999.

25. Hueter, U., and Turner, J., "Rocket-Based Combined Cycle Activities in the Advanced Space Transportation Program Office.", AIAA 99-2352, 35th AIAA/ASME/SAE/ASEE Joint Propulsion Conference and Exhibit, Los Angeles, CA, June 1999.

26. Heuter, U., "Rocket-Based Combined-Cycle Propulsion Technology for Access-to-Space Applications.", AIAA 99-4925, 9th International Space Planes and Hypersonic Systems and Technologies Conference, Norfolk, VA, Nov. 1999.

27. Anonymous, "Introduction to NASA's Integrated Space Transportation Plan and Space Launch Initiative.", National Aeronautics and Space Administration, May 2001.

28. Bulman, M. and Siebenhaar, A., "The Strutjet Engine: Exploding the Myths Surrounding High Speed Airbreathing Propulsion.", AIAA 95-2475, 31st AIAA/ASME/SAE/ASEE Joint Propulsion Conference and Exhibit, San Diego, CA., July, 1995.

29. Pandolfini, P., "Instructions for Using Ramjet Performance Analysis (RJPA) IBM-PC Version 1.24.", JHU/APL AL-92-P175, June 1992.

30. Cruise, D.R., "Notes on the Rapid Computation of Chemical Equilibria.", Journal of Physical Chemistry, 1964.

31. Burkardt, L. A., and Franciscus, L. C., "RAMSCRAM - A Flexible Ramjet/Scramjet Engine Simulation Program." NASA TM-102451, June 1990.

32. Pinckney, S.Z. and Walton, J.T., "Program SRGULL: An Advanced Engineering Model for the Prediction of Airframe-Integrated Subsonic/Supersonic Hydrogen Combustion Ramjet Cycle Performance.", NASA Langley Research Center, Hampton VA, NASP TM-1120, 1991.

33. Pinckney, S.Z., Ferlemann, S.M., "Program Manual for SRGULL, Version 1.0.", NASA Langley Research Center, Hampton, VA, July 2000.

34. Salas, M., "Shock Fitting Method for Complicated Two-Dimensional Supersonic Flows.", AIAA Journal, Vol. 14, No.5, May 1976.

35. Hill, P., and Peterson, C., *Mechanics and Thermodynamics of Propulsion, 2nd Edition*, Addison-Wesley Publishing Company, Inc., Reading, MA., June 1992.

36. Dobrowolski, A., "Analysis of Nonconstant Area Combustion and Mixing in Ramjet and Rocket-Ramjet Hybrid Engines.", National Aeronautics and Space Administration, NASA TN D-3626, Washington D.C., Oct. 1966.

37. Barnhart, P.J., "IPAC – Inlet Performance Analysis Code.", NASA-CR-204130, July 1997.

38. Zucrow, M.J., Hoffman, J.D., *Gas Dynamics Volume 1*, John Wiley and Sons Publishing, New York, 1976.

39. Anderson, J.D., *Modern Compressible Flow*, McGraw-Hill Publishing Co., Inc., New York, 1990.

40. Faires, J.D., and Faires, B.T., *Calculus 2nd Edition*, Random House Mathematics Series, 1986.

41. Zucrow, M.J., Hoffman, J.D., *Gas Dynamics Volume 2*, John Wiley and Sons, Inc., New York, 1976.

42. Seddon, J., Goldsmith, E.L., *Intake Aerodynamics, Second Edition*, American Institute of Aeronautics and Astronautics, Washington D.C., 1999.

43. Cengel, Y.A., and Boles, M.A., *Thermodynamics, An Engineering Approach, 2nd Edition*, McGraw-Hill Inc., New York, 1994.

44. Gordon, S. and McBride, B.J., "Computer Program for Calculation of Complex Chemical Equilibrium Compositions and Applications.", NASA Reference Publication 1311, Oct. 1994.

45. Denbigh, K., *The Principles of Chemical Equilibrium*, 4th Edition, Cambridge University Press, New York, 1981.

46. Vincenti, W.G., and Kruger, C.H., *Introduction to Physical Gas Dynamics*, Krieger Publishing Company, Malabar, Fl., 1986.

47. Golub, G.H, and Van Loan, C.F., *Matrix Computations 3rd Edition*, Johns Hopkins University Press, Baltimore, MD., 1983.

48. Humble, R.W., Henry, G.N., and Larson, W.J., *Space Propulsion Analysis and Design*, McGraw-Hill Inc., New York, 1995.

49. Tannehill, J.C., Anderson, D.A., Pletcher, R.H., *Computational Fluid Mechanics and Heat Transfer*, Hemisphere Publishing Co., 1997.

50. Ruffin, S.M., Venkatapathy, E., Spaid, F.W., et al., "Single Expansion Ramp Nozzle Simulations.", American Institute of Aeronautics and Astronautics, 1992.

51. Press, W.H., Teukolsky, S.A, Vetterling, W.T., and Flannery, B.P., *Numercial Recipes in C, The Art of Scientific Computing, Second Edition*, Cambridge University Press, New York, 1995.

52. Tai, J.C., Mavris, D.N., and Schrage, D.P., "Application of a Response Surface Method to the Design of Tipjet Driven Stopped Rotor/Wing Concepts.", American Institute of Aeronautics and Astronautics, 1995.

53. Mason, R., Gunst, R., and Hess, J., *Statistical Design and Analysis of Experiments*, John Wiley & Sons, NY, 1989.

54. Anonymous, *JMP Users Guide, Version 3.1*, SAS Institute, Inc., Cary, NC., 1995.

55. Knill, D.L., Giunta, A.A, Baker, C.A., "Response Surface Methods Combining Linear and Euler Aerodynamics for Supersonic Transport Design.", Journal of Aircraft, Vol. 36, No. 1, Jan.-Feb.1999.

56. Bradford, J. E., Olds, J. R., "*SCCREAM* v.5: A Web-Based Airbreathing Propulsion Analysis Tool.", AIAA 99-2104, Conference Proceeding of the 35th AIAA/ASME/SAE/ASEE Joint Propulsion Conference, Los Angeles, CA., June 1999.

57. Bradford, J. E. and Olds, J.R., "Improvements and Enhancements to SCCEAM, A Conceptual RBCC Engine Analysis Tool.", AIAA 98-3775, Conference Proceeding of the *34th AIAA/ASME/SAE/ASEE Joint Propulsion Conference,* Cleveland, OH., July 1998.

58. Olds, J.R., Bradford, J.E., "SCCREAM (Simulated Combined-Cycle Rocket Engine Analysis Module): A Conceptual RBCC Engine Design Tool.", AIAA 97-2760, 33rd AIAA/ASME/SAE/ASEE Joint Propulsion Conference and Exhibit, Seattle, WA., July 1997.

59. Flamig, B., *Practical Data Structures in C++,* John Wiley and Sons, Inc., New York, 1993.

60. Chase, M.W., Davies, C.A., Downey, J.R., and Frurip, D.J., *JANAF Thermochemical Tables, 3rd Edition*, National Bureau of Standards, American Institute of Physics, Inc., New York, 1986.

61. Anonymous, *1962 U.S. Standard Atmosphere*, U.S. Government Printing Office, Washington D.C., Dec. 1962.

62. Wall, L., Christiansen, T., and Schwart, R., *Programming Perl*, O'Reilly & Associates, Inc., CA., 1996.

63. Negrino, T., *JavaScript For the World Wide Web*, Peachpit Press, CA., 1998.

64. Castro, E., *HTML 4 For the World Wide Web*, Peachpit Press, CA., 1998.

65. Kelley, C., and Williams, T., *GNUPLOT Unix Version 3.5*, Dartmouth College, Hanover, NH., 1993.

66. Anonymous, *Aladdin Ghostscript 5.03*, Aladdin Enterprises, Menlo Park, CA., 1997.

67. Brauer, G. L., et al., "Program to Optimize Simulated Trajectories (POST).", Martin-Marietta Corp., Final Report for NASA Contract NAS1-18147, Denver, CO., Sept. 1989.

68. Olds, J. R., and McCormick, D. J., "Component-Level Weight Analysis for RBCC Engines.", AIAA 97-3953, 1997 Defense and Space Programs Conference and Exhibit, Huntsville, AL., Sept. 1997.

69. Moses, P.L. and Ferlemann, S.M. et al. "An Airbreathing Launch Vehicle Design with Turbine-Based Low-Speed Propulsion and Dual Mode Scramjet High-Speed Propulsion.", AIAA 99-4948, 9th International Space Planes and Hypersonic Systems and Technologies Conference, Norfolk, VA., Nov. 1999.

70. Lawry, M.H., IDEAS Master Series, Student Guide, Structural Dynamics Research Corporation, Milford, OH. 1994.

71. Bradford, J.E., and Olds, J.R., et al. "Exploration of the Design Space for the ABLV-GT SSTO Reusable Launch Vehicle.", AIAA 2000-5136, Space 2000 Conference and Exposition, Long Beach, CA., Sept. 2000.

72. Sova, G., and Divan, P., "Aerodynamic Preliminary Analysis System II, Part II – User's Manual.", NASA CR 182077, April 1991.

73. NASA Ames Thermal Protection Materials and Systems Branch, TPS-X Database Internet Site, http://asm.arc.nasa.gov.

74. Olds, J.R., and Budianto, I.A., "Constant Dynamic Pressure Trajectory Simulation in POST.", AIAA 98-0302, 36th Aerospace Sciences Meeting and Exhibit, Reno, NV., Jan. 1998.

VITA

John Edward Bradford was born on May 9, 1973 in Pensacola, Florida. He attended grade school in Placentia, California at Van Buren Elementary and Kraemer Junior High. Upon moving to Matthews, North Carolina in 1986, he attended and graduated from Sun Valley High School. In the Fall of 1991, John was accepted to North Carolina State University in Raleigh. While there, he was a brother of Phi Sigma Pi National Honor Fraternity and an active member and officer in the student AIAA branch. In May of 1996, he graduated with honors and received his Bachelor of Science degree in Aerospace Engineering. John was also awarded a minor in Computer Programming.

In October of 1996, John began work on his Masters degree in Aerospace Engineering at the Georgia Institute of Technology in Atlanta. During the course of his academic studies, John served as the team lead on numerous vehicle design projects in association with the Space Systems Design Lab (SSDL), under the direction of Dr. John Olds. In the Fall of 1997, John obtained his Master of Science degree and continued on with his academic studies to obtain his Doctoral degree. While at Georgia Tech, John participated in the NASA Academy program and spent the summer of 1997 at the Marshall Space Flight Center in Huntsville, AL working in the Preliminary Design (PD) division. For the summer of 1998, John spent ten weeks at GenCorp Aerojet in Sacramento, CA as an engineering support student. In 1999, he was the recipient of a NASA Graduate Student Researcher fellowship to fund his doctoral research and studies. In accordance with this fellowship, he spent the following three summers at MSFC working advanced RLV concepts under the direction of Mr. David R. Komar.